

UNCLASSIFIED

NAVAL AIR WARFARE CENTER AIRCRAFT DIVISION
PATUXENT RIVER, MARYLAND



TECHNICAL REPORT

REPORT NO: NAWCADPAX/TR-2008/60

MODELING AND PREDICTION OF CORROSION-FATIGUE FAILURES IN AF1410 STEEL TEST SPECIMENS

by

**Mr. David T. Rusk, P.E.
Mr. Wally Hoppe, UDRI
Dr. William Braisted, UDRI
Mr. Nilesh Powar, UDRI**

12 January 2009

Approved for public release; distribution is unlimited.

UNCLASSIFIED

DEPARTMENT OF THE NAVY
NAVAL AIR WARFARE CENTER AIRCRAFT DIVISION
PATUXENT RIVER, MARYLAND


NAWCADPAX/TR-2008/60
12 January 2009

MODELING AND PREDICTION OF CORROSION-FATIGUE FAILURES IN AF1410
STEEL TEST SPECIMENS

by

Mr. David T. Rusk, P.E.
Mr. Wally Hoppe, UDRI
Dr. William Braisted, UDRI
Mr. Nilesh Powar, UDRI

RELEASED BY:

 1/12/09

BARRY STURGIS / AIR-4.3.3 / DATE
Head, Structures Division
Naval Air Warfare Center Aircraft Division

| REPORT DOCUMENTATION PAGE | | | Form Approved OMB No. 0704-0188 | | |
|--|--------------|------------------------------------|--|--|---|
| Public reporting burden for this collection of information is estimated to average 1 hour per response, including the time for reviewing instructions, searching existing data sources, gathering and maintaining the data needed, and completing and reviewing this collection of information. Send comments regarding this burden estimate or any other aspect of this collection of information, including suggestions for reducing this burden, to Department of Defense, Washington Headquarters Services, Directorate for Information Operations and Reports (0704-0188), 1215 Jefferson Davis Highway, Suite 1204, Arlington, VA 22202-4302. Respondents should be aware that notwithstanding any other provision of law, no person shall be subject to any penalty for failing to comply with a collection of information if it does not display a currently valid OMB control number. PLEASE DO NOT RETURN YOUR FORM TO THE ABOVE ADDRESS. | | | | | |
| 1. REPORT DATE 12 January 2009 | | 2. REPORT TYPE Technical Report | | 3. DATES COVERED 1 October 2003 – 31 March 2008 | |
| 4. TITLE AND SUBTITLE Modeling and Prediction of Corrosion-Fatigue Failures in AF1410 Steel Test Specimens | | | 5a. CONTRACT NUMBER F42600-00-D-0039, 0011 | | |
| | | | 5b. GRANT NUMBER | | |
| | | | 5c. PROGRAM ELEMENT NUMBER | | |
| 6. AUTHOR(S) Mr. David T. Rusk, P.E. Dr. William Braisted, UDRI | | | 5d. PROJECT NUMBER | | |
| | | | 5e. TASK NUMBER | | |
| | | | 5f. WORK UNIT NUMBER | | |
| 7. PERFORMING ORGANIZATION NAME(S) AND ADDRESS(ES) Structures Division, Code 4.3.3 Bldg. 2187 Room 2340A Naval Air Systems Command 48110 Shaw Road, Unit #5 Patuxent River, MD 20670-1906 | | | 8. PERFORMING ORGANIZATION REPORT NUMBER NAWCADPAX/TR-2008/60 | | |
| 9. SPONSORING/MONITORING AGENCY NAME(S) AND ADDRESS(ES) Office of Naval Research One Liberty Center 875 North Randolph St., Suite 1425 Arlington, VA 22203-1995 | | | 10. SPONSOR/MONITOR'S ACRONYM(S) ONR 3.5.1 | | |
| | | | 11. SPONSOR/MONITOR'S REPORT NUMBER(S) | | |
| 12. DISTRIBUTION/AVAILABILITY STATEMENT Approved for public release; distribution is unlimited. | | | | | |
| 13. SUPPLEMENTARY NOTES | | | | | |
| 14. ABSTRACT The global maritime operating environment of U.S. Naval Aviation assets necessitates their prolonged exposure to severe corrosive environments. The resulting corrosion damage on flight critical structural components has a significant adverse impact on fleet readiness and total ownership costs. To address these issues, NAVAIR has initiated a multiyear research program to investigate and quantify the fatigue life reduction due to corrosion on high-strength steels, and to develop models and metrics to implement actionable maintenance criteria for corrosion damage. An Equivalent Stress Riser (ESR) model has been proposed for AF1410 steel that extends traditional notched fatigue analysis methods to applications with multiple corrosion notches present. An approximate elasticity solution featuring a Fast Fourier Transform of the corroded surface data was developed, and is used to identify local stress concentration areas that may initiate fatigue cracks under loading. Groups of image pixels with stress concentration values above a certain threshold are treated as idealized semi-elliptical notches, with corrosion-fatigue (C-F) notch factor values assigned based on notch geometry and a calibration to an experimental database of failures on bare, unnotched AF1410 C-F test plates. Median life prediction results for abrasive blasted and polished sets of test specimens show a level of conservatism between 1.0 and 3.0 for most predictions, with more severe levels of corrosion on the polished set having a higher level of conservatism. Validation tests were performed using cadmium plated C-F test plates, with the ESR life predictions showing a level of conservatism similar to the predictions on the bare, abrasive blasted C-F test plates. The ESR model was adapted to account for stress gradient effects, and demonstrated by performing a life prediction on a partial WLI scan of the corroded surface of an F/A-18C/D arresting shank. The prediction was consistent with the fatigue test results for the shank, and showed a substantial amount of fatigue life remaining for the corrosion-damaged area. A second, grid-based surface roughness metric life prediction capability was developed for use with low-resolution, ultrasonic time-of-flight surface topology measurements. Life predictions using this model were more conservative than the corresponding ESR predictions, but further investigation of the behavior of the model for coated materials is necessary. | | | | | |
| 15. SUBJECT TERMS Corrosion Fatigue AF1410 Steel Crack Initiation Surface Roughness Stress Concentration Notches Probabilistic Analysis | | | | | |
| 16. SECURITY CLASSIFICATION OF: | | | 17. LIMITATION OF ABSTRACT | 18. NUMBER OF PAGES | 19a. NAME OF RESPONSIBLE PERSON |
| a. REPORT | b. ABSTRACT | c. THIS PAGE | | | David T. Rusk |
| Unclassified | Unclassified | Unclassified | SAR | 108 | 19b. TELEPHONE NUMBER (include area code) (301) 342-9428 |

SUMMARY

The global maritime operating environment of U.S. Naval Aviation platforms necessitates their prolonged exposure to severe corrosive environments. The resulting corrosion damage on flight critical structural components has a significant adverse impact on fleet readiness and total ownership costs. Much of the costs and inconvenience of corrosion damage repair can be traced to uncertainty over the severity of corrosion necessary to cause a significant reduction in the fatigue life of a damaged component. Of particular concern to naval aviation is corrosion damage on high-strength steel airframe components, such as landing gear and arresting shanks. To address these issues, NAVAIRSYSCOM, in conjunction with the University of Dayton Research Institute (UDRI), Engineering Software Research and Development, Inc., and the Boeing Company, initiated a research program to investigate and quantify the fatigue life reduction due to corrosion on high-strength steels, and to develop models that can be used to implement actionable maintenance criteria for corrosion damage.

Newer-built Navy tactical aircraft such as F/A-18 have utilized high-strength, high alloy steels such as AF1410 and Aermet 100 which do not pit in corrosive environments as conventional low-alloy steels do. A number of corrosion exposure experiments conducted by UDRI on bare AF1410 steel plate have shown that the material exhibits general oxidation and material loss in large patches, with local areas of microscopic, shallow notch-like dimples. The dimples are not considered to be pits in that the depth dimension is less than the surface diameter. Fatigue tests on corroded AF1410 steel unnotched flat plates were conducted as part of this research program to provide a robust set of test results for corrosion-fatigue (C-F) model development. Two sets of test specimens were fabricated, and are referred to as "Batch A" and "Batch B." The Batch A test specimens were grit-blasted after heat treatment, but prior to corroding. Batch B specimens were hand polished prior to corrosion, and were not grit-blasted. High-resolution 3D topographic maps of the corrosion on the fatigue test plate specimens were made after they were corroded and cleaned, but prior to fatigue testing using a WYKO NT-8000 white light interferometer, with a lateral resolution of 7.66 μm per pixel and a vertical resolution that tended toward 0.1 μm .

An Equivalent Stress Riser (ESR) model has been proposed that extends traditional notched fatigue analysis methods to applications of multiple corrosion notches in high-strength steels. Critical corrosion notches for Batch A and Batch B C-F tests were characterized dimensionally using optical microscopic measurements, and were the basis of a Peterson notch sensitivity equation fit for the two test specimen batches. A difficult task in C-F modeling is distinguishing which corrosion notch or collection of notches will cause a critical crack on a component that has not yet failed. Initial attempts were made at performing conventional finite element analysis on the corroded surfaces of the C-F plates; however, the complex and chaotic corroded surface topology required geometric modeling simplifications that introduced significant error in the stress concentration predictions. An alternative approach was to develop an approximate elasticity solution using a Fast Fourier Transform (FFT) of the corroded surface data to represent the actual surface profile as a linear combination of sinusoidal components in the frequency domain. From the frequency information, the stress variation over the surface of each frequency component could be estimated with an approximate elasticity solution. The stress values

corresponding to each frequency component were then recombined, via an inverse FFT, to provide a stress concentration map of the corroded surface. The elasticity solution is used to identify local stress concentration areas that may initiate fatigue cracks under loading. An automated method was defined to enable the extraction of notch critical dimensions (width, height, and depth) from the geometric features that cause the local stress concentrations, on corroded surfaces with hundreds or thousands of notches present. Standard and custom software plug-ins for ImageJ were used to develop a filtering algorithm that sorts through a K_t map looking for groups of pixels with high K_t values above a certain threshold. These pixel groups are referred to as Regions of Interest (ROI), and are treated as idealized semi-elliptical notches for the purposes of fatigue modeling. C-F notch factor (K_{fc}) values are calculated for each ROI using the Peterson notch sensitivity equation and the notch K_t value estimated from the notch dimensions. K_{fc} values for the corroded surface are grouped into histograms and used to calculate a CDF of crack initiation probability for the component, assuming a series system failure analogy for corrosion notch fatigue cracks. Median life prediction results for the Batch A and Batch B C-F plates show a level of conservatism between 1.0 and 3.0 for most predictions, except for some of the 6-hr corrosion exposed Batch B specimens, which show a level of conservatism much higher. This effect was traced to the low K_t threshold value used to extract the ROIs from the K_t map for the Batch B specimens. A preliminary uncertainty analysis was performed to assess the influence of ESR model input uncertainty on the variability of the predicted fatigue life. The results showed that the model has a high degree of correlation between the individual ROI measurement errors, but the errors are not fully correlated. Using a fully correlated solution, 95% confidence bounds were generated for the median life prediction on a single test specimen.

As part of the C-F program investigations, AF1410 flat steel plates with discrete micromachined notch features were created to study the ability of traditional notched fatigue analysis approaches to predict fatigue life reduction due to known geometric shapes. Life predictions for the test plates were made using a Peterson notch sensitivity factor equation calibrated from geometrically-notched fatigue test data of various high-strength steels, taken from the Aerospace Structural Metals Handbook. Three different variations of the Peterson model were used to predict the mean and variance of the plate test fatigue lives. Two of the models had conservative mean life predictions, and the third had a nonconservative mean life prediction. Two of the models had good accuracy in predicting the test life variance, while the third gave a conservative prediction. None of the models were able to correctly predict that the conic frustum feature would crack first, because this feature did not conform to the idealized semi-elliptical shape that the notch metric equation was derived for. However, the results demonstrated that traditional notched fatigue analysis techniques, implemented in a probabilistic framework, can adequately capture the variance in fatigue test lives for shallow surface notches in uniform stress fields.

As a validation test, cadmium plated C-F test specimens were fabricated with the same geometry as the Batch B specimens, but a 1 in. diameter spot of plating was sanded away and the specimens corroded in an SO₂ salt fog chamber. The cad-plated corrosion has an overall topology that is different from the unplated specimens used to calibrate the ESR model, and more closely resembles the service-induced corrosion on the F/A-18 arresting shanks. The ESR life predictions show a level of conservatism similar to the predictions on the Batch A and Batch B plates, and demonstrate that the model is not dependent on how the corrosion damage was incurred on the surface. The ESR model was adapted to account for stress gradient effects by defining an equivalent gradient stress concentration factor ($K_{g-equiv}$) that describes the difference in crack initiation life between a notch at a local point in a gradient stress field and the same notch at a reference location. An effective C-F notch factor (K_{fc-eff}) is defined for the reference location that is the product of the local $K_{g-equiv}$ and K_{fc} values, and that when applied to the reference location stress history, will give the median life value of the local notch for its actual K_{fc} value. The K_{fc-eff} values for the corroded surface are grouped into histograms and used to calculate a CDF of crack initiation probability for the component, in the same way that life is predicted for uniform stress fields. This adaptation was demonstrated by performing an ESR life prediction on a partial WLI scan of the corroded surface of an F/A-18C/D arresting shank. The prediction, while conservative, was consistent with the fatigue test results for the shank, and showed a substantial amount of fatigue life remaining for the corrosion-damaged area.

The ESR approach relies on high-resolution 3D surface topography information to capture the corrosion notch features that cause fatigue cracking. However, currently deployed fleet nondestructive inspection techniques such as ultrasonic and eddy-current do not have the spatial and depth resolution necessary to capture the surface detail required for use of the ESR modeling approach. To accommodate this limitation, a grid-based surface roughness metric prediction capability was developed that is similar to the ESR method. Average and root-mean-square surface roughness values are calculated for each square of a 1 mm grid overlaid on a corroded surface. The roughness values are calculated from ultrasonic (UT) time-of-flight measurements of a corroded component. A regression curve converts the UT derived grid roughness values to equivalent WLI roughness values, and a second regression curve converts the WLI roughness values to equivalent K_{fc} values. The resulting K_{fc} values for the grid set are grouped into a histogram and used to calculate a CDF of crack initiation probability for the component, in the same way that life is predicted in the ESR method. Life predictions on three Batch B specimens with different levels of corrosion exposure show the method to be more conservative than the corresponding ESR predictions. However, fleet corroded components with protective coatings may not accumulate the type of large-scale corrosion damage necessary to trigger a UT-derived roughness metric fatigue life reduction, even though a significant amount of small-scale corrosion damage is present. For this reason, the behavior of roughness metric life prediction methods on coated materials should be ascertained before using the method to make disposition decisions on fleet corroded components.

A robust verification and validation (V&V) process was defined for this program, but budget and schedule constraints limited the amount of V&V work that could be completed. Still, the work that was completed indicates that the ESR model can meet the preliminary engineering validation criteria of a factor of 1 to 4 conservatism in model median life prediction error at the 95% confidence level, for light-to-moderate levels of surface corrosion damage. Whether the specified validation criteria represent acceptable limits for applying the method to fleet corroded components remains to be seen. Demonstration of the ESR method on several cases of fleet corroded components will likely be necessary to determine if the life predictions provide sufficient fatigue margin for the method to be useful.

Contents

| | <u>Page No.</u> |
|--|-----------------|
| Introduction..... | 1 |
| Methods | 2 |
| Corrosion-Fatigue Test Data..... | 2 |
| Corrosion Surface Imaging..... | 2 |
| Corrosion Notch Based Modeling | 3 |
| Corrosion-Fatigue Notch Sensitivity Model Calibration..... | 5 |
| Fast Fourier Transform Approach for Stress Concentration Mapping..... | 9 |
| Region of Interest Analysis..... | 14 |
| Uncorroded Corrosion-Fatigue Plate Probabilistic Life Prediction..... | 16 |
| Life Prediction Using the Equivalent Stress Riser Model | 16 |
| Life Prediction Uncertainty from the Equivalent Stress Riser Model | 17 |
| Equivalent Stress Riser Model Calibration Using Extreme Value Statistics | 20 |
| Micromachined Specimen Life Prediction | 23 |
| Cadmium-Plated Corrosion-Fatigue Specimen Life Prediction | 31 |
| Equivalent Stress Riser Modeling of Stress Gradient Effects | 31 |
| Corrosion Surface-Roughness Based Modeling | 33 |
| Verification and Validation of Corrosion-Fatigue Models..... | 51 |
| Results..... | 55 |
| Region of Interest K_{fc} Prediction Correlation..... | 55 |
| Uncorroded Corrosion-Fatigue Plate Probabilistic Life Prediction..... | 60 |
| Equivalent Stress Riser Corrosion-Fatigue Life Predictions | 61 |
| Life Prediction Uncertainty from the Equivalent Stress Riser Model | 64 |
| Equivalent Stress Riser Model Prediction Using Extreme Values Statistics | 65 |
| Micromachined Specimen Life Prediction | 68 |
| Equivalent Stress Riser Life Prediction on Cadmium-Plated Corrosion-Fatigue..... | 73 |
| Specimens | |
| Equivalent Stress Riser Life Prediction on an F/A-18C/D Arresting Shank Section..... | 73 |
| Corrosion Surface-Roughness Based Modeling | 78 |
| Verification and Validation Results from Corrosion-Fatigue Models..... | 79 |
| Discussion..... | 81 |
| Equivalent Stress Riser Model Application..... | 81 |
| Life Prediction Uncertainty from the Equivalent Stress Riser Model | 81 |
| Equivalent Stress Riser Model Calibration using Extreme Value Statistics | 81 |
| Equivalent Stress Riser Life Prediction on Micromachined Specimens | 81 |

| | <u>Page No.</u> |
|--|-----------------|
| Equivalent Stress Riser Life Prediction on Cadmium-Plated Corrosion-Fatigue..... | 83 |
| Specimens | |
| Equivalent Stress Riser Life Prediction on an F/A-18C/D Arresting Shank Section..... | 83 |
| Corrosion Surface-Roughness Based Modeling | 84 |
| Verification and Validation for Corrosion-Fatigue Models | 84 |
| Conclusions..... | 85 |
| References..... | 87 |
| Appendix A -Verification and Validation Framework Flowcharts | 91 |
| Distribution | 97 |

ACKNOWLEDGEMENTS

This research program was defined and initiated by Dr. Paul Hoffman of the Structures Division, Naval Air Systems Command. The authors wish to thank Paul for his guidance and inputs over the long course of this effort. The authors also wish to thank Mr. Eric Burke, formerly of the University of Dayton Research Institute, for his efforts in developing the surface feature identification approaches described in this report.

INTRODUCTION

The global maritime operating environment of U.S. Naval Aviation platforms necessitates their prolonged exposure to severe corrosive environments. The resulting corrosion damage on flight critical structural components has a significant adverse impact on fleet readiness and total ownership costs. Much of the costs and inconvenience of corrosion damage repair can be traced to uncertainty over the severity of corrosion necessary to cause a significant reduction in the fatigue life of a damaged component. This uncertainty has resulted in qualitative maintenance criteria for corrosion damage repair that are difficult to implement in practice, and do not provide objective measures of the reliability and risk associated with continued flight operation. Of particular concern to naval aviation is corrosion damage on high-strength steel airframe components, such as landing gear and arresting shanks. These components are generally highly stressed, have critical crack sizes below reliable nondestructive inspection (NDI) detection thresholds and possess very little damage tolerance capability. To address these issues, NAVAIRSYSCOM, in conjunction with the University of Dayton Research Institute (UDRI), Engineering Software Research and Development, Inc. (ESRD), and the Boeing Company, initiated a research program to investigate and quantify the fatigue life reduction due to corrosion on high-strength steels, and to develop models that can be used to implement actionable maintenance criteria for corrosion damage.

Newer-built Navy tactical aircraft such as F/A-18 have utilized high-strength, high alloy steels such as AF1410 and Aermet 100 in place of traditional high-strength, low alloy steels such as 4340, D6AC, and 300M for highly stressed components. The high alloy and low impurity content of AF1410 and Aermet 100 yield substantial improvements in corrosion resistance, stress corrosion cracking resistance and fracture toughness over comparable high-strength, low alloy steels. An additional benefit of this metallurgy is that these materials do not pit in corrosive environments as conventional low-alloy steels do. A number of corrosion exposure experiments conducted by UDRI on bare AF1410 steel plate have shown that the material exhibits general oxidation and material loss in large patches, with local areas of microscopic, shallow notch-like dimples. The dimples are not considered to be pits in that the depth dimension is less than the surface diameter. The conventional definition of pitting, as defined by Fontana [1], is that the depth dimension is the same as or greater than the surface diameter.

Traditional engineering approaches to predicting the fatigue life of pitted components, such as those of Mills, et al, [2] or Komai [3], often treat the corrosion pit as a semi-circular or tunneling crack, and use linear-elastic fracture mechanics or experimental crack growth rates to predict life. Empirical or statistical equivalent crack size or pit growth rate distributions are used to estimate the variability in pit size and density. More detailed modeling approaches, such as those of Harlow and Wei [4], Wang et al [5] or Shi and Mahadevan [6] attempt to treat the entire pitting corrosion-fatigue (C-F) process from pit nucleation and growth through to crack nucleation and growth. In order to apply these models, the electrochemical environment that the corroded component is exposed to must be sufficiently characterized. Quantifying the specific corrosive environments for individual aircraft has proven difficult to accomplish for shipboard naval aircraft, and is subject to a wide range of variability due to the global geographic

dispersion of the fleet. Alternatively, treating shallow notches as semi-circular cracks ignores the crack nucleation and short growth fraction of total life, which can be substantial, especially at lower stress levels. This can result in grossly conservative life predictions which render the analysis effectively useless as a fleet management tool. A more general limitation for the implementation of any of the previously mentioned analytical methods is the inability to adequately characterize the state of corrosion on a specific component, once corrosion is detected. Ultimately, the detailed life prediction analysis is then reduced to a qualitative comparison of the damaged component corrosion severity with respect to a known database of surface corrosion damage from which the prediction was derived.

To assist NAVAIR fleet maintainers in providing disposition decisions for corrosion damaged components, this research program was focused on developing quantitative fatigue modeling algorithms that provide objective measures of the reliability and risk associated with continued flight operation. In addition, any analytical methods developed must be compatible with the current NAVAIR fleet life tracking approach of a deterministic strain-life fatigue damage index.

METHODS

CORROSION-FATIGUE TEST DATA

Fatigue tests on corroded AF1410 steel unnotched flat plates were conducted as part of this research program to provide a robust set of test results for C-F model development. Two sets of test specimens were fabricated, and are herein referred to as “Batch A” and “Batch B.” The Batch A test specimens were grit-blasted after heat treatment, but prior to corroding. Batch B specimens were hand polished prior to corrosion, and were not grit-blasted. Test specimen fabrication, corrosion and test results for the Batch A set are described by Hoppe, et al. in a program report [7], and detailed descriptions for the Batch B set are included in Rusk, et al. [8]. All of the test plates that failed in the corroded area had cracks that initiated from small semi-elliptical notches that formed as a result of the corrosion process, except for the critical crack on one Batch B specimen.

CORROSION SURFACE IMAGING

For any quantitative assessment of corrosion severity, surface topology data with sufficient resolution to capture the important characteristics of the features that cause fatigue cracking is required. Measurements of the corrosion topography on the fatigue test plate specimens were made after they were corroded and cleaned, but prior to fatigue testing. The instrument used was a WYKO NT-8000 white light interferometer, which is capable of a lateral resolution of $0.2 \mu\text{m}$ and a vertical resolution of 3 nmi. With the optics and software options chosen for the corroded areas, the lateral resolution was $7.66 \mu\text{m}$ per pixel and the vertical resolution tended toward $0.1 \mu\text{m}$. A single scan, or individual topographic image, obtained using the parameters described above is approximately 2.5 mm x 1.9 mm or 320 x 240 pixels in size. Using a high-accuracy motorized stage, a series of these individual scans were taken automatically on the C-F test plate until an 11 x 11 mm area was covered. The individual images were automatically stitched

together by the software to make a larger topographic image that represented 11 mm x 11 mm of area and was approximately 1442 x 1442 pixels. Once a large stitched image was created, a stage-positioning program was implemented to move the test plate specimen under the objective lens by 10 mm to start the next 11 mm x 11 mm measurement, allowing for 1 mm of overlap. A completed topographic image of the corrosion patch on a fatigue test plate was approximately 41 mm x 41 mm (5365 x 5365 pixels). This technique of using an automatic stitching function and using a stage positioning program to increment and cover larger areas was implemented to accommodate computer memory storage constraints created by the large area of interest. An example of a complete corrosion patch image is shown in figure 1.

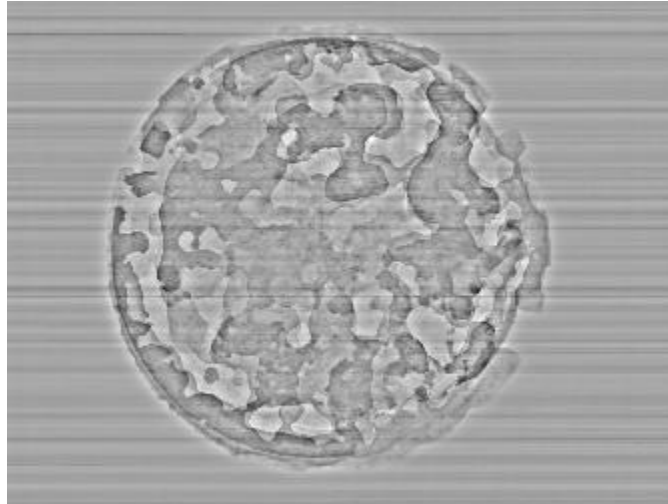


Figure 1: Example of a Stitched Topographic Image (41 mm x 41 mm) of a Corrosion Patch on a Fatigue Test Plate

The image stitching process introduces errors in the depth measurements, due to average tip and tilt values that differ for each individual image. Stitching the individual images together produces a “waviness” in the stitched image that is not present on the actual surface. This “waviness” can be removed by applying a Gaussian high-pass filter to the raw stitched image to remove the low-frequency components of the data. A Fast Fourier Transform (FFT) Gaussian filter was applied to all of the stitched corrosion images of the test plates, which removed all frequency components with a spatial wavelength greater than 8 mm. The mean surface height was also zeroed to remove any tip and tilt in the final stitched image.

CORROSION NOTCH BASED MODELING

The previously discussed fatigue test data demonstrated that the presence of shallow notch-like dimples on the corroded surfaces of AF1410 steel are the principle cause of early fatigue failures. It therefore stands to reason that traditional notched fatigue analysis techniques may be adapted to predict these early fatigue failures if methods of adequately accounting for the large number of notches and the complexity of the corroded surface can be developed. This approach

has the added benefit of being compatible with the flight certification requirements and fleet life tracking algorithms currently in use by NAVAIR. Stress and strain-based notched fatigue approaches both rely on a defined relationship between the geometric stress concentration factor (K_t) of a notch and the corresponding ratio of unnotched fatigue endurance limit to notched endurance limit (fatigue notch factor – K_f), which is generally referred to as the notch sensitivity (q) factor or ratio [9, 10].

$$q = \frac{K_f - 1}{K_t - 1} \quad (1)$$

Equations proposed by Peterson [11] and Neuber [12] to quantify notch sensitivity are based on experimental data of geometrically notched and unnotched fatigue test specimens. Both equations use the notch root radius as the independent variable, and a single parameter describes the fit to the experimental data. Elastic stress concentration factors for geometric notch geometries are generally found through handbook solutions [13, 14] or finite element analysis. No handbook solution exists that could describe the complex, chaotic surface of a corrosion-damaged part, and attempts at performing conventional finite element analysis on the AF1410 C-F plates proved to be greatly time consuming and computationally intensive. Approximate methods of estimating stress concentration would therefore be necessary.

Based on the test results described previously, the critical corrosion notches can be assumed to be semi-elliptical in shape, as a first approximation. UDRI developed a notch metric (μ) equation to estimate the peak stress concentration value for an idealized semi-elliptical notch shape using the overall notch width (W), height (H) and depth (D) dimensions.

$$\mu = \frac{WD}{H(W/2 + D)} \quad (2)$$

$$K_t = 1 + 2\mu \quad (3)$$

The K_t equation was refined by performing a finite element sensitivity study for a range of notch metric values, with the new equation expressed as:

$$K_t = 1 + 2.1\mu + 0.27\mu^2 \quad (4)$$

The refined equation has a maximum relative error of less than $\pm 0.4\%$ for a range of notch metric (μ) values from 0.57 to 2.13, as shown in figure 2.

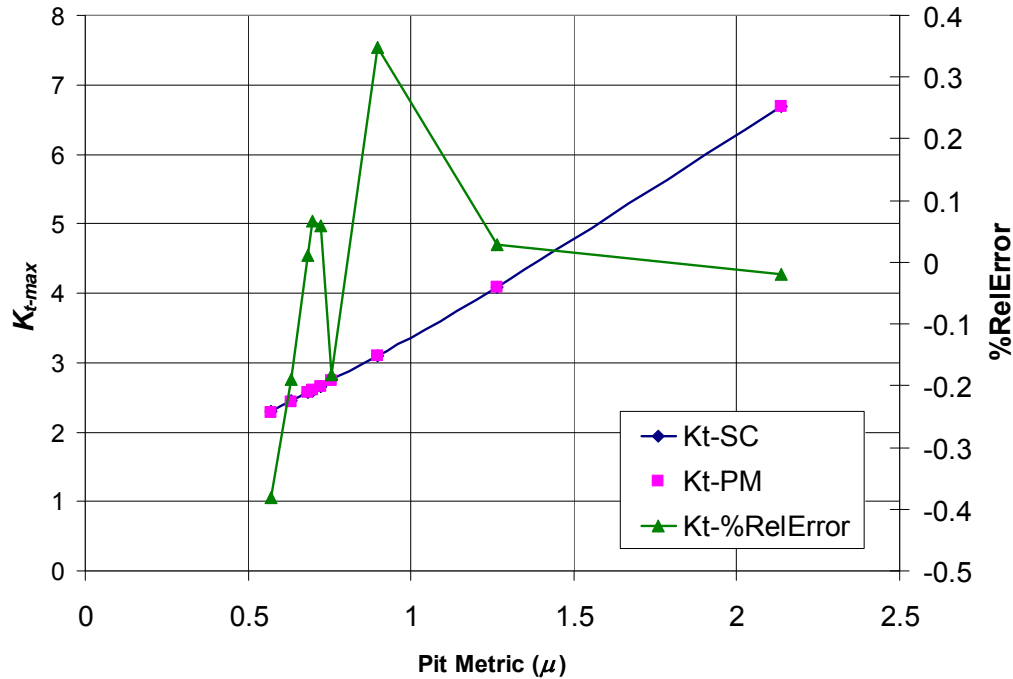


Figure 2: K_t Error in Revised Notch Metric Equation for Range of Metric Values

The notch height and depth dimensions can also be used to estimate the notch root radius (R) value by fitting a semi-circle through three points. The equation used for the notch root radius was derived as:

$$R = \frac{D}{2} + \frac{H^2}{8D} \quad (5)$$

CORROSION-FATIGUE NOTCH SENSITIVITY MODEL CALIBRATION

Using the notch metric equations and the measured dimensions of the critical corrosion notches on the Batch A and Batch B C-F test plates, the approximate K_t values of each notch can be calculated. The fatigue notch factor for each test plate was determined by the crack initiation test life, and an unnotched probabilistic strain-life (PSL) prediction. The PSL curve is based on smooth, unnotched uniform gage strain-life coupons tested under fully reversed, constant-amplitude loading per ASTM E606 [15] for low-cycle tests, and per ASTM E466 [16] for high-cycle tests. High-cycle coupons were subjected to periodic overstrains during testing. The high-cycle portion of the PSL curve was modeled using the Random Fatigue Limit model of Pascual and Meeker [17]. The low-cycle portion of the curve was modeled using the Coffin-Manson equation (references 9 and 10); with the equation coefficients derived from a log-log regression of the elastic and plastic strain components of the test data. The life scatter about the nominal curve was assumed to be distributed lognormally, with the variance estimated from the root-mean-squared error (RMSE) of the regression. Mean stress effects are accounted for in the

predictions by the Smith-Watson-Topper equation as formulated by Socie [18]. The strain-life test data and prediction bounds of the PSL model are shown in figure 3.

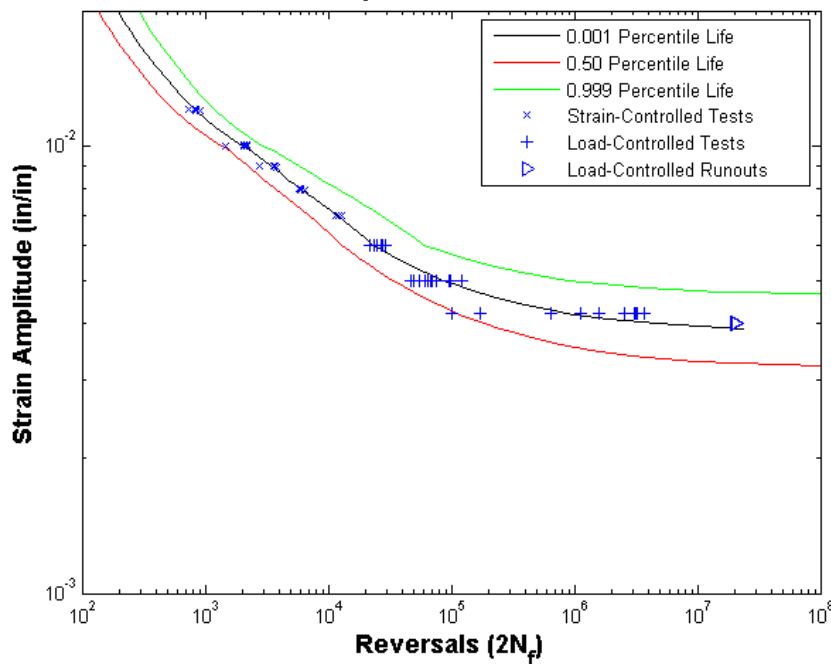


Figure 3: AF1410 PSL Curve, Uniform Gage Specimens

Fatigue notch factor (K_f) in notched components has traditionally been defined as the ratio of the unnotched to notched stress at lives of 10^6 to 10^7 cycles, or the endurance limit stresses. For the AF1410 C-F test specimens, the endurance limit for an individual corroded plate is unknown, since most plates were tested to a finite life at a single stress level. An alternative method of calculating K_f is to increase the nominal stress in the unnotched life prediction until the median predicted life matches the notched test life. The ratio of nominal stresses from the unnotched prediction and the notched test life then defines K_f . This was the approach used to calculate C-F notch factor (K_{fc}) values for all of the AF1410 C-F test specimens. Local plasticity effects are accounted for in the predictions by the Neuber notch-strain relation under nominally elastic conditions (references 9 and 10). The K_{fc} predictions were combined in equation (1) with the K_t values for critical notches to give a C-F notch sensitivity (q_c) distribution for each C-F test specimen, which are plotted as a function of the equivalent notch root radius (R) (figures 4 and 5). The plots display the q_c distributions in terms of median values, with error bars showing the ± 3 standard deviation (σ) bounds for each test plate estimate. Only results for test plates that failed from corrosion notch cracks are plotted. Also, none of the results from the 12-hr exposure Batch A tests are plotted, as these specimens were deemed to have a level of corrosion damage so severe that continued flight operation of an airframe component with that level of damage would not be allowed.

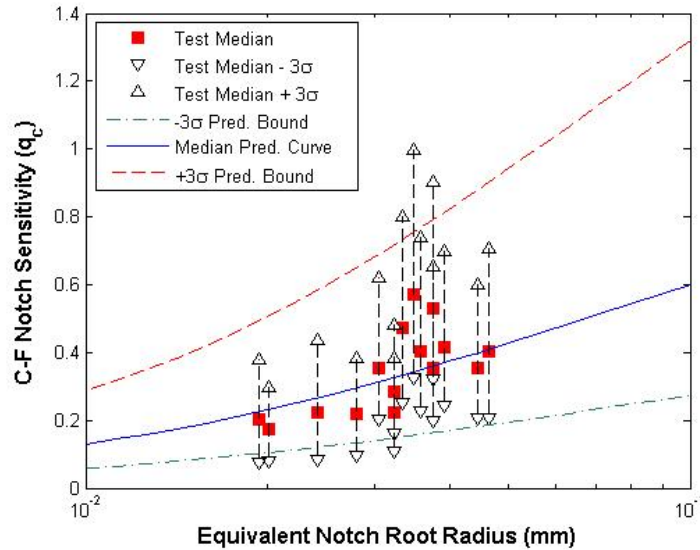


Figure 4: Peterson Notch Sensitivity Model Fit, AF1410 Batch A C-F Plates

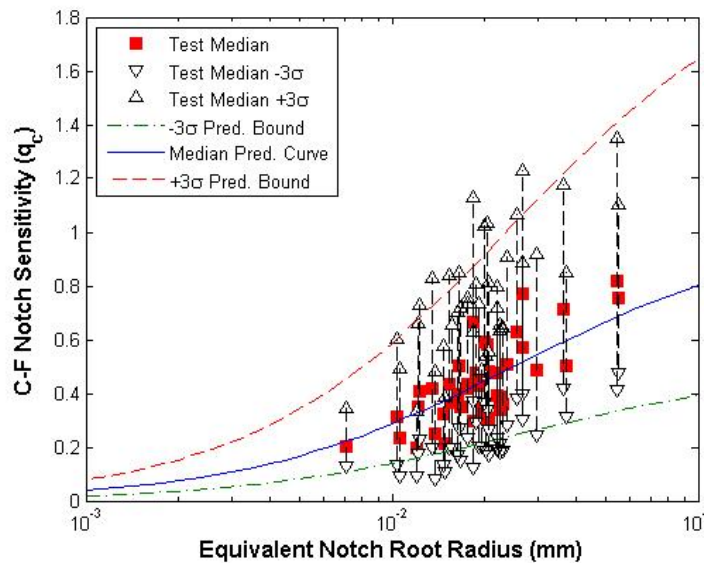


Figure 5: Peterson Notch Sensitivity Model Fit, AF1410 Batch B C-F Plates

Before attempting to model the q_c versus notch R relationship, an understanding of the sources of uncertainty is necessary. The q_c distributions shown in figures 4 and 5 are a product of the predicted fatigue life scatter for each test specimen, but do not include the uncertainty in the notch K_t values due to measurement and approximation errors. For this analysis, these errors are assumed to be much smaller than the fatigue life scatter. In traditional notched fatigue analysis, statistical means or medians of fatigue tests results are used to estimate q for a given notch geometry, which has the effect of eliminating fatigue scatter from the q versus R relationship. For the type of C-F tests described here, the true fatigue life scatter is unknowable, since it is

impossible to create replicate test specimens with identical corrosion features for testing. Each test specimen is thus a unique representation of all possible corrosion states that a component may exhibit. For the purposes of the NAVAIR C-F modeling effort, it was not necessary to model all possible corrosion states on a component, but only those realizations that are representative of the corrosion damage that is found on fleet components. Because the fatigue life scatter cannot be reduced from the q_c estimates, it must be propagated through to the model calibration phase, since this source of uncertainty is now convoluted with the errors of fit for any model that is proposed to define the q_c versus R relation.

When fatigue scatter effects are factored out of the q equation inputs, the value of q ranges from zero for no notch effect ($K_f = 1$) to unity for a full notch effect ($K_f = K_t$). When fatigue scatter effects are included in the q equation inputs, the values of q can range beyond 0 and 1. Values of q_c less than zero would generally not occur in C-F specimen tests, except at very light corrosion exposures and low stress levels. However, values of q_c greater than 1 can easily occur at the lower probability bounds of the q_c distributions, as can be seen in figures 4 and 5. Initial fitting of the C-F q_c data was done using standard notch sensitivity equations. Both Peterson and Neuber notch sensitivity equations were fit to the median values of the q_c distributions using least-squares regression, with the Peterson equation (6) giving a much better overall fit to the data sets.

$$q = \frac{1}{1 + \alpha/R} + \varepsilon \quad (6)$$

Standard least-squares regression theory assumes that the errors of data fit (ε) about the regression curve are independent, have a mean of zero and constant variance. It is also statistically advantageous that they be normally distributed, for example to develop confidence intervals on the fitted parameter values [19]. The residual errors from the fit of equation 6 were shown to have skewed normal probability plots, indicating that the error structure for the regression equation does not closely conform to a normal distribution. A refinement to the Peterson regression consists of treating the errors of fit as being normally distributed in log space by taking the log of both sides of the equation. This also limits the q_c value to an asymptotic lower bound of zero, as discussed previously. The form of the equation used in the final regression fit is:

$$\log(q_c) = -\log(1 + \alpha/R) + \varepsilon \quad (7)$$

The residual errors from the fit of equation 7 were shown to have a much better fit to a normal distribution, indicating that the error structure for the data is more accurately described by the log form of the original equation. Parameter values for the regression fits are listed in table 1, along with other fit statistics.

Table 1: Regression Fit Statistics for Log-Peterson Notch Sensitivity Equation on AF1410 C-F Plates

| Test Data Set | Parameter Value (α) | α 95% Conf. Bounds | RMSE | R ² |
|---------------|------------------------------|---------------------------|-------|----------------|
| Batch A | 0.0669 mm | 0.0525, 0.0813 | 0.263 | 50.1% |
| Batch B | 0.0269 mm | 0.0234, 0.0303 | 0.240 | 55.1% |

Using the RMSE value of the regression as the estimate for the error standard deviation, $\pm 3\sigma$ prediction bounds were generated for the Peterson fits over a range of notch root radius values. The bounds are plotted along with the regression curves in figures 4 and 5, and show that the $\pm 3\sigma$ probability bounds for the group of q_c distributions are reasonably captured by the prediction bounds from the new model formulation. This was not the case for the original formulation. The prediction bounds become very broad at large notch root radii values, so the error structure of the regression model may not be appropriate for notch root radii far outside the range of the data sets.

FAST FOURIER TRANSFORM APPROACH FOR STRESS CONCENTRATION MAPPING

Determining the critical corrosion notch on a corroded component is relatively straightforward if the component has already failed, as the exposed fracture surfaces preserve the history of crack nucleation and growth from the surface features that initiated the critical crack. A much more difficult task is distinguishing which corrosion notch or collection of notches will cause a critical crack on a component that has yet to fail. Initial attempts were made at performing conventional finite element analysis (FEA) on the corroded surfaces of the AF1410 C-F plates using the topography measurements from WLI surface scans. However, the complex and chaotic corroded surface topology required geometric modeling simplifications that introduced significant error in the stress concentration predictions. The simplified FEA models also proved to be greatly time consuming and computationally intensive to build and run (see reference 7). An alternative approach was to develop an approximate elasticity solution using a FFT of the corroded surface data to represent the actual surface profile as a linear combination of sinusoidal components in the frequency domain. Because each of the frequency components was a smooth, continuous function, one could estimate the stress variation over the surface of each frequency component with an approximate elasticity solution. The stress values corresponding to each frequency component were then recombined, via an inverse FFT, to provide an estimate of the stress field. The overall approach for stress concentration factor modeling of corroded surfaces is depicted in figure 6.

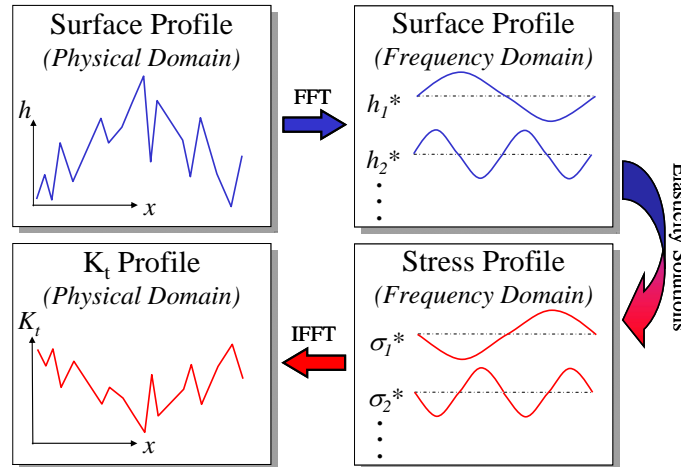


Figure 6: Elasticity Approach for Corroded Surface Modeling

The elasticity stress function solution was developed based on observations from analyses of axial load components with sinusoidally varying surface geometries. For shallow surface height variations, the surface stress varies 180 deg out of phase from the local surface height. From the elasticity solution, a simple expression was developed that defined the stress variation over a sinusoidal surface in terms of the surface profile parameters (height and wavelength in each surface direction) and the applied axial loading (figure 7).

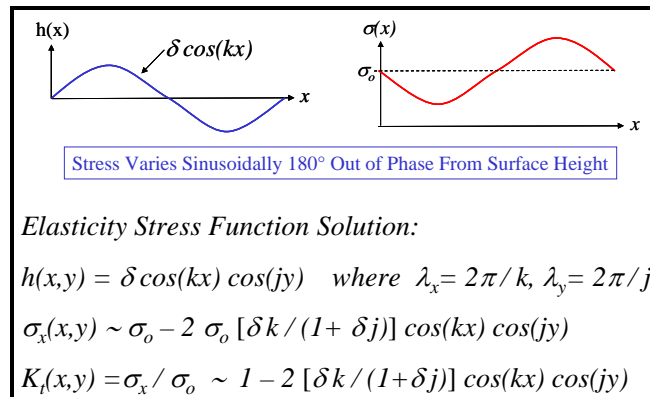


Figure 7: Elasticity Solution for Each Surface Profile Frequency Component

A series of FEAs was performed to estimate the stress concentration factors for a variety of idealized corroded surfaces having increasing complexity. The elasticity solution approach was applied to each of these surfaces and correlated well with the finite element results. An example is figure 8, which depicts the elasticity and finite element solutions corresponding to an axial load applied to a surface with a sinusoidal variation in both surface directions. These results indicated that the elasticity solution accurately predicted both the amplitude and spatial variation of the stress profile.

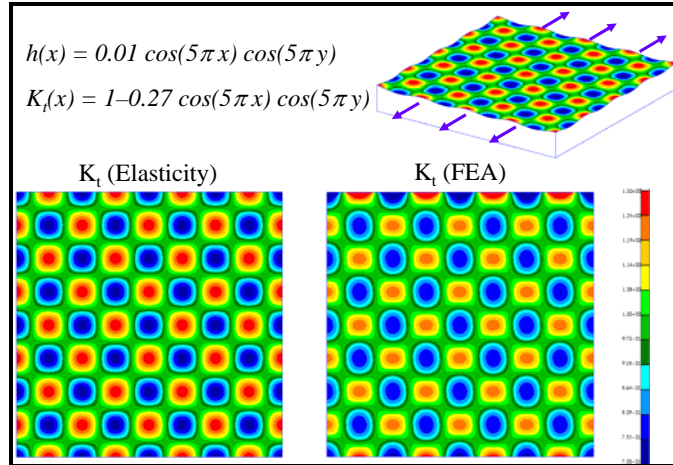


Figure 8: Elasticity Solution 2-D Single Frequency Validation Problem

ESRD and UDRI performed a series of detailed FEAs to determine the accuracy of the individual frequency component elasticity solutions over a wide variety of conditions. These results, shown in figure 9, indicated that the elasticity solution was accurate over most conditions, except when the surface height of one of the frequency components was large compared to the corresponding wavelength. Review of measured surface profile data from AF1410 C-F specimens found that the surface heights were significantly smaller than the corresponding wavelengths. This implied that the elasticity solution would be used in the most accurate regime and remained viable for estimating the severity of actual corroded surfaces.

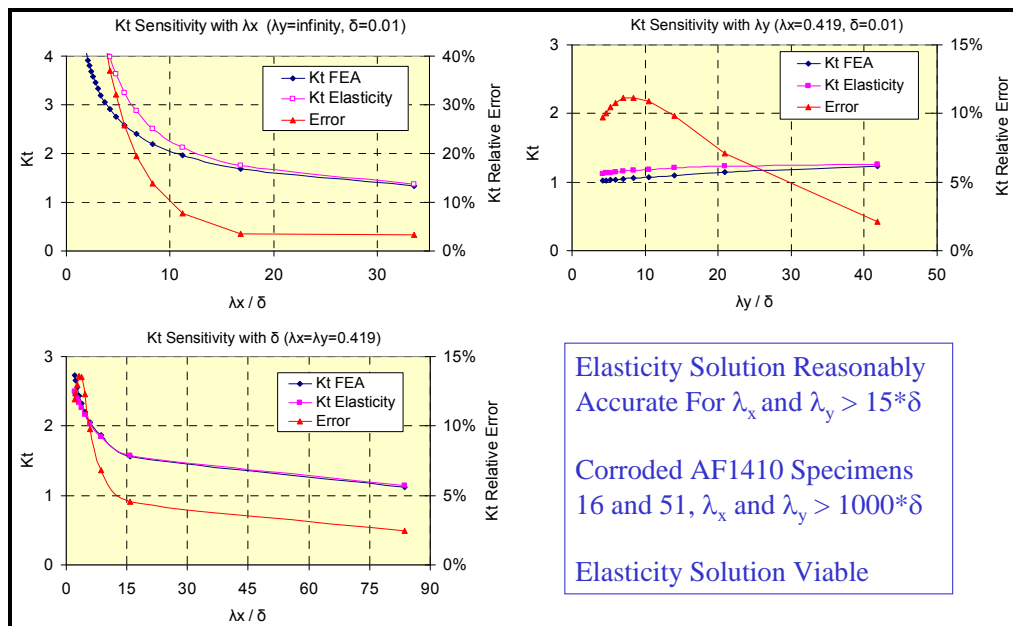


Figure 9: Accuracy of Individual Frequency Component Elasticity Solutions

FEAs were also performed to determine if the individual frequency components could be superimposed to represent the overall surface stress profile. The justification for superposition was based on the observation that the effects of multiple stress concentrations factors, such as a notch within a notch, were known to combine as the product of the individual stress concentration factors as indicated in figure 10. When the individual elasticity solutions were inserted in the product expression and higher order terms were neglected, the total stress concentration factor was estimated by a summation of terms related to the stress state of the individual frequency components.

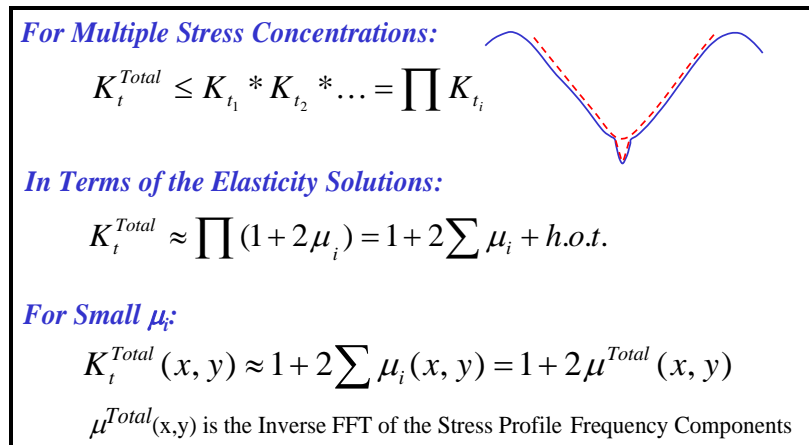


Figure 10: Combined Stress Concentration Factor Solution

Figure 11 depicts the elasticity (FFT), FEA, and boundary element solutions corresponding to an axial load applied to a component having a surface geometry composed of three sinusoids. These results indicated that the superposition of the individual elasticity solutions accomplished via the inverse FFT accurately predicted the amplitude and spatial variation of the stress gradient over a complex surface profile.

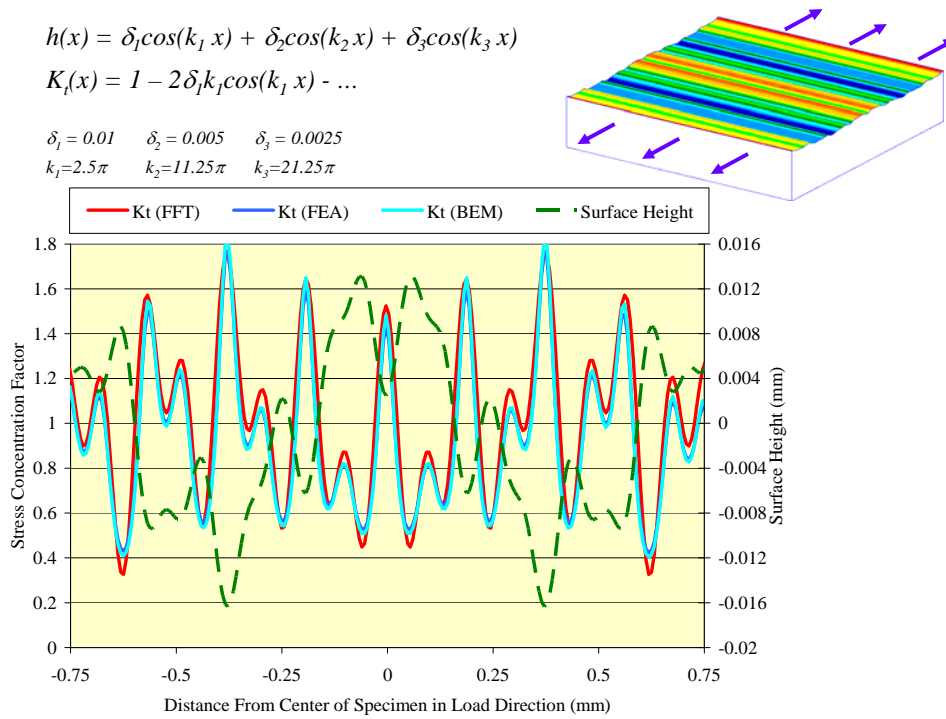


Figure 11: Accuracy of Elasticity Solution Approach on a Complex Surface

The elasticity approach was applied directly to an AF1410 corroded surface geometry from one of the test specimens that had a large number of fatigue cracks at failure. A number of crack locations on the test specimen were identified and compared to the predicted stress concentrations near the crack origins. Figure 12 shows the surface height profile and corresponding stress concentration factor contour plot from the elasticity solution in a local region where fatigue cracks occurred. The loading was applied in the vertical direction and the cracks appeared to form and grow along the step risers between corroded regions of different surface heights.

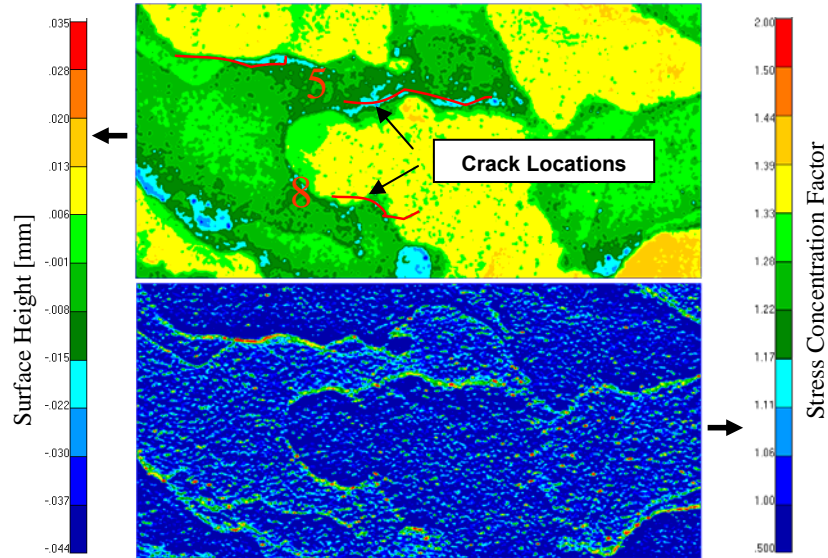


Figure 12: Zoomed Surface and Stress Concentration Profiles in AF1410 C-F Test Specimen

The comparison showed a high degree of correlation between the areas of local high stress concentration predicted by the elasticity solution and the actual locations of fatigue cracks on the test specimen. The conclusion was that the elasticity solution possessed sufficient accuracy to identify the stress concentrations of critical surface features that cause fatigue cracking in the AF1410 C-F test plates, given sufficient resolution of the WLI surface profile scan. Further details of this portion of the model development can be found in reference 7.

REGION OF INTEREST ANALYSIS

The elasticity solution can be used to identify local stress concentration areas that may initiate fatigue cracks under loading. However, an automated method must be defined to enable the extraction of notch critical dimensions (width, height, and depth) from the geometric features that cause the local stress concentrations, on corroded surfaces with hundreds or thousands of notches present. For this research program, standard and custom software plug-ins for ImageJ [20] were used to develop a filtering algorithm that sorts through a K_t map looking for pixels of high K_t values above a certain threshold. The process starts by creating a combined binary image of all pixels in the WLI image with a surface height below $1 \mu m$ and all pixels with K_t values greater than 1.3 for Batch A, and greater than 1.1 for Batch B. An ImageJ plug-in called Particle Analyzer identifies Region of Interest (ROI) boundaries from groups of contiguous pixels with binary values of one and with areas of size equal to 36 square pixels for Batch A and 4 square pixels for Batch B. All regions of smaller area are ignored. A lower K_t threshold value and ROI area threshold value for the Batch B specimens were chosen to increase the probability of finding the critical notches on specimens with the lightest amounts of corrosion. The major and minor axes dimensions of the enclosed ROI area are extracted using the Measurement utility in ImageJ. Also defined is the major axis orientation with respect to the image orientation. The depth of each ROI feature is determined by a net distance measurement between a reference

plane defined from height measurements taken at the four corners of the WLI image outside the corroded region, and the maximum depth pixel in the ROI area. A more detailed description of the ROI feature definition procedures is listed in reference 22.

Examples of ROI feature definition for corroded surfaces are shown in figure 13 on a C-F specimen K_t map, and in figure 14 for service induced corrosion damage on an F/A-18C/D arrestment shank.

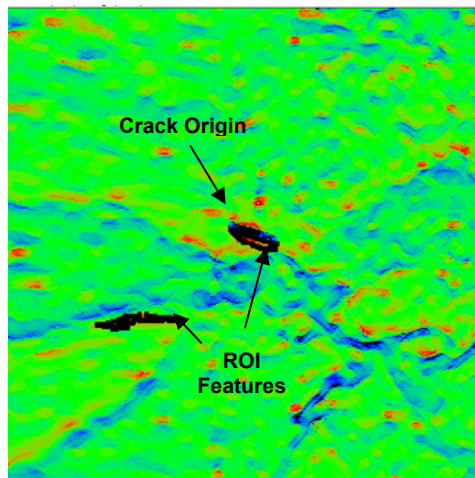


Figure 13: ROI Feature Detection on K_t Map of C-F Specimen

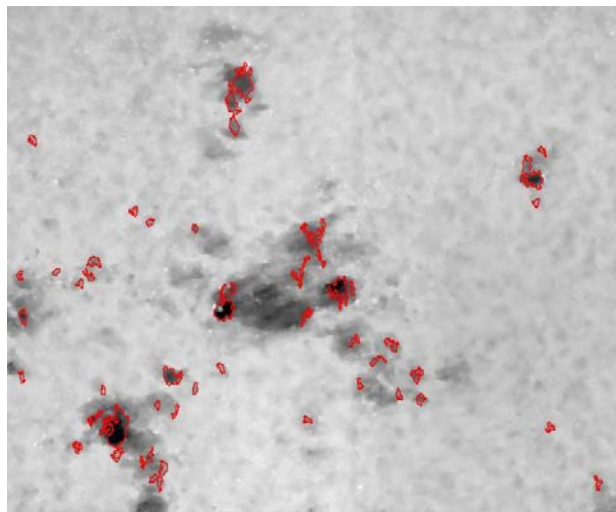


Figure 14: F/A-18C/D Arrestment Shank Corroded Surface WLI Profile with ROI Features Marked in Red

UNCORRODED CORROSION-FATIGUE PLATE PROBABILISTIC LIFE PREDICTION

Probabilistic crack initiation life predictions on uncorroded AF1410 Batch A and Batch B C-F test plates were made using the baseline AF1410 PSL curve model described previously. To account for the difference in geometry between the strain-life coupons and the C-F test plates, Weibull's sizing method based on weakest-link principles was modified based on the gage section surface areas of the respective test specimens [21]. Reliability values from a strain-life prediction based on coupon test data (R_0) are modified by raising to the power of the ratio of the C-F plate gage section area (A_p) to the coupon test area (A_0), to give the reliability for the C-F plate (R_p).

$$R_p = R_0^{A_p/A_0} \quad (8)$$

The AF1410 strain-life coupons had a cylindrical gage section with a 0.20 in. diameter and 0.06 in. gage length, giving a gage surface area of 0.377 in.². The gage surface area for the Batch A C-F plate is 41.25 in.², and is 26.25 in.² for the Batch B plate.

LIFE PREDICTION USING THE EQUIVALENT STRESS RISER MODEL

The ROI search algorithm, along with the notch metric equations and the Peterson notch sensitivity equation fit to the Batch A and Batch B C-F test results, essentially defines an Equivalent Stress Riser (ESR) model for corrosion damaged AF1410 steel with machined and abrasive blasted surface finishes. The set of notch K_{fc} values derived from the ROI set is sufficient to make a probabilistic strain-life prediction of the crack initiation life of a corrosion damaged test specimen. For a component with a uniform stress field in the corroded region, the cumulative density function (CDF) of the survivability in the presence of the j^{th} single corrosion notch can be defined as:

$$R_j(N_i) = R_j(N_i | K_{fc-j}, \sigma(t)) \quad (9)$$

where the independent variable N_i is the number of cycles to crack initiation, and the CDF is conditional on the values of K_{fc-j} and the nominal stress history $\sigma(t)$. For a component with n corrosion notches present, the notches can be treated as a series system, assuming they are all independent. This is a reasonable assumption, since individual notches that are in close proximity are usually lumped together into one large notch by the ROI algorithm. The CDF of the survivability then becomes:

$$R(N_i) = \prod_{j=1}^n R_j(N_i | K_{fc-j}, \sigma(t)) \quad (10)$$

For large numbers of notches, calculating the CDF for every individual K_{fc} value is computationally intensive and unnecessary in most cases, since the reliability of series systems is dominated by the individual components that have the highest failure probabilities. To make the solution more computationally tractable, the set of K_{fc} values can be sorted into histogram bins, and the CDF is then calculated only once for each bin value of K_{fc} . The CDF of the component survivability for m histogram bins then becomes:

$$R(N_i) = \prod_{j=1}^m \left[R_j(N_i | K_{fc-j}, \sigma(t)) \right]^{h_j} \quad (11)$$

where h is the number of K_{fc} occurrences in each bin. The contribution of the uncorroded surface area portions to the overall reliability can be considered by adding an additional histogram bin with a K_{fc} value of 1.0, and with an exponent value that is the ratio of the total surface area to the strain-life coupon gage area, as in equation (8). Some discretization error is introduced into the life prediction CDF through the use of histogram K_{fc} values instead of exact values, but this error can be minimized by extracting the three or four largest K_{fc} values on the surface and assigning each one to an individual histogram bin. The remaining K_{fc} values can then be grouped into other histogram bins.

LIFE PREDICTION UNCERTAINTY FROM THE EQUIVALENT STRESS RISER MODEL

To develop confidence bounds on ESR model predictions, the sources and levels of uncertainty in the model input parameters must be defined. A list of the major sources of uncertainty for each part of the model are identified as:

1. PSL curve
2. WLI scan resolution
3. WLI median filtering
4. Elasticity solution K_t transformation
5. ROI K_t and pixel area thresholds
6. ROI depth measurement
7. Notch metric idealization
8. Notch sensitivity q curve
9. K_{fc} histogram discretization

Uncertainty in the PSL curve arises from the finite sample size of the strain-life test data used to fit the PSL model. The AF1410 strain-life data set consisted of 65 samples, with 36 in the high-cycle region and the remainder in the low-cycle region. High-cycle fatigue (HCF) data were fit to the random fatigue limit (RFL) model described previously. This model has five parameters defined as fatigue curve coefficients (β_0, β_1), scale parameter (σ) and fatigue limit location and scale parameters ($\mu_\gamma, \sigma_\gamma$). The covariance structure of the model fit was investigated by performing bootstrap resampling of the test data, and generating MLE parameter values for each

bootstrap set. 115 bootstrap sets were generated from the HCF data. The covariance matrix of the MLE parameter sets was used to define correlated distributions of parameter value uncertainty for the RFL model fit. The final RFL parameter uncertainty model is defined as parameters σ and $-\mu_\gamma$ being independent, lognormally distributed with log means of -6.5543 and 1.7054, and log standard deviations of 0.1675 and 0.00196, respectively. The parameter σ_γ is normally distributed, with a mean defined by the equation:

$$E[\sigma_\gamma | \mu_\gamma] = -3.3645 - 0.61903\mu_\gamma \quad (12)$$

and a standard deviation of 0.00545. The parameter β_1 is normally distributed, with a mean defined by the equation:

$$E[\beta_1 | \mu_\gamma] = 30.745 - 5.8326\mu_\gamma \quad (13)$$

and a standard deviation of 0.1063. The parameter β_0 is also normally distributed, with a mean defined by the equation:

$$E[\beta_0 | \beta_1] = 10.014 - 6.1643\beta_1 \quad (14)$$

and a standard deviation of 0.0477. Low-cycle fatigue test data were modeled using a bilinear log-log fit of the Coffin-Manson relation described previously. The elastic portion of the Coffin-Manson curve was assumed fixed. The slope (B) and intercept (A) errors of the plastic strain regression curve are Student-t distributed when transformed by the sample standard deviation (S) and S_{xx} .

$$\frac{(\hat{\beta} - \beta)}{S / \sqrt{S_{xx}}} \sim t_{n-2} \quad (15)$$

$$\frac{\hat{A} - A + \bar{x}(\hat{\beta} - \beta)}{S / \sqrt{n}} \sim t_{n-2} \quad (16)$$

$$S = \sqrt{\frac{\sum_{i=1}^n (y_i - \bar{y})^2}{n-2}} \quad (17)$$

$$S_{xx} = \sum_{i=1}^n (x_i - \bar{x})^2 \quad (18)$$

The variance ratio error for the plastic strain regression fit is Chi-squared distributed.

$$\frac{(n-2)S^2}{\sigma^2} \sim \chi_{n-2}^2 \quad (19)$$

Statistical values for the lower and upper plastic strain regression curves are listed in table 2.

Table 2: Statistical Values for Plastic Strain Regression Parameters

| Curve | Sample Size (n) | \hat{A} | \hat{B} | S | S_{xx} | \bar{x} |
|-----------|---------------------|-----------|-----------|--------|----------|-----------|
| Plastic 1 | 7 | 4.387 | -0.5688 | 0.0598 | 2.5439 | -8.1264 |
| Plastic 2 | 14 | -0.5799 | -1.31 | 0.124 | 1.5741 | -5.9099 |

Strain-life test data points at a total strain amplitude of 0.9% (in./in.) were not included in the linear regressions of the upper and lower plastic curves described previously. At total strain amplitudes between 0.8% (in./in.) and 1.0% (in./in.), a cubic spline interpolation is fit through the upper and lower plastic curves and through the 0.9% (in./in.) plastic mean point. The mean (μ) error at this strain level is Student-t distributed.

$$\frac{\bar{y} - \mu}{S/\sqrt{n}} = \frac{8.1367 - \mu}{0.1491/\sqrt{4}} \sim t_{n-1} \quad (20)$$

WLI scan resolution uncertainty is centered around the required image spatial and depth resolution necessary to capture the corrosion notch geometry characteristics while minimizing the error in subsequent notched fatigue model calculations. In cases of light or moderate corrosion, insufficient image resolution may introduce errors in the subsequent notch geometry characterization. Without prior knowledge, the resolution chosen for most of the WLI corrosion scans was a lateral resolution of 7.66 μm per pixel and a vertical resolution of 0.1 μm , but it is not known if that resolution is sufficient to minimize notch geometry characterization errors. Sensitivity studies to determine the effect that WLI resolution has on life prediction error were not conducted due to program time constraints. However, they are considered necessary to determine the contribution that WLI scan resolution has to the overall life prediction error.

Similarly to WLI scan resolution, WLI median filtering can affect the amount of error in the corrosion notch geometry characterization and elasticity K_t solution. Sensitivity studies to determine these effects on life prediction error were not conducted due to program time constraints. Uncertainties in the elasticity K_t solution are tied to WLI scan resolution, but are also a function of the approximate nature of the method. These uncertainties may also be affected by WLI median filtering that is applied prior to elasticity solution calculations. Therefore, sensitivity studies to characterize the individual errors of each uncertainty source should also be expanded to account for the interaction of the multiple sources of error on the final life prediction error.

Corrosion notch geometry values that are extracted by the ROI analysis are dependent on the WLI image and elasticity transformations described previously, but also on the ROI K_t and pixel area thresholds, and the notch depth measurement procedure. Estimates of the notch geometry measurement error were made by comparing the notch geometry values extracted by the ROI analysis to optical measurements of the critical corrosion notches on Batch A and Batch B specimens. Errors in notch geometry measurements are assumed to be independent normally distributed with zero mean, and a notch width standard deviation of 20 μm , a notch height standard deviation of 10 μm and a notch depth standard deviation of 3 μm . Bias in actual notch measurement errors was ignored.

Errors in calculating K_t values using the notch metric equation were estimated from the data in figure 2, and are assumed to be normally distributed with a mean of zero and a standard deviation of 0.00595. Errors in the notch radius calculation are assumed to be normally distributed with a mean of zero and a standard deviation of 3.5 μm ; however, no data comparisons were available to base this number on. Errors in the log Peterson notch sensitivity equation parameter fit were estimated by bootstrap resampling the median notch sensitivity data from the Batch A and Batch B tests, similar to the process used for the PSL test data. The error samples fit a normal distribution with a mean of zero, and Batch A standard deviation of 6.46 μm and Batch B standard deviation of 1.75 μm . Discretization error from the use of histogram K_{fc} values instead of exact values was not investigated due to program time constraints. Except for the correlations describing the PSL curve parameters, all error source characterizations are assumed independent in subsequent uncertainty calculations.

EQUIVALENT STRESS RISER MODEL CALIBRATION USING EXTREME VALUE STATISTICS

The approach that was previously described for calibrating the notch sensitivity equation in the ESR model treats the critical corrosion notch as a single event on an individual test specimen. In reality, there are many notches present that can potentially crack, but it is generally the first occurrence of a crack from the notch with the largest K_{fc} value that will lead to final failure of a specimen. This is in essence an extreme value problem, in that the critical notch K_{fc} represents the maximum value of a large sample from the population of K_{fc} values for all test specimens. In the interest of improving model calibration and predictive capability, an extreme value approach to calibration of the ESR model was proposed. If just one C-F specimen is considered – the i^{th} specimen – then each ROI (labeled by the index j) will have a probability defined by the model, a probability density function (PDF), and a CDF. These PDFs and CDFs represent the parent population from which the K_{fc} 's for each ROI are sampled. Starting with the Peterson notch sensitivity equation, let the CDF for a given ROI (j) from a given specimen (i) (describing the model) be described by:

$$F(K_{fc_i}, K_{ti,j}, r_{i,j} | \alpha, \sigma) = F(\log(K_{fc_i} - 1) | \log(K_{ti,j} - 1) - \log(1 + \alpha / r_{i,j}), \sigma) \quad (21)$$

where K_{fc-i} is the specimen K_{fc} value, then this CDF applies for all ROIs, including the critical ROI as individual samples from the population. However, the CDF for the entire sample needs to be known. The CDF for the extreme value for this specimen is the product of the CDFs for all ROIs on this specimen. Letting G and g be the CDF and PDF of the extreme value for this population of ROIs for specimen i , then:

$$G(K_{fc_i} | \alpha, \sigma) = \prod_j F_j(K_{fc_i}, K_{ti,j}, r_{i,j} | \alpha, \sigma) \quad (22)$$

To get the PDF for the extreme value for this set of ROIs, this equation is differentiated with respect to K_{fc} :

$$g(K_{fc_i} | \alpha, \sigma) = \frac{dG(K_{fc_i} | \alpha, \sigma)}{dK_{fc_i}} \quad (23)$$

To construct a likelihood function, the product of the PDFs over all specimens needs to be optimized. Since the log function retains the maximum, a likelihood function as the log of the product can be constructed, which is the same as the sum of logs:

$$L = \sum_i \log(g(K_{fc_i} | \alpha, \sigma)) \quad (24)$$

L must then be optimized for the model parameters. This function can be expanded and simplified. Since g is the derivative of a product, the product rule can be used:

$$\begin{aligned} g(K_{fc_i} | \alpha, \sigma) &= \frac{dG(K_{fc_i} | \alpha, \sigma)}{dK_{fc_i}} = \sum_k \left(f(K_{fc_i}, K_{ti,k}, r_{i,k} | \alpha, \sigma) * \prod_{j \neq k} F(K_{fc_i}, K_{ti,j}, r_{i,j} | \alpha, \sigma) \right) \\ &= \sum_k \left(\frac{f(K_{fc_i}, K_{ti,k}, r_{i,k} | \alpha, \sigma)}{F(K_{fc_i}, K_{ti,k}, r_{i,k} | \alpha, \sigma)} * \prod_j F(K_{fc_i}, K_{ti,j}, r_{i,j} | \alpha, \sigma) \right) \\ &= \prod_j F(K_{fc_i}, K_{ti,j}, r_{i,j} | \alpha, \sigma) * \sum_k \left(\frac{f(K_{fc_i}, K_{ti,k}, r_{i,k} | \alpha, \sigma)}{F(K_{fc_i}, K_{ti,k}, r_{i,k} | \alpha, \sigma)} \right) \end{aligned} \quad (25)$$

Since g is now a product of two factors, the log of these factors is the sum of the logs:

$$\begin{aligned}
L &= \sum_i \log(g(K_{fc_i} | \alpha, \sigma)) = \sum_i \log\left(\prod_j F(K_{fc_i}, K_{ti,j}, r_{i,j} | \alpha, \sigma) * \sum_k \left(\frac{f(K_{fc_i}, K_{ti,k}, r_{i,k} | \alpha, \sigma)}{F(K_{fc_i}, K_{ti,k}, r_{i,k} | \alpha, \sigma)}\right)\right) \\
&= \sum_i \left(\log \prod_j F(K_{fc_i}, K_{ti,j}, r_{i,j} | \alpha, \sigma) + \log\left(\sum_k \left(\frac{f(K_{fc_i}, K_{ti,k}, r_{i,k} | \alpha, \sigma)}{F(K_{fc_i}, K_{ti,k}, r_{i,k} | \alpha, \sigma)}\right)\right)\right) \quad (26) \\
&= \sum_i \sum_j \log(F(K_{fc_i}, K_{ti,j}, r_{i,j} | \alpha, \sigma)) + \sum_i \log\left(\sum_k \left(\frac{f(K_{fc_i}, K_{ti,k}, r_{i,k} | \alpha, \sigma)}{F(K_{fc_i}, K_{ti,k}, r_{i,k} | \alpha, \sigma)}\right)\right)
\end{aligned}$$

This expression does not include any products and should be relatively easy to carry out. It should be noted that there are factors that might be missing in this expression related to the derivative of the CDF (F), to get the PDF (f). For instance, if the model assumes a normal distribution, then the mean is given by:

$$\mu_{i,j} = \log(K_{ti,j} - 1) - \log(1 + \alpha / r_{i,j}) \quad (27)$$

and the standard deviation is given by σ . Then the expression above must include a factor of:

$$1/(K_{fc_i} - 1)\sigma \quad (28)$$

in the second term, inside the inner summation to account for the derivative of the argument of the CDF:

$$L = \sum_i \sum_j \log(\Phi((\log(K_{fc_i} - 1) - \mu_{i,j}) / \sigma)) + \sum_i \log\left(\sum_k \left(\frac{\phi((\log(K_{fc_i} - 1) - \mu_{i,k}) / \sigma)}{\Phi((\log(K_{fc_i} - 1) - \mu_{i,k}) / \sigma)} * \frac{1}{(K_{fc_i} - 1)\sigma}\right)\right) \quad (29)$$

Note that the second term in the above expression uses the index k instead of j . Since the two terms are completely independent, k can be changed to j without loss of generality. The index k was used to make a distinction between the index being differentiated and the rest of the $j-1$ factors in the product. This expression for the likelihood function does not distinguish between the critical ROI and the rest of the ROIs. This formalism also does not include censored ROIs in a formal way. The reason is that the set of ROIs, including the critical ROI, is considered one set of samples from the population of such sets with the given set of ROIs for that specimen. The extreme value formulation automatically includes all of the ROIs in the determination of the probabilities for that specimen. The critical ROI then is not anything special. All that is needed to know is that all of the ROIs (including the critical ROI) had a K_{fc} value that was less than the K_{fc} value found for this specimen.

To test this proposed approach, the model was calibrated on a subset of AF1410 Batch A C-F test specimens (14, 20, 36, 58, 59, 62, 21, 29, 12, 37, and 41). The model parameters were found to be as follows: $\alpha = 0.547$ mm and $\sigma = 0.566$ (unitless) for the Peterson Notch Sensitivity model,

$$\ln(K_{fc} - 1) = \ln(K_t - 1) + \varepsilon \quad (30)$$

where ε has zero mean and standard deviation of σ .

MICROMACHINED SPECIMEN LIFE PREDICTION

As part of the C-F program investigations, AF1410 flat steel plates with discrete micromachined notch features were proposed to study the ability of traditional notched fatigue analysis approaches to predict fatigue life reduction due to known geometric shapes. Details of the specimen design and fabrication are discussed in the second program contract report [22]. Fatigue testing was performed using the same constant-amplitude marker cycle fatigue load history that was used for the AF1410 Batch A and Batch B C-F tests. Three types of geometric features were utilized for these specimens: conic frustum, ellipsoidal, and pill-shaped. The shape and dimensions of each one are shown in figures 15, 16, and 17. The orientation of each feature on the gage section of the plate is shown in figure 18. The feature dimensions were sized to give a maximum K_t of 2.5, based on elastic FEA. The conic frustum was intended to be a cone with a single radius at the tip. Tooling limitations necessitated the use of multiple radii, resulting in the current frustum shape.

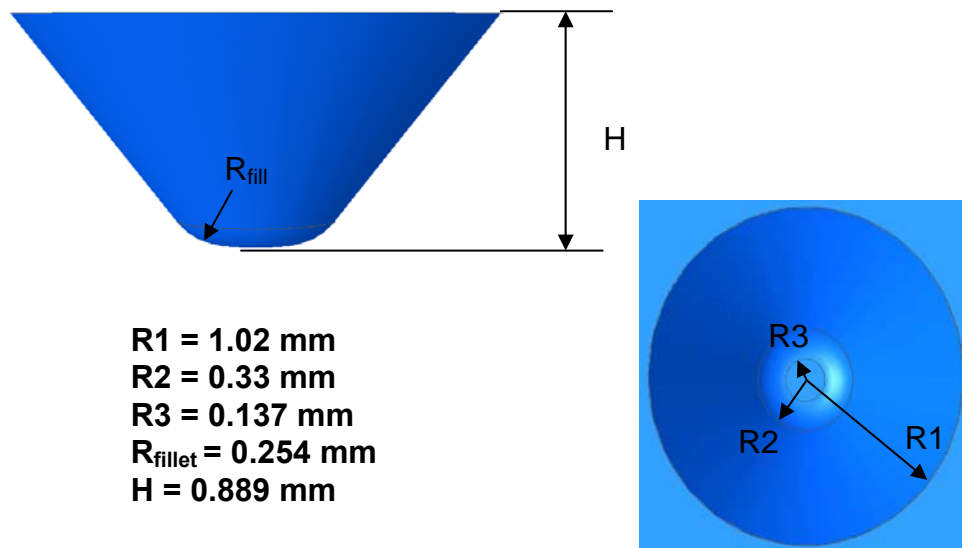


Figure 15: Conic Frustum Feature Dimensions

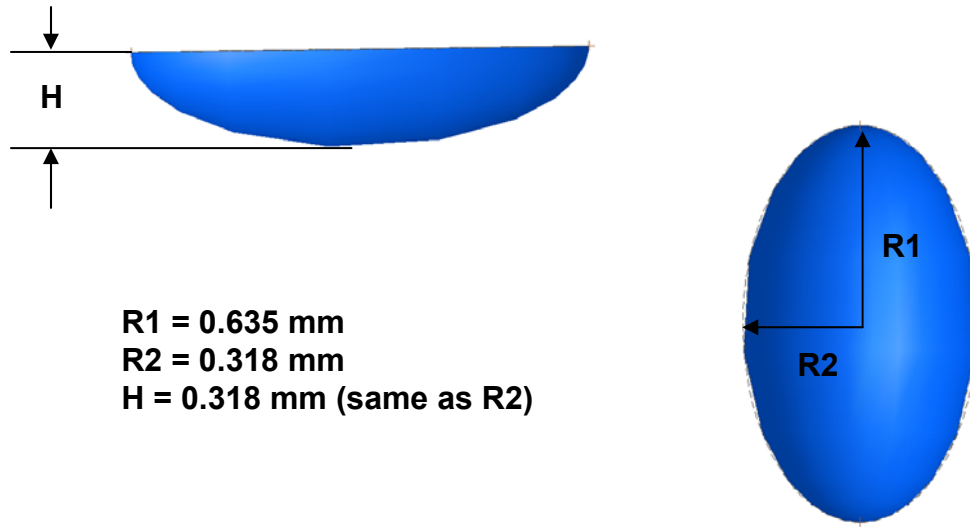


Figure 16: Ellipsoidal Feature Dimensions

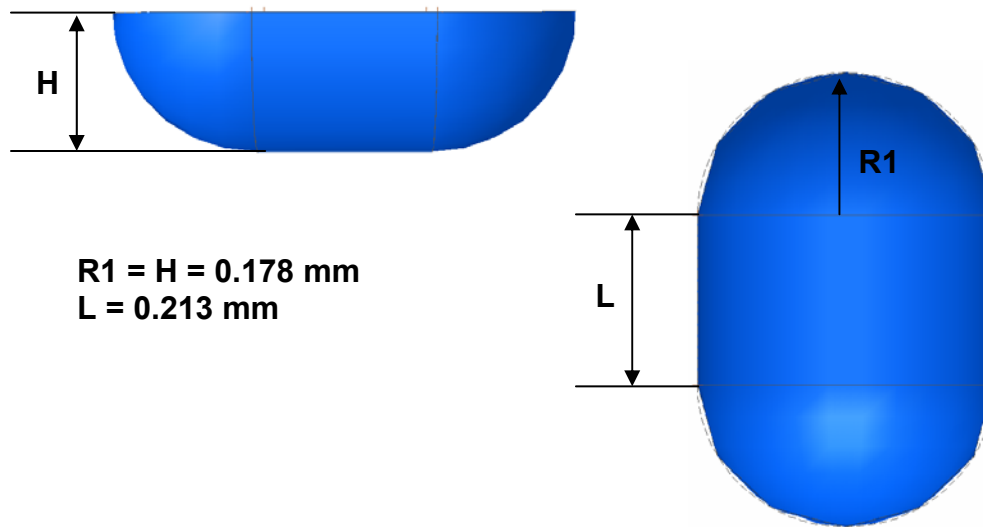


Figure 17: Pill-Shape Feature Dimensions

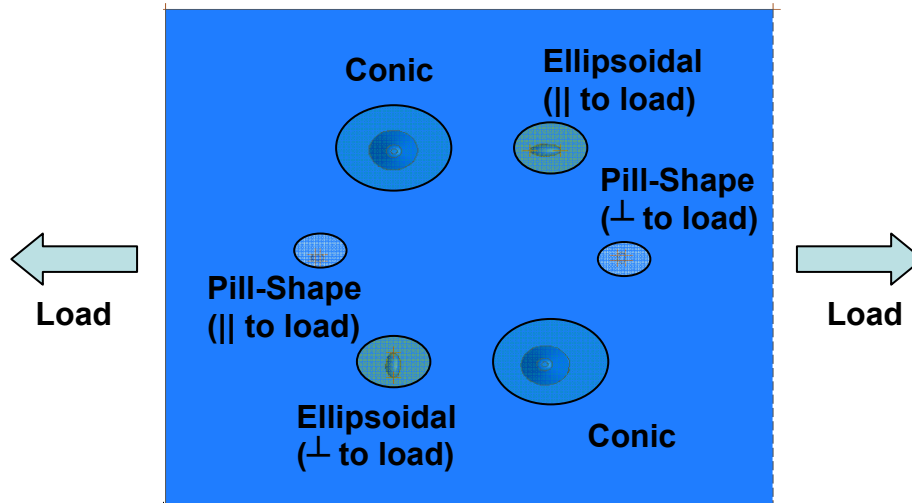


Figure 18: Feature Orientation on Micromachined Plate Surface

The original intent of the micromachined specimen test regime was to generate replicate test samples with geometric notch features similar to the critical notches on corroded test specimens. However, machine tool limitations required the specification of notch features with characteristic dimensions much larger than the critical corrosion notches on the Batch A and Batch B test specimens. This meant that the micromachined features fell outside the experimental bounds of the notch sensitivity model calibration for the C-F test data. It was then thought that the micromachined specimens could provide a validation of the notched fatigue analysis approach to characterizing small geometric features that would be independent of the sampling difficulties inherent in C-F testing. Although the notch geometries would be larger than the experimental database of corrosion damage, the small surface notches on a flat surface of uniform stress provide a stress distribution field more representative of corrosion damage than is the case for the circumferentially notched axial and rotating bending specimens traditionally used to develop notch sensitivity equations.

Predictions of the test life to crack initiation (0.010 in. deep crack) for the micromachined specimens were made using two different versions of the ESR C-F model that were calibrated to predict the life of geometrically-notched specimens. The Peterson notch sensitivity equation is used for all test predictions here.

$$q = \frac{1}{1 + \alpha/r} \quad (31)$$

For the first prediction, the value of α in Peterson's equation is taken to be the average value that Peterson gives for quenched and tempered steels ($\alpha = 0.064$ mm) [23]. Since there was no large body of test data used to generate Peterson's α value, the range of scatter in the values of q for this fit is unknown. Hence, the first life prediction only assigns a deterministic value of q to each

micromachined notch, and the parameter uncertainty and subsequent confidence bounds of the life prediction are unknown.

For the second prediction model, geometrically-notched fatigue test results for various high-strength steels were taken from the Aerospace Structural Metals Handbook [24]. This data set groups together test results from 10 different materials, some with varying tensile strengths, for both axial and rotating bending type tests. Data for quenched and tempered material is shown in table 3, and some data for material in the normalized and annealed condition shown in table 4. The notch ratios were determined from finite element models based on the specimen geometry information provided in the reference.

Table 3: Notched Fatigue Results for Quenched and Tempered High-Strength Steels

| Material | Ultimate Strength (ksi) | Notch Radius (in.) | Notch Radius (mm) | Unnotched Endurance Limit (ksi) | Notched Endurance Limit (ksi) | K_t | K_f | q |
|---------------------------|-------------------------|--------------------|-------------------|---------------------------------|-------------------------------|-------|-------|-------|
| 4130 Sheet | 180 | 0.3175 | 8.0645 | 60 | 40 | 2 | 1.5 | 0.50 |
| | 180 | 0.057 | 1.4478 | 60 | 18 | 4 | 3.33 | 0.778 |
| 4340 Bar | 125 | 0.01 | 0.254 | 50 | 19 | 3.66 | 2.63 | 0.613 |
| | 150 | 0.01 | 0.254 | 70 | 30 | 3.66 | 2.33 | 0.501 |
| | 200 | 0.01 | 0.254 | 70 | 22 | 3.66 | 3.18 | 0.820 |
| | 260 | 0.03 | 0.762 | 78 | 52 | 2.19 | 1.50 | 0.420 |
| | 260 | 0.01 | 0.254 | 78 | 45 | 3.22 | 1.73 | 0.330 |
| 4140 Bar | 110 | 0.015 | 0.381 | 60 | 28 | 2.39 | 2.14 | 0.848 |
| | 110 | 0.015 | 0.381 | 53 | 26 | 2.39 | 2.04 | 0.770 |
| | 140 | 0.025 | 0.635 | 72 | 40 | 2.11 | 1.80 | 0.723 |
| | 237 | 0.025 | 0.635 | 103 | 62 | 1.94 | 1.66 | 0.704 |
| 8630 Cast Bar | 138 | 0.015 | 0.381 | 65 | 38 | 2.35 | 1.71 | 0.527 |
| D6AC Bar | 285 | 0.008 | 0.2032 | 100 | 50 | 3.31 | 2.00 | 0.433 |
| 300M Forging | 280 | 0.04 | 1.016 | 100 | 58 | 2.11 | 1.72 | 0.654 |
| | 280 | 0.0145 | 0.3683 | 100 | 30 | 3.28 | 3.33 | 1.022 |
| | 280 | 0.0042 | 0.10668 | 100 | 20 | 5.85 | 5.00 | 0.825 |
| HY-TUF Billet | 240 | 0.012 | 0.3048 | 70 | 30 | 3.13 | 2.33 | 0.627 |
| Nitralloy 135 Mod. Billet | 140 | 0.005 | 0.127 | 45 | 24 | 3.53 | 1.88 | 0.345 |
| H11 Mod. | 290 | 0.008 | 0.2032 | 95 | 50 | 3.31 | 1.90 | 0.390 |
| 18 Ni (250) Maraging | 261 | 0.0055 | 0.1397 | 100 | 45 | 3.18 | 2.22 | 0.560 |
| | 288 | 0.0055 | 0.1397 | 103 | 63 | 3.18 | 1.63 | 0.291 |
| | 264 | 0.0055 | 0.1397 | 103 | 54 | 3.18 | 1.91 | 0.416 |
| | 281 | 0.0055 | 0.1397 | 108 | 45 | 3.18 | 2.4 | 0.641 |

Table 4: Notched Fatigue Results for Some Normalized and Annealed High-Strength Steels

| Material | Ultimate Strength (ksi) | Notch Radius (in.) | Notch Radius (mm) | Unnotched Endurance Limit (ksi) | Notched Endurance Limit (ksi) | K_t | K_f | Q |
|----------------------|-------------------------|--------------------|-------------------|---------------------------------|-------------------------------|-------|-------|-------|
| 4130 Sheet | 123 | 0.76 | 19.304 | 47 | 35 | 1.5 | 1.34 | 0.686 |
| | 120 | 0.3175 | 8.0645 | 47 | 26 | 2 | 1.81 | 0.808 |
| | 120 | 1.5 | 38.1 | 47 | 26 | 2 | 1.81 | 0.808 |
| | 120 | 0.1736 | 4.40944 | 47 | 26 | 2 | 1.81 | 0.808 |
| | 120 | 0.057 | 1.4478 | 47 | 14 | 4 | 3.36 | 0.786 |
| | 120 | 0.07 | 1.778 | 47 | 14 | 4 | 3.36 | 0.786 |
| | 120 | 0.0195 | 0.4953 | 47 | 14 | 4 | 3.36 | 0.786 |
| | 120 | 0.075 | 1.905 | 47 | 14 | 5 | 3.36 | 0.589 |
| 8630 Cast Bar | 110 | 0.015 | 0.381 | 54 | 33 | 2.348 | 1.64 | 0.472 |
| 18 Ni (250) Maraging | 270 | 0.01 | 0.254 | 116 | 55 | 2.2 | 2.11 | 0.924 |
| | 250 | 0.01 | 0.254 | 115 | 55 | 2.2 | 2.09 | 0.909 |

The notch sensitivity data were plotted as a function of the notch root radius to enable fitting of the Peterson model (figure 19). Also plotted were curves defined by the coefficient values for quenched and tempered and normalized and annealed steels taken from Peterson (reference 23). The normalized and annealed value was ($\alpha = 0.254$ mm). The plot shows a large amount of scatter in both sets of test data, with the Peterson curve for quenched and tempered steels being conservative for nearly all data points. The Peterson curve for normalized and annealed data is less conservative for the quenched and tempered data, but is still conservative for most of the available normalized and annealed data. A least-squares fit of the Peterson equation to the quenched and tempered data gives a coefficient ($\alpha = 0.174$ mm) that is between the Peterson defined values for the two material condition categories, but the R^2 value for this fit is only 20% due to the large amount of scatter in the data. The 300M forging data point with the notch sensitivity value greater than 1.0 was reset to 0.99 for the equation fit, and the 4130 sheet data point with the 8 mm notch radius was removed from the data set for fitting.

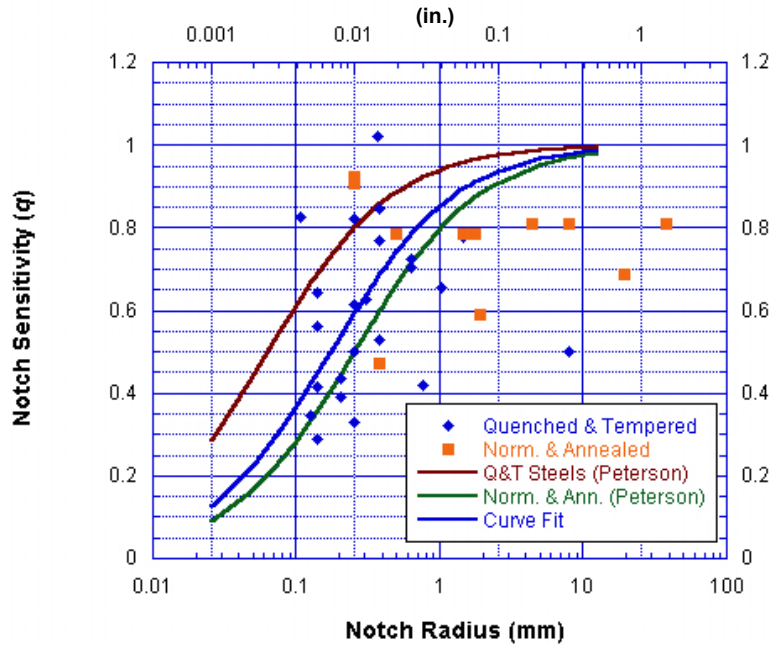


Figure 19: Notch Sensitivity Data and Peterson Curves for High-Strength Steels

Unlike the notch factor values from the C-F data set, the values from tables 3 and 4 are determined for unnotched and notched endurance limit data that nominally represents the average behavior of a set of identical fatigue test specimens. As such, the notch factor values can be considered point estimates of the true value, with fatigue scatter effects eliminated. As stated in a previous section, when fatigue scatter effects are factored out of the q equation inputs, the value of q ranges from zero for no notch effect ($K_f = 1$) to unity for a full notch effect ($K_f = K_t$). The finite upper and lower bounds of possible q values can be accounted for in the error distribution (ε) about the regression curve (equation 6) by assuming a series of Beta distributions for the error.

$$\begin{aligned} \varepsilon &\sim \text{Beta}(a, b) \\ 0 &< \varepsilon < 1 \end{aligned} \quad (32)$$

The Peterson notch sensitivity equation is still used to represent the mean fit of the notch data. The expected value of q from the Peterson equation is also the expected value of the Beta distribution for a specified notch radius.

$$E[q | R] = 1/(1 + \alpha/R) = E[\varepsilon | R] = a/(a + b) = \mu_q \quad (33)$$

A variance structure for the Beta error distribution is assumed that follows the shape of a symmetric Beta PDF, with zero variance at the asymptotic limits of q , and maximum variance ($\sigma_{0.5}^2$) at $q = 0.5$.

$$\text{Var}[\varepsilon | \mu_q] = \sigma_q^2(\mu_q | \sigma_{0.5}^2, \lambda) = \sigma_{0.5}^2 (4\mu_q)^{\lambda-1} (1 - \mu_q)^{\lambda-1} \tag{34}$$

$$\text{Var}[\varepsilon | \mu_q] = \frac{ab}{(a+b)^2(a+b+1)} \tag{35}$$

Maximum likelihood estimators were derived for the model parameters α , $\sigma_{0.5}$ and λ from equations 33, 34, and 35. The Beta MLE was calculated only for the quenched and tempered fatigue data, with the parameter value estimates shown in table 5. The MLE value of the notch sensitivity coefficient (α) closely matches the least-squares fit value, as expected. The resulting MLE mean fit of the data is shown in figure 20, along with the three standard deviation upper and lower prediction bounds. The plot shows that the data fall within the 3 sigma prediction bounds for the model fit.

Table 5: MLE Parameter Estimates for Beta Distributed Peterson Notch Sensitivity Equation

| Material | Sample Size | $\hat{\alpha}$ (mm) | $\hat{\sigma}_{0.5}$ | $\hat{\lambda}$ |
|---------------------------|-------------|---------------------|----------------------|-----------------|
| Quenched and Tempered HSS | 22 | 0.177 | 0.207 | 2.035 |

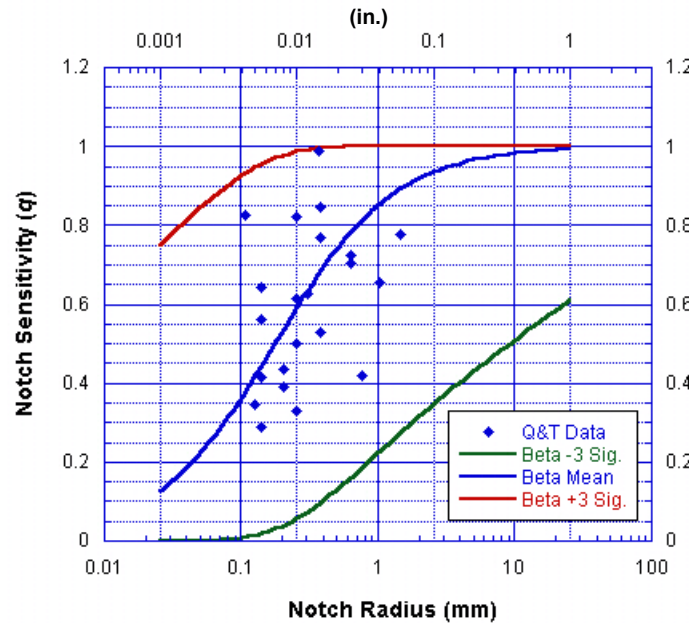


Figure 20: Peterson Beta Model Fit to Quenched and Tempered HSS Data

Micromachined specimen life predictions were performed using the ESR methodology developed previously for corroded specimens, with some modifications. Since the micromachined notch geometries are exactly defined, an ROI analysis with elasticity modeling was not necessary. The notch metric equation was used to define a K_t and equivalent notch radius for each micromachine feature using the nominal width height and depth dimensions, with the results listed in table 6 and compared to finite element K_t values.

Table 6: Micromachined Notch Metric Dimensions and Parameters

| Notch Type | Width (mm) | Height (mm) | Depth (mm) | Notch Radius (mm) | Notch Metric K_t | FEM K_t |
|---------------|------------|-------------|------------|-------------------|--------------------|-----------|
| Conic Frustum | 2.03 | 2.03 | 0.889 | 1.025 | 2.041 | 2.53 |
| Ellipsoid 1 | 1.27 | 0.635 | 0.318 | 0.318 | 2.521 | 2.50 |
| Ellipsoid 2 | 0.635 | 1.27 | 0.318 | 0.794 | 1.544 | 1.47 |
| Pill 1 | 0.569 | 0.356 | 0.178 | 0.178 | 2.395 | 2.52 |
| Pill 2 | 0.356 | 0.569 | 0.178 | 0.317 | 1.685 | 1.75 |

The equivalent notch radius values of the micromachined features fall within the radius bounds of the quenched and tempered data set, indicating that the Peterson Beta model fit should be representative of these notch types. Mean notch sensitivity and K_f values for the Peterson Beta model were calculated using the parameter estimates in table 5, with the results shown in table 7 for the Beta model and the original Peterson model coefficient for quenched and tempered steels.

Table 7: Notch Sensitivity and Notch Factors for Micromachined Features

| Notch Type | q - Peterson | q - Peterson (data) | K_f - Peterson | K_f - Peterson (data) |
|-------------|----------------|-----------------------|------------------|-------------------------|
| Conical | 0.941 | 0.853 | 1.980 | 1.888 |
| Ellipsoid 1 | 0.832 | 0.642 | 2.266 | 1.977 |
| Ellipsoid 2 | 0.925 | 0.818 | 1.503 | 1.445 |
| Pill 1 | 0.736 | 0.501 | 2.026 | 1.700 |
| Pill 2 | 0.832 | 0.641 | 1.570 | 1.439 |

ESR life predictions were made using each discrete notch factor for the original Peterson model. For the Peterson Beta model, two sets of life predictions were performed. In the first, the discrete micromachined notch factors from the Beta model fit were input to the ESR code and run in the same manner as the original Peterson fit prediction and the C-F specimen predictions. In the second, a Monte Carlo ESR simulation was used to propagate the scatter in q for a given notch root radius through to the life distribution for each micromachine notch. Two constant-amplitude ($R = 0.1$) strain life curves at 0.001 and 0.50 probability were generated and used to fit a lognormal life distribution at each Monte Carlo K_f value. A random sample was then drawn from each lognormal distribution and then ranked to generate the CDF of crack initiation for each notch. Confidence bounds on the sample size effect of the Monte Carlo prediction were generated using a modified form the normal CDF discretization error equation of Shooman [25].

$$N = \left(\frac{1 - P_f}{P_f} \right) \left(\frac{200}{\gamma} \right)^2 \quad (36)$$

The target failure probability for validation is 50%, so to achieve a 5% error in the predicted life with 95% confidence, the Monte Carlo sample size must be at least 1600.

CADMIUM-PLATED CORROSION-FATIGUE SPECIMEN LIFE PREDICTION

ESR life predictions on cadmium-plated C-F specimens were made using the same methods described previously for the Batch A and Batch B C-F specimens. WLI scans with 7.66 μm lateral resolution were acquired before each plate was tested. Tests on corroded and uncorroded specimens were performed using the constant-amplitude marker band load history used previously on other C-F and micromachined specimens. Peak stress was 170 ksi. Since these specimens were grit-blasted prior to plating, the Batch A ROI threshold of 1.3 K_t on 36 square pixel area was applied. The Batch A fit to the log-Peterson Notch Sensitivity Equation was also used.

EQUIVALENT STRESS RISER MODELING OF STRESS GRADIENT EFFECTS

The ESR model outlined in the previous sections was developed from test results on flat C-F test specimens with roughly constant net section stress contours in the gage section. To be usefully applied to actual airframe components, the ESR modeling capability must be extended from the uniform stress state case to more complex stress states. Most airframe components are subject to combined axial, bending, shear, and torsional loads of varying magnitude, orientation, and phasing. These loads can produce complex surface stress gradients that vary from one load sequence to the next. The first simplifying assumption made in accounting for stress gradient effects is to limit the applied loading to those cases where the resulting stresses in the corroded region have fixed principle axes orientations, which is commonly referred to as proportional loading. Cases in which the stress principle axes orientations vary throughout the load history are referred to as nonproportional loading, and require multiaxial fatigue analysis methods that are outside the scope of the current research effort. The second simplifying assumption is that the maximum stress anywhere on the corroded surface remains elastic, prior to accounting for corrosion damage. This assumption is necessary to enable the superposition of stresses and strains to account for various combinations of load cases and sequences. No net section yielding is allowed at any time during the loading history.

The ESR model as applied to a uniform stress field assumes that the stress concentration in a corrosion notch is only a function of the notch geometry. In a nonuniform stress field, the notch stress concentration is a function of both the notch geometry and its location in the stress field. For a component load history that contains multiple load cases producing different stress gradients in time, the complete spectrum load history will produce a different stress history at every point on the component surface. This makes calculating life distributions from individual notch location stress histories too computationally intensive to be applied to surfaces with even moderate numbers of corrosion notches. Therefore, histograms of K_{fc} values must be utilized to generate life predictions on corroded surfaces with stress gradients.

For a component with a nonuniform stress field in the corroded region, the CDF of the survivability in the presence of the j^{th} single corrosion notch can be defined as:

$$R_j(N_i) = R_j(N_i | K_{fc-j}, \sigma(t | x_j, \theta_l)) \quad (37)$$

where the independent variable N_i is the number of cycles to crack initiation, the CDF is conditional on the values of K_{fc-j} and the local stress history σ . The local stress history is conditional on the notch location x in the stress field and the stress gradient θ for l different load cases, and varies as a function of the independent variable time t . For most airframe components, FEM analyses can be used to generate contour maps of surface stresses in corroded regions, for all unique load cases. By choosing a reference location at any point on a contour map, a stress concentration factor for gradient effects (K_g) can be defined as the ratio of the reference point stress to the local stress at a particular point. The stress contour maps for each load case are then transformed into K_g maps based on a common reference location.

$$K_{g-j,l} = \frac{\sigma(x_{ref}, \theta_l)}{\sigma(x_j, \theta_l)} \quad (38)$$

Local stress histories for any location on the contour maps can be built up from the K_g maps for each load case, and the spectrum stress history at the reference location.

$$\sigma_j(t) = \sum_{i=1}^l K_{g-j,i} \sigma_{ref}(t | \theta_i) \quad (39)$$

This local stress history can be directly used to estimate the survivability CDF for an individual notch, but a large number of spectrum strain-life calculations would be necessary for each notch. An approximate method that greatly reduces the number of strain-life calculations would be to define an equivalent gradient stress concentration factor ($K_{g-equiv}$) that also accounts for the difference in crack initiation life between a notch at a local point and the same notch at the reference location. To do this, a median spectrum strain-life curve is generated for a range of reference stress ratios at the reference location, and for a reference notch K_{fc} value. A median strain-life prediction is then generated at each local notch location using the respective local stress histories, but for the reference notch K_{fc} value. Using the local notch predicted life, a local reference stress ratio can be interpolated from the spectrum strain-life curve at the reference location. This stress ratio defines the $K_{g-equiv}$ value for the local notch that, when applied to the reference location stress history, will give the median life value for the local notch.

$$R_j(N_i | K_{fc-ref}, \sigma_j(t)) = R_j(N_i | K_{fc-ref}, K_{g-equiv_j} \sigma_{ref}(t)) = 0.50 \quad (40)$$

An effective C-F notch factor (K_{fc-eff}) can now be defined for the reference location that is the product of the local $K_{g-equiv}$ and K_{fc} values, and that when applied to the reference location stress history, will give the median life value of the local notch for its actual K_{fc} value.

$$K_{fc-eff-j} = K_{g-equiv-j} K_{fc-j} \quad (41)$$

This approximation effectively decouples the local notch life prediction from the local stress history, allowing all subsequent notch life predictions to be made using only the stress history at the reference location. Only one local notch life prediction using the local stress history must be made for each notch. The decoupling allows all of the notches to be grouped into a histogram of K_{fc-eff} values for component life prediction, using m histogram bins:

$$R(N_i) \approx \prod_{k=1}^m [R_k(N_i | K_{fc-eff-k}, \sigma_{ref}(t))]^{h_k} \quad (42)$$

where h is the number of occurrences in each histogram bin. The K_{f-eff} values for the uncorroded surface area portions can be estimated similarly to the K_{fc-eff} values for the corrosion notches. The entire surface of the part is divided into a grid, and local stresses are averaged across each grid square for each load case. A $K_{g-equiv}$ value is calculated for each grid square using the approach described previously, but for a reference K_f value of 1.0, since no notch is present. The K_{f-eff} values for each grid square are then just the $K_{g-equiv}$ values, since all of the nominal K_f values for the grid squares are 1.0. The K_{f-eff} values can be grouped into a separate histogram or added to the K_{fc-eff} histogram, with the exponent values for each bin being the product of the number of grid squares in the bin and the ratio of a single grid square area to the strain-life coupon gage area.

CORROSION SURFACE-ROUGHNESS BASED MODELING

The ESR approach to C-F modeling described previously relies on high-resolution 3D surface topography information to capture the corrosion notch features that cause fatigue cracking. However, currently deployed fleet NDI techniques such as ultrasonic and eddy-current do not have the spatial and depth resolution necessary to capture the surface detail required for use of the ESR modeling approach in component fatigue life prediction. Alternative approaches were explored that seek to categorize the corrosion severity in terms of surface roughness metrics, and that may be suitable for use with existing NDI techniques. Forty different surface height roughness metrics were investigated to look for correlations to fatigue life for corrosion damage. Of those, average surface roughness (R_a), root-mean-square surface roughness (R_q) and normalized volume loss showed the best correlation compared to the other metrics. Roughness metric comparisons used available WLI scans of test specimen corrosion patches, with a single metric value calculated based on the entire scan area of the corrosion patch. It was realized that this averaging over a large area has the effect of smoothing out local areas of significant roughness that may be more susceptible to cracking, so a grid-based approach was implemented where the entire scanned image is broken up into a rectangular grid of 0.5 – 1.0 mm lateral resolution. Roughness values were then calculated for each grid square from the image data. The results are shown for two different Batch A specimens in figures 21 and 22.

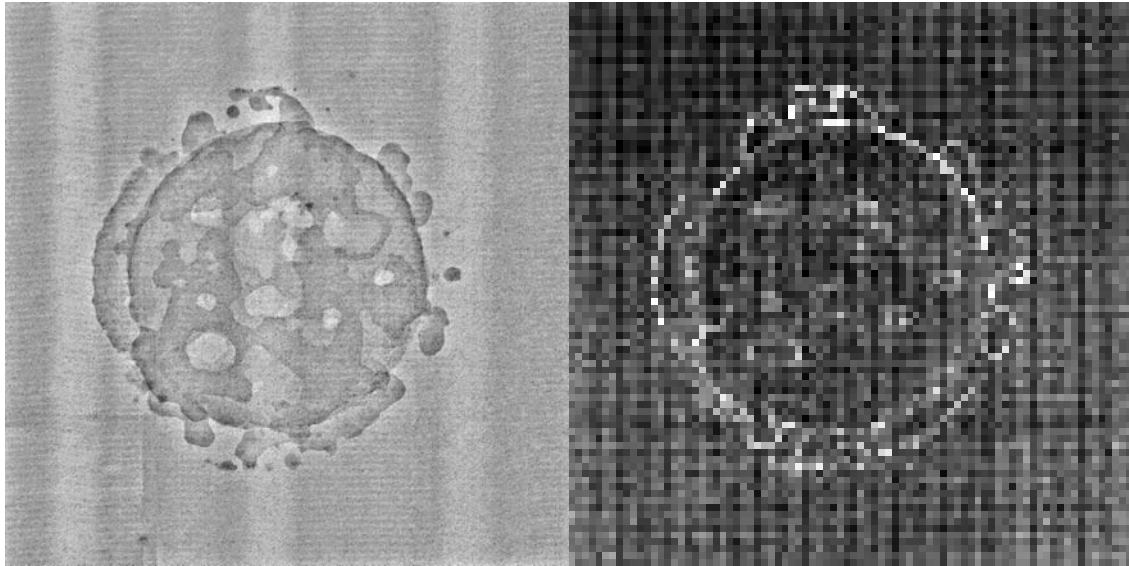


Figure 21: Metric Grid Results for Batch A Specimen 62, 3-hr Exposure, WLI Image (Left) and R_a Image (Right)

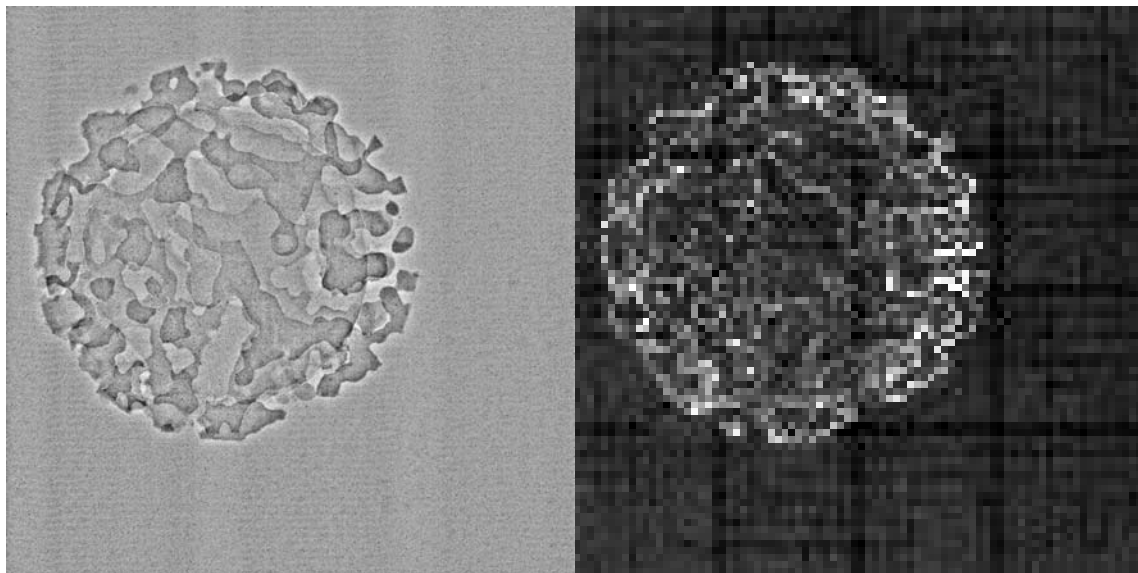


Figure 22: Metric Grid Results for Batch A Specimen 59, 6-hr Exposure, WLI Image (Left) and R_a Image (Right)

The WLI image resolution for specimen 62 was $6.345 \mu\text{m}$, and was $7.66 \mu\text{m}$ for specimen 59. The R_a images for both specimens are for a grid spacing of $500 \mu\text{m}$. Examination of several metric grid images indicated that the metric grid approach was capturing the large-scale surface variations in the corroded specimens, but not the small-scale surface variations indicative of corrosion notches. However, there appeared to be a correlation between the areas where fatigue

cracks occurred in the tests and the large-scale surface variations in the corrosion patch. To examine this correlation, R_a and R_q values for the grid blocks that correspond to the locations of corrosion notch critical cracks on Batch A specimens were compared to the maximum grid metric values for the entire image, as well as the average metric value for the entire image. The results are listed in tables 8, 9, and 10, and show that the critical crack grid values are near or above the upper 90th percentile of all grid values in most cases. The effect of increasing the grid spacing is also shown.

Table 8: Metric Grid Results for WLI Image, Batch A Specimens, 3-hr Exposure

| Specimen | Plate | | Critical Crack Location | | Max. | | Critical Location % | |
|-------------------|-------|-------|-------------------------|-------|--------|--------|---------------------|-------|
| | R_a | R_q | R_a | R_q | R_a | R_q | R_a | R_q |
| Spec. 15 | 3.127 | 4.21 | | | | | | |
| 1000 μm Res. | | | 3.952 | 5.346 | 6.421 | 7.547 | 94.7 | 96.3 |
| 500 μm Res. | | | 3.093 | 4.194 | 9.184 | 10.628 | 73.7 | 74.7 |
| Spec. 21 | 2.919 | 4.426 | | | | | | |
| 1000 μm Res. | | | 2.883 | 4.16 | 5.043 | 6.595 | 51.3 | 34.7 |
| 500 μm Res. | | | 2.525 | 3.97 | 6.183 | 8.928 | 90.2 | 86.6 |
| Spec. 29 | 2.972 | 3.992 | | | | | | |
| 1000 μm Res. | | | 3.267 | 4.243 | 5.591 | 9.32 | 89.4 | 87 |
| 500 μm Res. | | | 3.204 | 4.192 | 6.659 | 13.03 | 90.2 | 86.6 |
| Spec. 36 | 2.739 | 3.976 | | | | | | |
| 1000 μm Res. | | | 4.335 | 5.446 | 5.734 | 7.072 | 99.3 | 98.6 |
| 500 μm Res. | | | 3.559 | 4.781 | 6.022 | 9.532 | 96.7 | 93.0 |
| Spec. 62 | 3.128 | 4.200 | | | | | | |
| 1000 μm Res. | | | 3.753 | 4.775 | 5.1882 | 6.345 | 96.4 | 95.1 |
| 500 μm Res. | | | 3.456 | 4.467 | 5.789 | 7.579 | 92.5 | 86.0 |

Table 9: Metric Grid Results for WLI Image, Batch A Specimens, 6-hr Exposure

| Specimen | Plate | | Critical Crack Location | | Max. | | Critical Location % | |
|-------------------|-------|-------|-------------------------|-------|-------|--------|---------------------|-------|
| | R_a | R_q | R_a | R_q | R_a | R_q | R_a | R_q |
| Spec. 5 | 3.158 | 4.16 | | | | | | |
| 1000 μm Res. | | | 3.982 | 5.184 | 6.681 | 8.052 | 90.7 | 91.5 |
| 500 μm Res. | | | 3.812 | 4.866 | 7.486 | 8.631 | 92.3 | 92.3 |
| Spec. 6 | 3.55 | 4.7 | | | | | | |
| 1000 μm Res. | | | 3.937 | 5.031 | 9.352 | 10.975 | 83.1 | 82.2 |
| 500 μm Res. | | | 4.078 | 5.276 | 9.648 | 13.445 | 89.8 | 90.0 |
| Spec. 12 | 3.786 | 4.96 | | | | | | |
| 1000 μm Res. | | | 6.196 | 8.001 | 7.895 | 9.256 | 99.2 | 99.6 |
| 500 μm Res. | | | 3.621 | 4.729 | 8.741 | 9.915 | 64.5 | 64.3 |
| Spec. 14 | 3.234 | 4.634 | | | | | | |

| | | | | | | | | |
|-------------------------|-------|-------|-------|--------|--------|--------|------|-------|
| 1000 μm Res. | | | 6.853 | 8.34 | 7.629 | 8.739 | 99.9 | 99.9 |
| 500 μm Res. | | | 8.861 | 10.435 | 8.861 | 10.435 | 100 | 100 |
| Spec. 20 | 3.291 | 4.394 | | | | | | |
| 1000 μm Res. | | | 5.433 | 7.632 | 8.593 | 10.004 | 96.2 | 99.0 |
| 500 μm Res. | | | 9.44 | 10.784 | 10.472 | 11.432 | 99.9 | 99.96 |
| Spec. 37 | 3.478 | 4.716 | | | | | | |
| 1000 μm Res. | | | 4.395 | 5.756 | 6.735 | 8.156 | 90.8 | 91.6 |
| 500 μm Res. | | | 5.681 | 7.493 | 8.625 | 10.349 | 98.4 | 99.0 |
| Spec. 41 | 3.456 | 4.575 | | | | | | |
| 1000 μm Res. | | | 5.179 | 6.648 | 7.814 | 9.272 | 96.0 | 96.9 |
| 500 μm Res. | | | 5.707 | 7.445 | 9.486 | 10.641 | 98.2 | 98.8 |
| Spec. 42 | 3.34 | 4.513 | | | | | | |
| 1000 μm Res. | | | 3.921 | 5.256 | 8.057 | 9.248 | 81.6 | 84.0 |
| 500 μm Res. | | | 4.279 | 6.174 | 10.031 | 11.266 | 91.6 | 95.0 |
| Spec. 58 | 3.506 | 4.647 | | | | | | |
| 1000 μm Res. | | | 4.505 | 5.92 | 7.631 | 9.479 | 91.4 | 93.2 |
| 500 μm Res. | | | 4.548 | 6.041 | 8.889 | 11.411 | 94.5 | 95.7 |
| Spec. 59 | 3.263 | 4.363 | | | | | | |
| 1000 μm Res. | | | 4.612 | 5.784 | 8.682 | 10.104 | 91.8 | 91.5 |
| 500 μm Res. | | | 3.671 | 4.829 | 9.9 | 11.149 | 87.8 | 88.4 |

Table 10: Metric Grid Results for WLI Image, Selected Batch A Specimens, 12-hr Exposure

| Specimen | Plate | | Critical Crack Location | | Max. | | Critical Location % | |
|-------------------------|----------------|----------------|-------------------------|----------------|----------------|----------------|---------------------|----------------|
| | R _a | R _q | R _a | R _q | R _a | R _q | R _a | R _q |
| Spec. 35 | 5.027 | 6.951 | | | | | | |
| 1000 μm Res. | | | 9.726 | 13.318 | 14.281 | 16.867 | 97.9 | 99.2 |
| 500 μm Res. | | | 7.86 | 11.609 | 17.539 | 19.077 | 96.7 | 98.5 |
| Spec. 38 | 5.229 | 7.427 | | | | | | |
| 1000 μm Res. | | | 14.084 | 18.678 | 16.927 | 18.894 | 99.8 | 99.9 |
| 500 μm Res. | | | 13.723 | 18.084 | 20.925 | 26.526 | 99.8 | 99.9 |
| Spec. 46 | 5.298 | 7.313 | | | | | | |
| 1000 μm Res. | | | 10.642 | 13.862 | 13.104 | 16.039 | 99.0 | 99.5 |
| 500 μm Res. | | | 6.721 | 10.659 | 16.521 | 19.909 | 93.1 | 97.2 |

The critical crack grid block values for the Batch B specimens are listed in tables 11, 12, and 13 for 1000 μm grid spacing only, and exceed the upper 90th percentile of all grid values in the majority of cases, except for the 1.5-hr exposures. The critical crack grid block values can also be plotted as a function of the plate median K_{fc} values, as shown in figures 23 and 24 for critical R_q value. Plots for plate test K_{fc} versus critical R_a value are similar.

Table 11: Metric Grid Results for WLI Image, Batch B Specimens, 1.5-hr Exposure, 1000 μm Resolution

| Specimen | Critical Crack Location | | Max. | | Critical Location % | |
|----------|-------------------------|--------|--------|--------|---------------------|-------|
| | R_a | R_q | R_a | R_q | R_a | R_q |
| 544-9C | 0.7596 | 1.1317 | 2.475 | 2.757 | 81.9 | 86.0 |
| 545-3D | 0.7083 | 0.8898 | 2.451 | 2.652 | 82.7 | 82.7 |
| 547-26A | 1.1363 | 1.4454 | 2.3425 | 2.7214 | 93.8 | 94.7 |
| 545-2A | 1.0809 | 1.3613 | 2.9291 | 3.2363 | 92.1 | 92.3 |
| 547-50B | 0.6036 | 0.729 | 2.3565 | 2.807 | 77.0 | 76.0 |
| 614-7 | 0.777 | 0.9912 | 2.336 | 2.676 | 83.6 | 84.4 |
| 614-11 | 2.615 | 3.104 | 2.615 | 3.104 | 100.0 | 100.0 |

Table 12: Metric Grid Results for WLI Image, Batch B Specimens, 3-hr Exposure, 1000 μm Resolution

| Specimen | Critical Crack Location | | Max. | | Critical Location % | |
|----------|-------------------------|--------|--------|--------|---------------------|-------|
| | R_a | R_q | R_a | R_q | R_a | R_q |
| 545-6A | 2.6023 | 3.1209 | 3.8607 | 4.3702 | 97.5 | 97.8 |
| 545-10D | 2.4693 | 2.9693 | 4.1044 | 4.7087 | 97.1 | 97.3 |
| 547-22C | 2.0445 | 2.5128 | 4.9589 | 5.638 | 88.6 | 88.5 |
| 547-37B | 1.1277 | 1.4415 | 3.6911 | 4.3506 | 72.9 | 73.2 |
| 547-9M | 2.003 | 2.3508 | 4.7804 | 5.2958 | 93.0 | 91.9 |
| 547-5A | 1.6863 | 2.3408 | 4.238 | 4.825 | 89.0 | 92.1 |
| 547-23B | 3.1676 | 3.892 | 4.7697 | 5.5815 | 98.3 | 98.6 |
| 544-5C | 2.100 | 2.7601 | 3.7924 | 4.3123 | 96.3 | 97.7 |
| 614-4 | 0.914 | 1.3364 | 3.9442 | 4.7583 | 69.1 | 71.9 |
| 614-12 | 1.167 | 1.6192 | 4.1603 | 5.5801 | 75.1 | 77.2 |
| 614-21 | 4.2024 | 4.7469 | 5.4091 | 6.2483 | 99.6 | 99.6 |
| 614-1 | 1.9684 | 2.4015 | 4.358 | 4.882 | 91.9 | 91.9 |
| 614-15 | 1.912 | 2.297 | 3.4067 | 3.9665 | 95.2 | 94.7 |

Table 13: Metric Grid Results for WLI Image, Batch B Specimens, 6-hr Exposure, 1000 μm Resolution

| Specimen | Critical Crack Location | | Max. | | Critical Location % | |
|----------|-------------------------|---------|---------|---------|---------------------|-------|
| | R_a | R_q | R_a | R_q | R_a | R_q |
| 544-8C | 5.7124 | 7.1536 | 8.4398 | 9.119 | 99.0 | 99.4 |
| 544-10C | 3.039 | 3.586 | 7.538 | 8.418 | 85.1 | 83.3 |
| 547-6A | 4.2875 | 5.389 | 8.503 | 9.42 | 93.6 | 94.9 |
| 547-20B | 4.692 | 5.429 | 8.4564 | 9.556 | 97.3 | 96.6 |
| 547-36B | 7.2576 | 8.3671 | 8.6128 | 9.6417 | 99.8 | 99.8 |
| 544-3B | 5.8199 | 7.103 | 10.522 | 12.2359 | 97.3 | 97.3 |
| 547-16B | 3.2621 | 4.3229 | 7.864 | 9.6029 | 88.4 | 91.1 |
| 547-2C | 5.3591 | 6.2932 | 10.2866 | 11.5859 | 98.5 | 98.0 |
| 547-31B | 4.9242 | 5.6289 | 8.6817 | 9.6783 | 97.9 | 97.4 |
| 614-3 | 2.3209 | 2.9939 | 8.4912 | 9.3304 | 77.3 | 77.2 |
| 614-8 | 5.579 | 6.6038 | 8.5887 | 10.162 | 97.1 | 97.3 |
| 614-13 | 6.7249 | 8.5335 | 9.631 | 10.47 | 98.7 | 99.5 |
| 614-5 | 4.8292 | 5.8754 | 8.796 | 10.153 | 94.8 | 95.4 |
| 614-6 | 9.9308 | 10.9466 | 11.883 | 13.5319 | 99.5 | 99.3 |
| 614-19 | 5.5015 | 6.3388 | 8.9858 | 10.0879 | 97.0 | 96.7 |

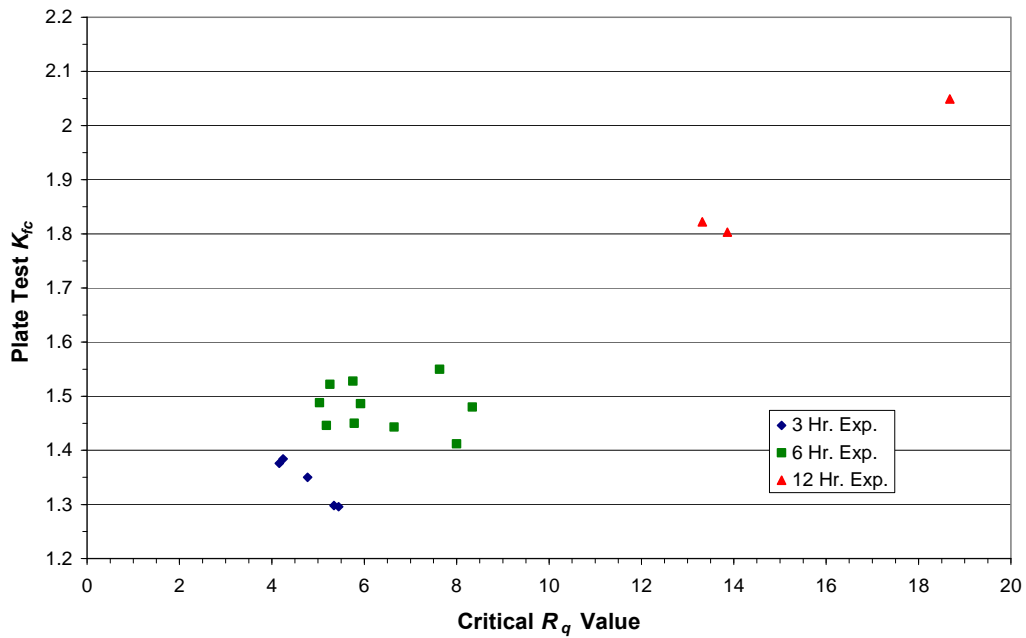


Figure 23: Plate Test K_{fc} versus Critical R_q Value for Batch A C-F Plates, 1000 μm Resolution

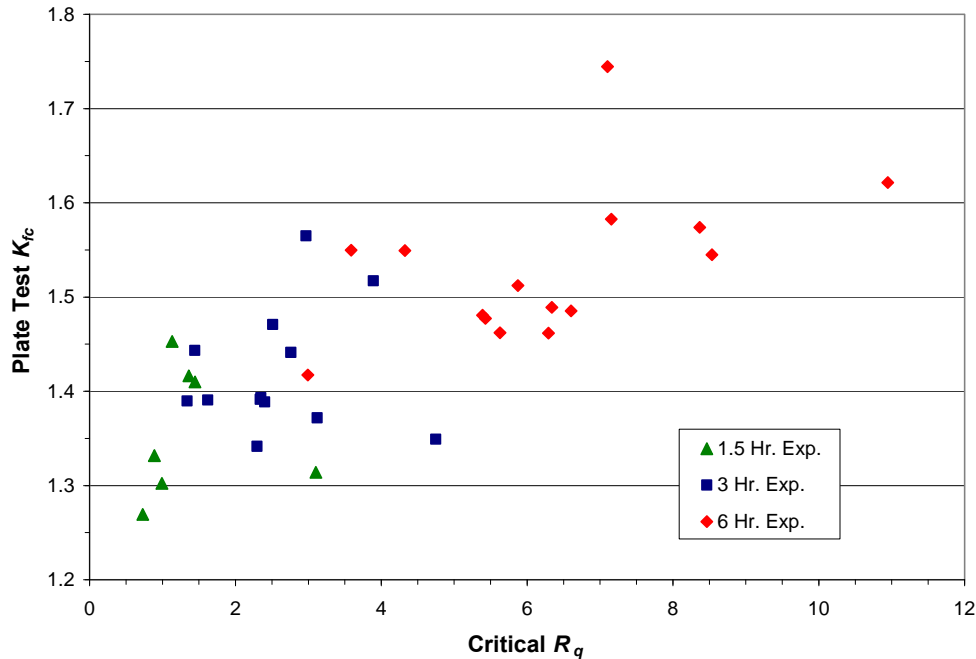


Figure 24: Plate Test K_{fc} versus Critical R_q Value for Batch B C-F Plates, 1000 μm Resolution

The plots show a significant amount of scatter, but a linear correlation can be discerned. Coefficients for least-squares linear regression fit of the data are listed in table 14 for both batches of C-F test data.

Table 14: Linear Regression Coefficients for Plate Test K_{fc} versus Critical R_a and R_q Data, 1000 μm Resolution

| Test Data | Slope | Intercept | RMSE | R^2 |
|-----------------|-----------------------|-------------------|--------|-------|
| R_a - Batch A | 0.06058 ± 0.01396 | 1.168 ± 0.088 | 0.0803 | 0.841 |
| R_a - Batch B | 0.03111 ± 0.01129 | 1.353 ± 0.045 | 0.0727 | 0.488 |
| R_q - Batch A | 0.04612 ± 0.00971 | 1.168 ± 0.081 | 0.0744 | 0.864 |
| R_q - Batch B | 0.02805 ± 0.00956 | 1.344 ± 0.045 | 0.0704 | 0.519 |

The variability in the corresponding plate K_{fc} value for a given WLI roughness metric value must be propagated through the life prediction calculations to adequately capture the correlation uncertainty in the final reliability result. However, this process generally involves a substantial amount of Monte Carlo simulation, which was not practical given the remaining time constraints in the C-F program. An alternative is to choose a conservative upper bound on the correlation model, such that the true plate K_{fc} value has a high probability of being less than the value specified by the correlation model. Choosing an upper bound probability of, say 99%, a revised zero intercept parameter can be found by shifting the regression curve by 2.326 standard deviations. Using the baseline parameter and RMSE values from table 14 for each data set, the revised parameter values for the 99th percentile plate K_{fc} correlation curves are listed in table 15.

Table 15: Linear Regression Coefficients for the 99th Percentile Plate Test K_{fc} versus Critical R_a and R_q Data, 1000 μm Resolution

| Test Data | Slope | Intercept |
|-----------------|---------|-----------|
| R_a - Batch A | 0.06058 | 1.355 |
| R_a - Batch B | 0.03111 | 1.522 |
| R_q - Batch A | 0.04612 | 1.341 |
| R_q - Batch B | 0.02805 | 1.508 |

The results of the previously described analysis indicate that a roughness metric grid approach could be used to predict the critical K_{fc} value for corrosion-damaged AF1410 plates; however, the correlation has been calibrated using high-resolution WLI scans, which would generally not be available at fleet deployed locations. To examine the effect that reduced image scan resolution has on computing roughness metric values, a study was performed to provide insight into the limitations of determining metrics from traditional NDI techniques, like ultrasound, that have a poorer spatial resolution than the WLI microscope used to create surface profiles. Starting with the WLI profiles for a number of Batch B specimens, the RMS roughness was calculated in a circular region positioned inside the corrosion patch. The diameter of the circle was slightly smaller than the diameter of the circular patch of corrosion. Each image was filtered with Gaussian blur filters of various widths to simulate different spatial resolutions. RMS values were determined for each processed image in the circular ROI. RMS values were normalized by the RMS value of the original white light profile and were plotted as a function of the Gaussian blur full width at half maximum in mils.

Figure 25 shows a plot of normalized RMS versus Gaussian blur full width at half maximum for 1.5-hr exposure data on some of the Batch B specimens. Figure 26 is a plot of several 3-hr exposure specimens. Also shown in each plot is a best-fit line with the corresponding equation. It is interesting to note that the slope of the fit is similar for all data. Apparently, the effect of the low-pass filter is to reduce the effective roughness, but in a manner such that the effective roughness is proportional to the actual roughness determined from the full-resolution white light profile. This suggests that the surface profile characteristics are present across a range of spatial frequencies. When the low-pass filter removes the higher frequencies, there are still lower-frequency roughness components present to give an indication of the overall roughness.

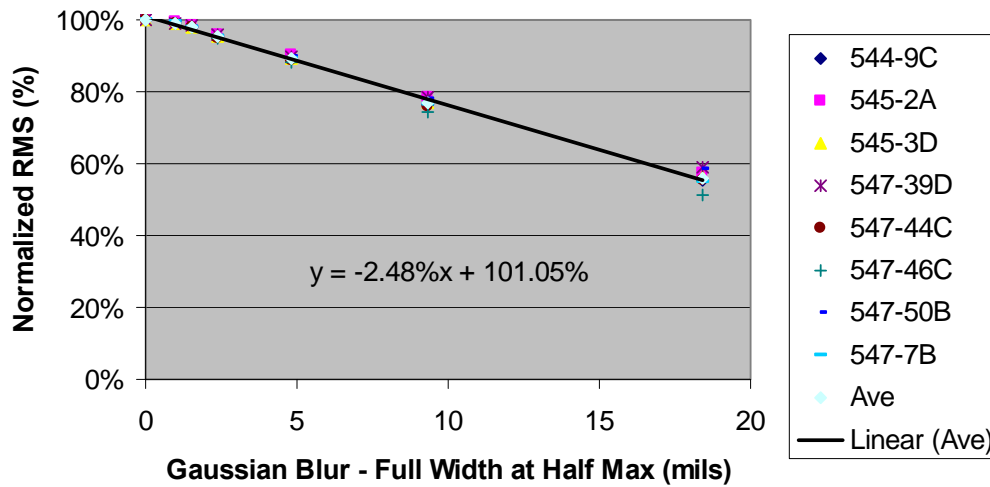


Figure 25: Normalized RMS versus Gaussian Blur Full Width at Half Maximum for Several Batch B 1.5-hr Exposure Specimens

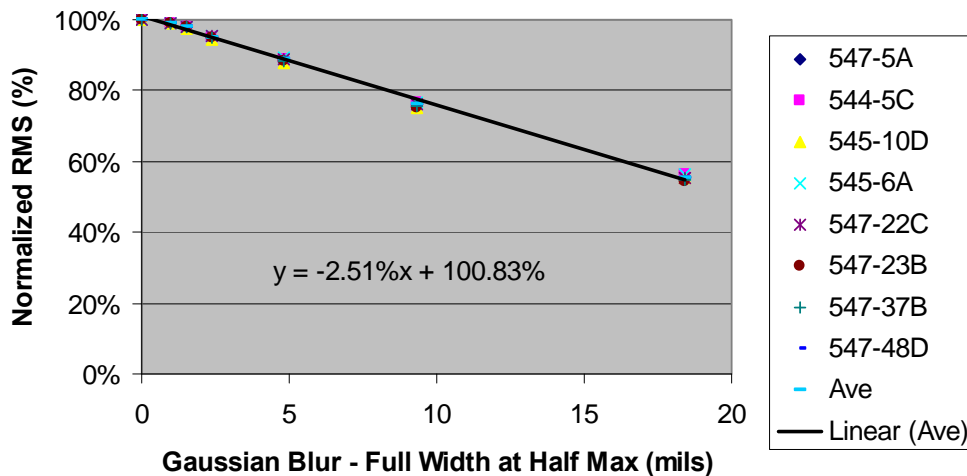


Figure 26: Normalized RMS versus Gaussian Blur Full Width at Half Maximum for Several Batch B 3-hr Exposure Specimens

Figure 27 is a plot of the normalized RMS versus the Gaussian blur full width at half maximum for a specimen from Batch A that had been exposed for 6 hr. This figure shows RMS both inside and outside the corrosion patch. As can be seen in this plot, there is a deviation of the RMS in the corrosion patch from a straight line. It is believed that this is due to the fact that the Batch A specimens were grit blasted prior to growing corrosion, leaving the surface with a dimpled texture, even outside of the corrosion patch. The effect of filtering on this grit-blasted surface roughness is seen in the curve representing the region outside the corrosion patch. Apparently, the grit-blasted surface contains a significant amount of high-frequency roughness. As the low-

pass filter removes these higher-frequency components, the effective roughness decreases dramatically. This knowledge helps explain the shape of the curve for the RMS values in the corrosion patch. There appears to be a significant influence on the RMS value of the original WLI profile due to the surface roughness from the grit blasting. As the low pass filter is applied to remove more of the high-frequency roughness components, relatively more of the roughness due to the corrosion is left, which shows a similar behavior to that shown on the Batch B specimens. Since the Batch B specimens were not grit blasted and had a much smoother surface prior to growing corrosion, there is only the corrosion roughness characteristic present in these specimens.

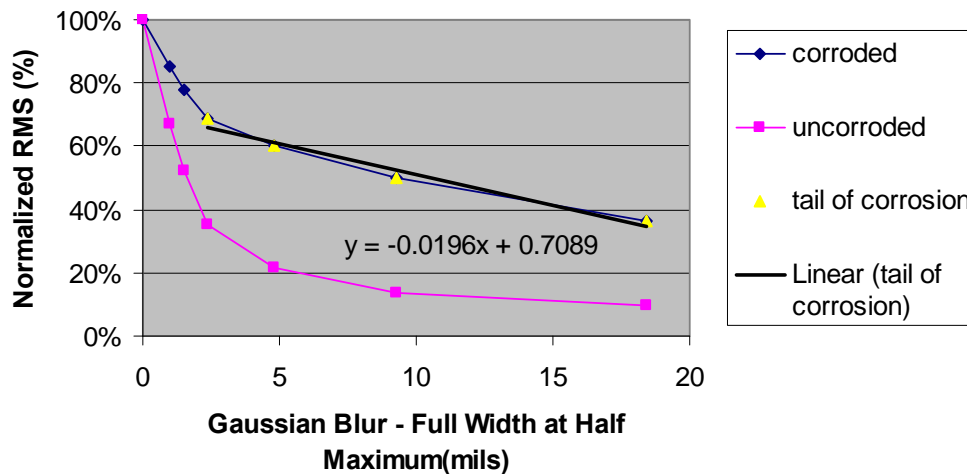


Figure 27: Normalized RMS versus Gaussian Blur Full Width at Half Maximum for Batch B 6-hr Exposure Specimen 37

For reference, the RMS roughness values of the specimen, shown in figure 27, for the original WLI profile inside and outside the corrosion patch were 5.3 and 4.1 microns, respectively. Average RMS roughness values for the Batch B specimens shown in figures 25 and 26 are 1.2 and 2.2 microns, respectively. RMS roughness sampled outside the corrosion patch for three different Batch B specimens ranged from 0.1 to 0.4 microns. Apparently, the roughness of the surface prior to growing corrosion has a significantly smaller effect on the roughness of the corrosion patch after corrosion for Batch B compared to Batch A. One possible hypothesis that could be made from these observations is that a poorer-resolution inspection might actually give a better measure of roughness due to corrosion. The poor-resolution inspection is less sensitive than the better-resolution WLI instrument to the higher-frequency components present in the grit-blasted surface. However, more research would be required to confirm this hypothesis. These results and interpretations are assumed to equally hold for the average roughness metric measure.

The RMS roughness resolution study clearly shows that the roughness metric values will change significantly when the image resolution is reduced. Therefore, an additional correlation must be carried out to relate the roughness metric values from low-resolution NDI images to those calculated from high-resolution WLI scans. For the AF1410 C-F specimens, it was not possible to go directly from NDI images to a plate K_{fc} correlation in all cases, since not all test specimens had NDI images taken prior to testing. The following study makes use of Batch B C-F measurements of surface height profiles using ultrasonic (UT) time-of-flight and corresponding WLI profiles for the same test specimens. Data from nine specimens were used to calculate roughness values in a grid overlaid on the corrosion patch; each grid element was 1 mm by 1 mm. The specimens included three from each of three different corrosion exposure levels (1.5, 3, and 6 hr) in order to make use of a range of corrosion severities. With each grid, tilt was removed prior to calculation of RMS roughness in the form of the parameter R_q . Figure 28 shows UT R_q versus WLI R_q for the 1.5-hr exposure specimens, figure 29 contains the 3-hr exposure plots, and figure 30 contains the 6-hr exposure data. Notice the change in scale. In each figure, the grid data are given by the dark blue diamonds, while a line with a slope of one and a zero intercept is shown in purple. This line represents an ideal correlation between the UT and WLI data. Obviously, the data do not fit the ideal correlation line; however, they do show that there is a correlation.

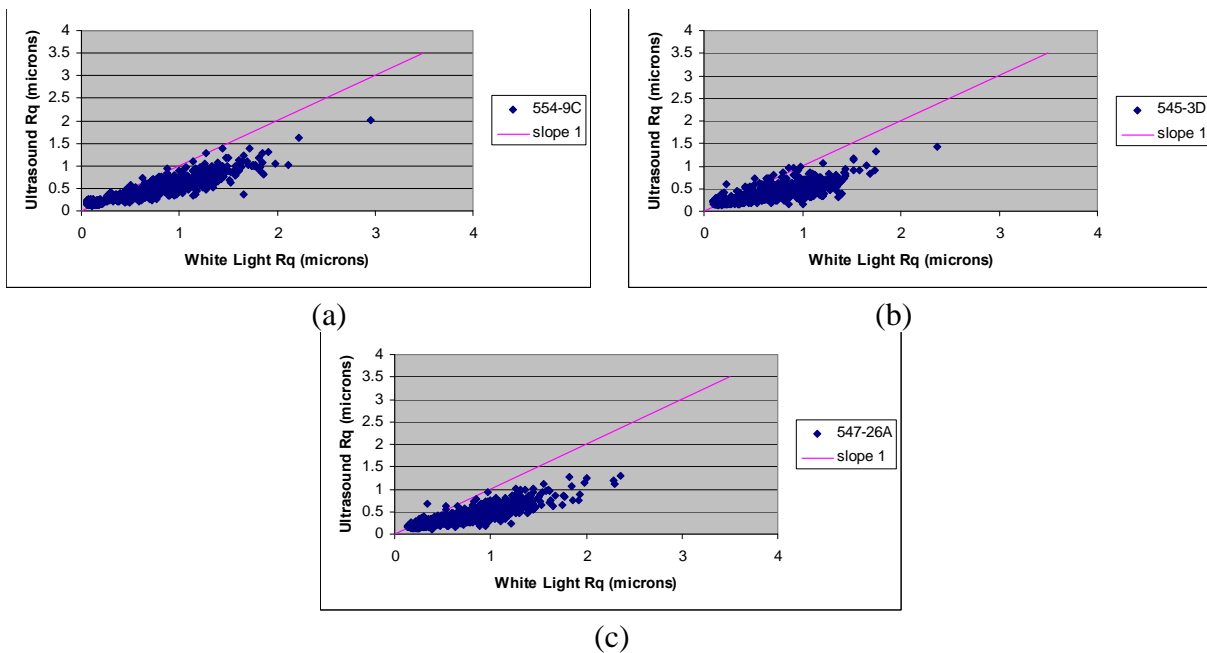


Figure 28: Plots of R_q for UT versus R_q of WLI for 1.5-hr Exposure Data on Batch B Specimens: (a) 544-9C, (b) 545-3D, and (c) 547-26A

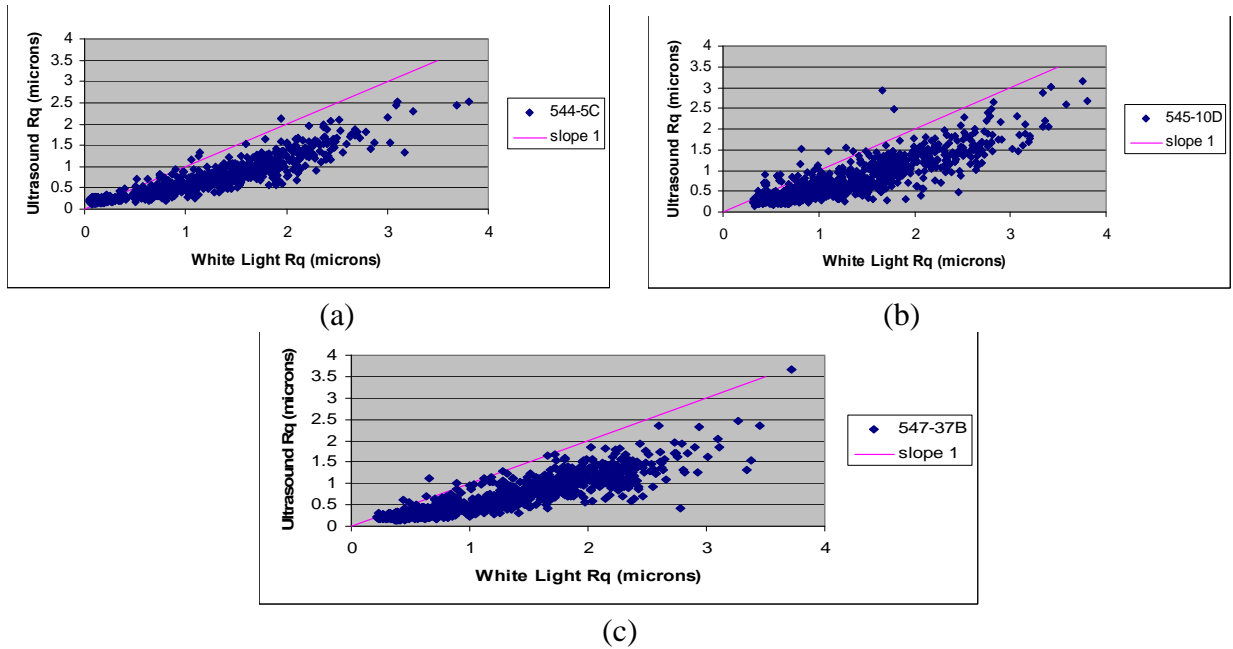


Figure 29: Plots of R_q for UT versus R_q of WLI for 3-hr Exposure Data on Batch B Specimens: (a) 544-5C, (b) 545-10D, and (c) 547-37B

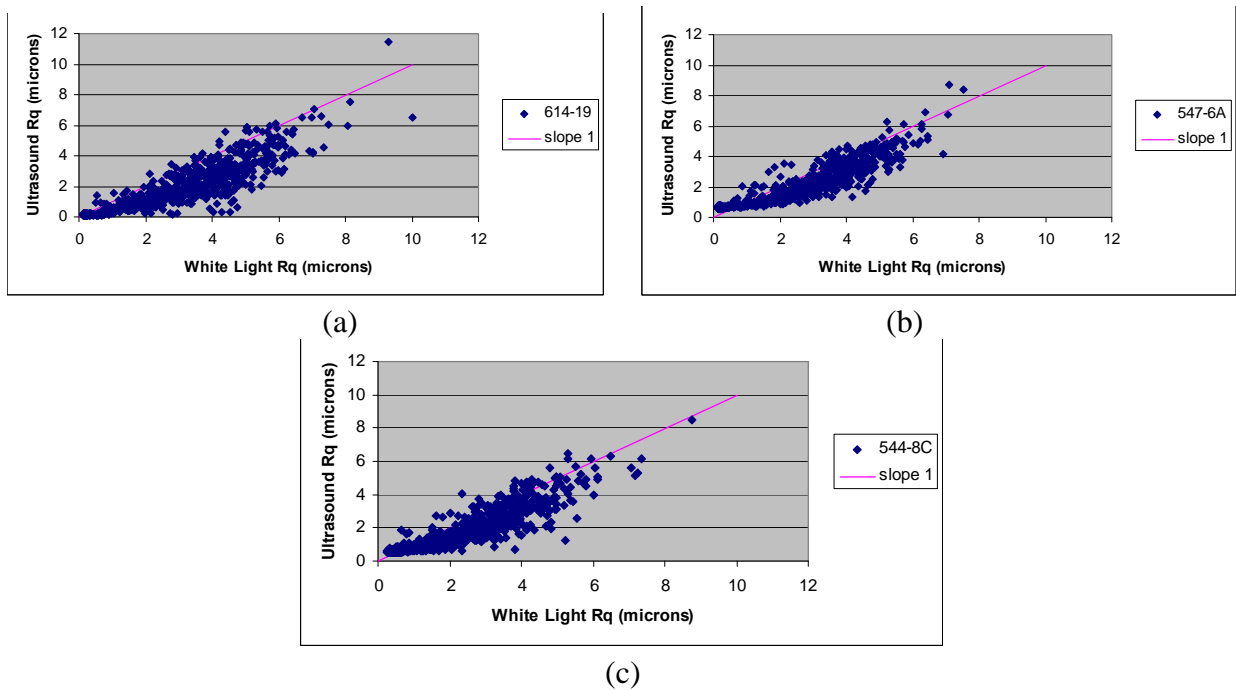


Figure 30: Plots of R_q for UT versus R_q of WLI for 6-hr Exposure Data on Batch B Specimens: (a) 614-19, (b) 547-6A, and (c) 544-8C

There are some interesting observations to note in these plots. First, the trends in the data are not linear, but a leveling off is apparent at small WLI R_q values. This is interesting because it suggests that the UT data approach a minimum nonzero value. Physically, the grid elements with very small WLI R_q values represent areas on the C-F specimens without corrosion (outside the corrosion patches). This means that the UT measurements are showing a level of roughness that is really independent of the actual surface roughness in these grid elements. This represents a noise floor in the UT profile measurements. This can be caused by vibration or mechanical dither in the transducer standoff that causes the time-of-flight measurement in the ultrasonic signal to vary randomly at a small level, giving the appearance of a rough surface – even when the surface is actually very flat. This noise could also be of an electronic nature, caused by variations in sampling (digitizing) of the signal in the time domain. In either case, the time-of-flight variations would be expected to be present in all of the UT measurements, but be more noticeable on the smooth, uncorroded regions of the sample. Notice that the noise is different for each set. The second observation from this data is that the scatter in the UT roughness increases with WLI roughness. This points out that, while there is a general correlation, there is still quite a bit of UT roughness variation from grid element to grid element for the same WL roughness. This suggests that the actual UT response is a complicated phenomenon that is dependent on the actual surface profile in the grid. It might not be possible to do any better than to produce a model of the data that accounts for an assumed random variable representing the effects of the detailed corrosion profile on the UT response.

With these observations in mind, a simple model presents itself. Since R_q is essentially a standard deviation of the surface profile, the limiting value of the UT roughness at small WLI roughness values represents the standard deviation of the time-of-flight variations, or noise. Since variances add together, the simple model would suggest that the measured UT R_q value (UT_m) is given by the following:

$$UT_m = \sqrt{UT_0^2 + N^2} \quad (43)$$

where UT_0 is the actual UT R_q value that would be measured if the noise were not present and N is the noise, as a standard deviation. N is measured by averaging the UT_m at small WLI R_q values. So, the corrected UT roughness value is:

$$UT_0 = \sqrt{UT_m^2 - N^2} \quad (44)$$

After studying several different models, this simple empirical model seemed best:

$$\ln(UT_m^2 - N^2) = m \ln(WL) + b + \varepsilon \quad (45)$$

The parameter ε is the model fit error (normally distributed) with a mean of zero and some standard deviation. In fitting this model to the data, all data points for which UT_m is less than N had to be eliminated from the fit to avoid undefined logarithms. In addition, there seemed to be a

slope change for points at $\ln(WL)$ equals -1.0 ; therefore, all points with $\ln(WL)$ less than -1.0 were eliminated. Figure 31 shows the data plotted as $\ln(UT_m^2 - N^2)$ versus $\ln(WL)$ for the 1.5-hr exposure data.

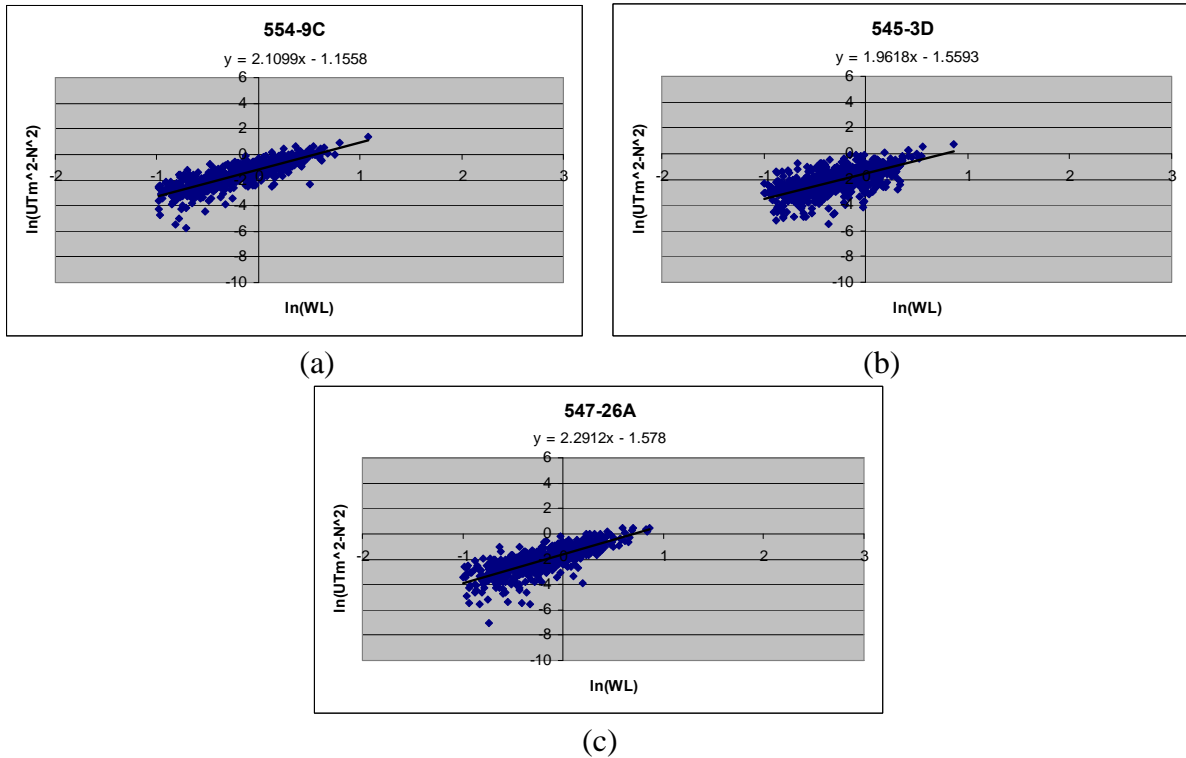


Figure 31: Log-Log UT versus WLI R_q Plots for 1.5-hr Exposure Data on Batch B Specimens: (a) 544-9C, (b) 545-3D, and (c) 547-26A

Figure 32 contains the 3-hr exposure data and figure 33 shows the 6-hr exposure data. Table 16 shows all of the slopes and intercepts for these fits.

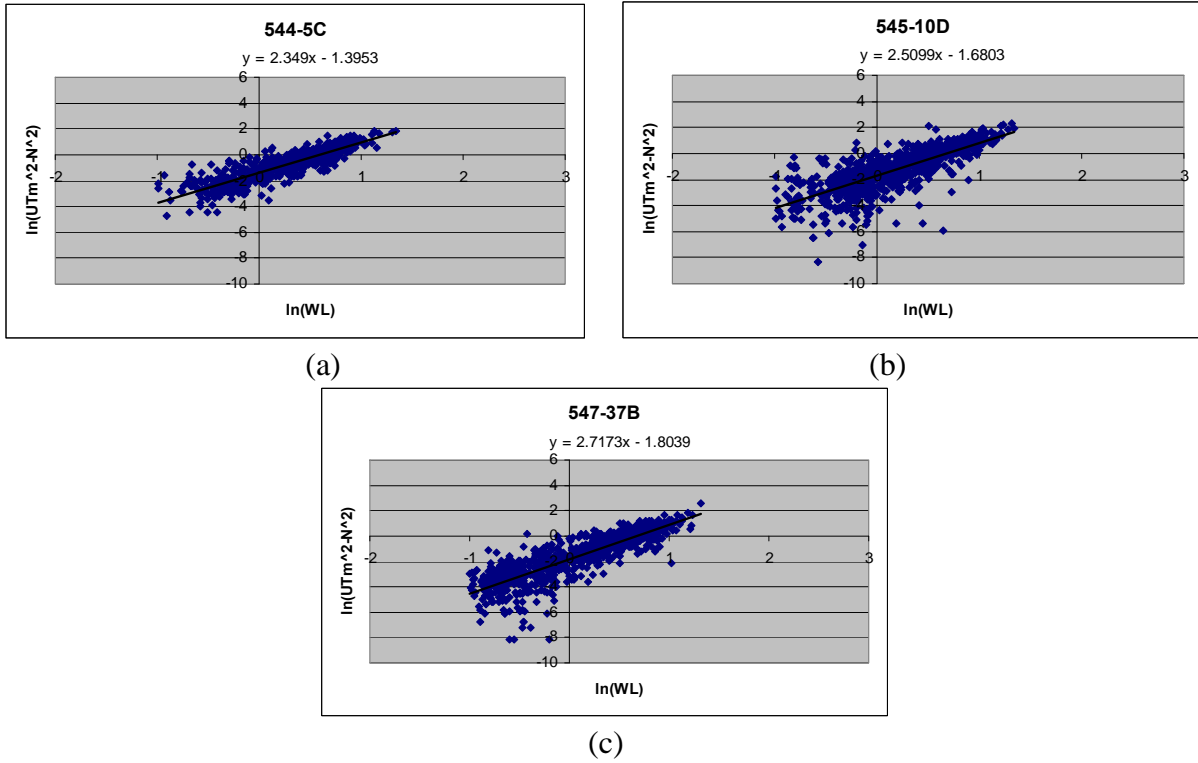


Figure 32: Log-Log UT versus WLI R_q Plots for 3-hr Exposure Data on Batch B Specimens: (a) 544-5C, (b) 545-10D, and (c) 547-37B

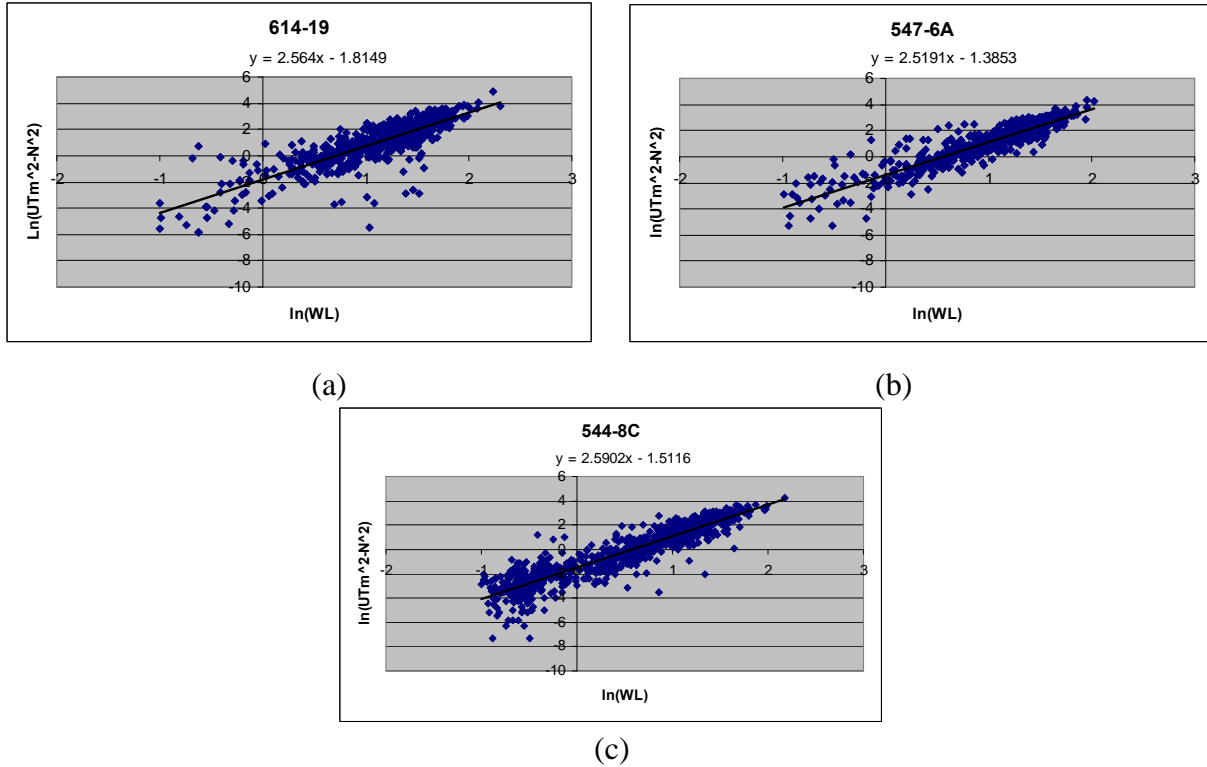


Figure 33: Log-Log UT versus WLI R_q Plots for 6-hr Exposure Data on Batch B Specimens: (a) 614-19, (b) 547-6A, and (c) 544-8C

Table 16: Slopes and Intercepts of Log-Log UT versus WLI R_q Fits

| Run | Exposure (hr) | Slope | Intercept |
|---------|---------------|-------|-----------|
| 554-9C | 1.5 | 2.11 | -1.16 |
| 545-3D | 1.5 | 1.96 | -1.56 |
| 547-26A | 1.5 | 2.29 | -1.58 |
| 544-5C | 3 | 2.35 | -1.40 |
| 545-10D | 3 | 2.51 | -1.68 |
| 547-37B | 3 | 2.72 | -1.80 |
| 547-6A | 6 | 2.52 | -1.39 |
| 544-8C | 6 | 2.59 | -1.51 |
| 614-19 | 6 | 2.56 | -1.81 |
| Average | | 2.40 | -1.54 |

The slopes of the individual fits vary, but not in a consistent manner. While the slope is slightly higher for the longer exposures, there are problems with defining a clear trend. The largest slope is actually for a set of 3-hr data and there is a 1.5-hr set of data that is not much different than one of the 3-hr sets of data. It is even harder to establish a trend in the intercept data. The above plots are all shown with the same scales; to the eye, these data sets could very well belong to the same population. There are similar slopes, intercepts, and even scatters between the plots. With

this observation in mind, all of the data has been plotted on a single graph as one set of data. In this plot, only data points from the above plots where $\ln(WL)$ is greater than -0.5 have been plotted. This was due to the apparent increase in scatter at the smaller WLI values. As will be seen, this limit on the data, while apparently justified, may not have been high enough. Figure 34 shows all data, limited as described in the previous paragraphs, as $\ln(UT_m^2 - N^2)$ versus $\ln(WL)$.

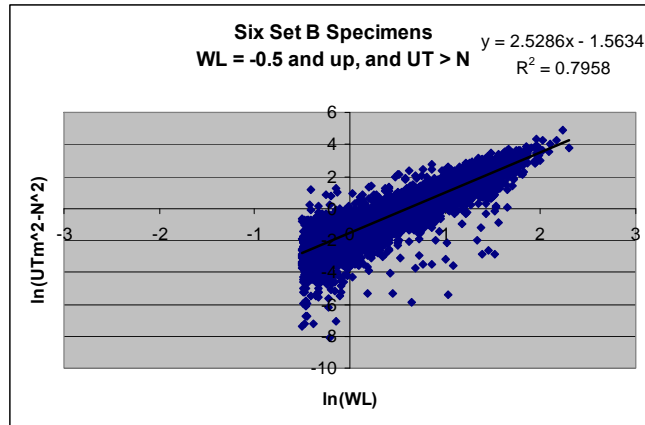


Figure 34: Log-Log UT versus WLI R_q Plot for Six Batch B Specimens

The equation of the fit is given in the upper right corner of the figure. It is seen that the slope and intercepts are within those given in table 16. In order to better understand the scatter in the data, the standard deviation of the differences from the fit had been calculated: 0.78. The plot seems to show that the variance is decreasing with an increase in WLI. To test this, the data were partitioned into bins as follows: -0.5 to 0 , 0 to 0.5 , 0.5 to 1.0 , 1.0 to 1.5 , and 1.5 to 2.0 . The standard deviations for each bin are given in table 17.

Table 17: Standard Deviations of Regression Fit Error for Bins of WLI $\log(R_q)$ Values

| Bin | Standard Deviation |
|------------|--------------------|
| -0.5 to 0 | 0.93 |
| 0 to 0.5 | 0.71 |
| 0.5 to 1.0 | 0.65 |
| 1.0 to 1.5 | 0.76 |
| 1.5 to 2.0 | 0.65 |

From this table, it is apparent that the standard deviation does not change much, if at all above $\ln(WL)$ equals zero. Below this value, the scatter increases with decreasing $\ln(WL)$. It is hypothesized that this is due to the fact that the UT data are small and can actually be less than the noise. While these points have been removed, there are still others that approach the noise value and, therefore, will fall at large negative values on this plot. These points increase the scatter in the plot. The limit of zero for $\ln(WL)$ means that only WLI R_q values greater than $1 \mu\text{m}$ are being considered.

With this model in hand, the UT R_q measurements can be inverted to find the WLI R_q values, with the understanding that the WLI values are the independent variable and the UT is a measurement of this value. The variability in the corresponding WLI value for a given UT metric value must be propagated through the life prediction calculations to adequately capture the correlation uncertainty in the final reliability result. However, this process also involves a substantial amount of Monte Carlo simulation, which was not practical given the remaining time constraints in the C-F program. An alternative is to choose a conservative upper bound on the correlation model, such that the true WLI metric value has a high probability of being less than the value specified by the correlation model. Inverting the correlation equation gives the WLI metric value as a function of the UT metric value and the error.

$$\ln(WL) = \frac{1}{m} [\ln(UT_m^2 - N^2) - b - \varepsilon] \quad (46)$$

Choosing an upper bound probability of 99%, as was the case for the WLI R_q to plate K_{fc} correlation, a revised zero intercept parameter (b') can be found by shifting the regression curve by -2.326 standard deviations. Using the baseline parameter values from figure 34 for the combined data set, and the average error standard deviation for table 17 bins greater than zero, the revised correlation equation for the 99th percentile WLI R_q values is:

$$\begin{aligned} \ln(WL') &= \frac{1}{m} [\ln(UT_m^2 - N^2) - b'] = \frac{1}{2.529} [\ln(UT_m^2 - N^2) - (-1.563 - 2.326 * 0.693)] \\ &= \frac{1}{2.529} [\ln(UT_m^2 - N^2) + 3.175] \end{aligned} \quad (47)$$

Using the statistical upper bound correlation equations for UT R_q values to WLI R_q values, and from WLI critical R_q values to plate K_{fc} values, quasi-probabilistic life predictions can be made using the combined notch approach derived for the ESR model. For the roughness metric method, it is assumed that a single notch is present within each grid square, with a K_{fc} value derived from the correlation equations for the UT R_q values. The set of K_{fc} values from the entire grid space can then be grouped into histograms as is done in the ESR method. The grid-based approach also allows for the consideration of gradient stress fields in the corroded area, as the resulting K_{fc} values for each grid square can be modified by adjusting the K_{fc-eff} values by the average stress in each respective grid square.

VERIFICATION AND VALIDATION OF CORROSION-FATIGUE MODELS

Verification and Validation (V&V) is an essential part of the development of computational models that describe physical phenomenon, and is necessary both to ensure that the software tools developed to implement the models produce the intended result, and to define the range of applicability of the computational results to real-world problems. Four unique data sets are available for validating AF1410 C-F models: Batch A and Batch B C-F specimens; Cad-plated C-F specimens; Micromachined specimens; Corroded arresting shanks. Batch A and Batch B specimens have the largest number of samples but were used to calibrate the predictive models, and therefore cannot be used to perform an independent model validation. However, life predictions made for this data set can be used to assess the accuracy and uncertainty of the modeling approaches. The cad-plated specimens represent a small sample size tested at one stress level, and use a corrosion exposure method that is different from the one used to create the model calibration data set. That makes this data set a good candidate for validation, and would demonstrate that the modeling approach is not dependent on how the corrosion was incurred on the surface. The micromachined specimens are a small sample with identical notch features, however the features are an order of magnitude larger than the corrosion features that cause fatigue cracking. As such, this data set can be used for limited validation of the traditional notched fatigue approach, and to assess the underlying uncertainty when errors associated with approximating corrosion notch geometries and stress concentrations are eliminated. However, it is not suitable for validating C-F models. Corroded arresting shanks represent the most robust validation case, because they are subject to service-induced corrosion damage and incorporate stress gradient effects and spectrum loading typical of actual aircraft components. However, none of the shanks that were tested failed due to corrosion damage, so the test results only represent suspended data points for C-F failure.

The initial approach to V&V was to develop a framework for the various components of the NAVAIR C-F modeling effort, using the format suggested in the ASME Guide for Verification and Validation in Computational Solid Mechanics [26]. A bottom-up approach to V&V was utilized for this program. The corrosion modeling and test program for AF1410 steel is broken down into elemental building blocks (B1-B4) of increasing model complexity, as shown in figure 35.

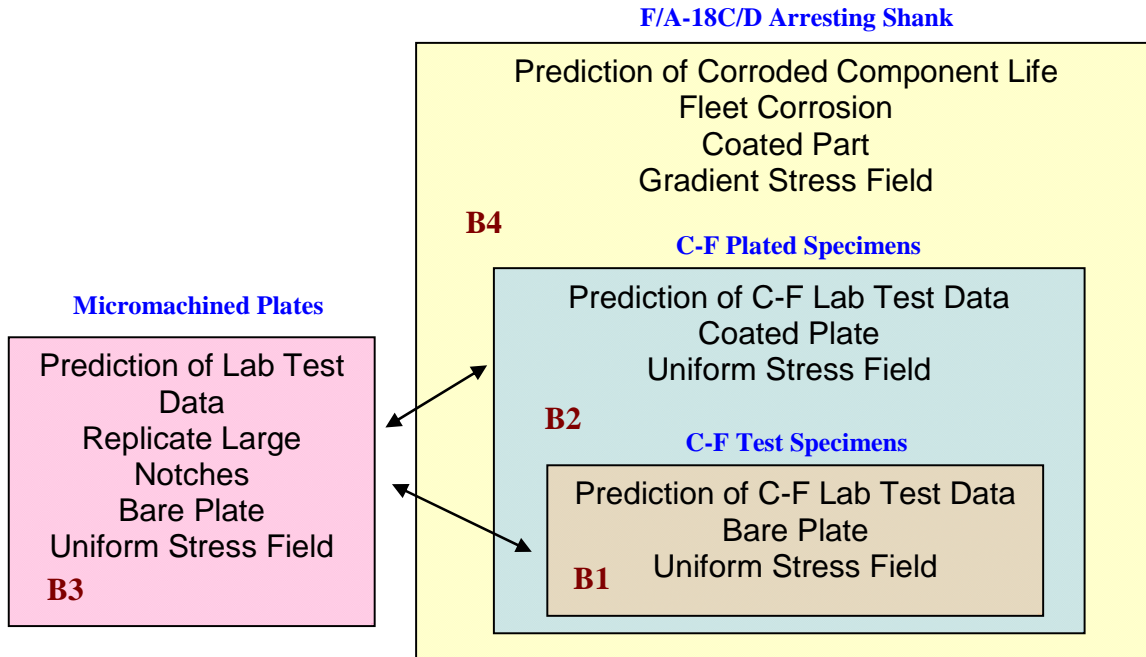


Figure 35: Hierarchical Structure of C-F Life Characterization Complexity

V&V activities were carried out in each building block of the hierarchical structure, with flowcharts in appendix A showing how the various modeling and testing activities relate to each other. Block 1 is divided into sub-blocks A and B for the ESR and roughness metric prediction methods, respectively. To provide guidance on the level of effort required to perform V&V on the models developed in the program, task lists were developed that break down the code verification, calculation V&V work for each element in the ESR and roughness metric models.

Code verification tasks:

1. PSL Curve to PSL Code (Boeing)
2. FFT K_t Transformation to FFT K_t Algorithm (UDRI)
3. ROI Search Criteria to ROI Search Algorithm (UDRI)
4. Notch Metric to ESR Life Prediction Algorithm (Boeing)
5. Notch Sensitivity Curve to ESR Life Prediction Algorithm (Boeing)
6. ESR Life Prediction Logic to ESR Life Prediction Algorithm (Boeing)
7. Roughness Metric Formulas to Roughness Metric Algorithm (Boeing)
8. Roughness Metric Correlation to Roughness Metric Algorithm (Boeing)
9. Equivalent Geometric Stress Concentration Logic to ESR Shank Life Prediction Algorithm (Boeing)
10. Equivalent Geometric Stress Concentration Logic to Metric Shank Life Prediction Algorithm (Boeing)
11. Shank FEM assumptions to Shank FE Model (ESRD)

Calculation verification tasks:

1. PSL Code to ESR Probabilistic Life Predictions (Boeing)
2. FFT K_t Algorithm to ESR Probabilistic Life Predictions (UDRI)
3. ROI Search Algorithm to ESR Probabilistic Life Predictions (UDRI)
4. ESR Life Prediction Algorithm to ESR Probabilistic Life Predictions (Boeing)
5. Roughness Metric Algorithm to Metric-Based Probabilistic Life Predictions (Boeing)
6. Metric Life Prediction Algorithm to Metric-Based Probabilistic Life Predictions (Boeing)
7. ESR Shank Life Prediction Algorithm to ESR Probabilistic Life Predictions (Boeing)
8. Metric Shank Life Prediction Algorithm to Metric-Based Probabilistic Life Predictions (Boeing)
9. Shank FE model to ESR and Metric-Based Probabilistic Life Predictions (ESRD/Boeing)

Validation Tasks:

1. Confidence bounds on ESR Probabilistic Life Predictions
 - a. Identification of sources of uncertainty (NAVAIR/UDRI/Boeing)
 - b. Input uncertainty distributions (NAVAIR/UDRI/Boeing)
 - c. Sensitivity analysis (NAVAIR/UDRI/Boeing)
 - d. Confidence bounds on life predictions (NAVAIR)
2. Comparison of ESR Probabilistic Life Predictions with AF1410 Batch A and Batch B C-F test results. (NAVAIR)
3. Confidence bounds on Metric-Based Probabilistic Life Predictions
 - a. Identification of sources of uncertainty (NAVAIR/UDRI/Boeing)
 - b. Input uncertainty distributions (NAVAIR/UDRI/Boeing)
 - c. Sensitivity analysis (NAVAIR/UDRI/Boeing)
 - d. Confidence bounds on life predictions (NAVAIR)
4. Comparison of Metric-Based Probabilistic Life Predictions with AF1410 Batch A and Batch B C-F test results. (ESRD)
5. Confidence bounds on ESR and Metric-Based Probabilistic Life Predictions for Cad-Plated C-F Specimens
6. Comparison of ESR and Metric-Based Probabilistic Life Predictions with Cad-Plated C-F test results. (ESRD)
7. Confidence bounds on ESR Probabilistic Life Predictions of Large Notch Plates (micromachine specimens).
 - a. Identification of sources of uncertainty (NAVAIR/UDRI/Boeing)
 - b. Input uncertainty distributions (NAVAIR/UDRI/Boeing)
 - c. Sensitivity analysis (NAVAIR/UDRI/Boeing)
 - d. Confidence bounds on life predictions (NAVAIR)
8. Comparison of ESR Probabilistic Life Predictions with Large Notch plate test results. (ESRD)
9. Shank FE model to Shank Strain Survey Results (ESRD)
10. Confidence bounds on ESR and Metric-Based Probabilistic Shank Life Predictions
 - a. Identification of sources of uncertainty (NAVAIR/UDRI/Boeing)
 - b. Input uncertainty distributions (NAVAIR/UDRI/Boeing)
 - c. Sensitivity analysis (NAVAIR/UDRI/Boeing)

d. Confidence bounds on life predictions (NAVAIR)
11. Comparison of ESR and Metric-Based Probabilistic Shank Life Predictions with Corroded Shank test results (ESRD)

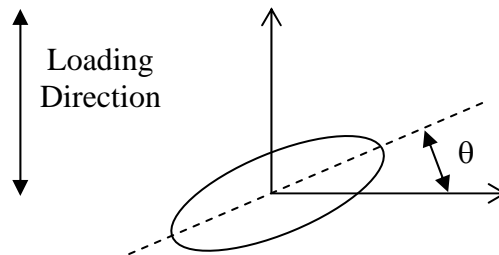
As part of the validation process, acceptability criteria for successful validation must be specified. According to formal validation requirements, it is desirable to specify acceptability criteria prior to model development and testing. However, this was not practical for the type of model development undertaken in this program. Since there were no prior C-F models in use by NAVAIR or its contractors, there is no historical knowledge base to draw from to set such criteria. It was clear that an engineering validation criteria would be necessary, since exact scientific accuracy is not required in order to provide a useful tool for fleet management. Informal NAVAIR discussions of model capability led to a preliminary engineering validation criteria of a factor of 1 to 4 conservatism in model median life prediction error at the 95% confidence level, with all predictions being conservative. This was seen as an initial general-case criteria, with specific criteria set on a case-by-case basis for each application. The key question with regards to validation of C-F models is what constitutes an overly-conservative prediction? Without having a model that has been implemented and used for fleet management activities, this question cannot currently be answered. The V&V work described herein represents the best efforts of the C-F research program participants to fulfill the requirements of a robust V&V process.

RESULTS

REGION OF INTEREST K_{fc} PREDICTION CORRELATION

The ability of the ROI algorithm to find the notches that caused the critical fatigue cracks in the AF1410 C-F plates was tested by running the algorithm on the elasticity solution K_t maps for all of the test plates, except for the 12-hr Batch B exposure set. An ROI was identified for the critical notch on all of the 3- and 6-hr exposure Batch A plates that cracked in the corrosion patch, as well as all of the 6-hr exposure Batch B plates. For the 3-hr exposure Batch B plates, an ROI was identified for all but one of the critical notches. For the 1.5-hr exposure Batch B plates, an ROI was identified for the critical notches on 7 of the 12 plates that cracked in the corrosion patch. The low identification rate on the 1.5-hr exposure plates was likely due to the light amounts of corrosion present on these specimens.

Notch K_t values for all of the ROI features detected on a corrosion patch can be calculated using the notch metric equations described previously, with the notch width and height values extracted from the ROI feature measurement tool in ImageJ, and the notch depth calculated from the WLI image. The ROI feature measurement tool extracts major and minor axes dimensions from the enclosed ROI area, and calculates an inclination angle of the major axes with respect to the image axes. The inclined notch K_t values were corrected for loading axis orientation on the test specimens by the equation shown in figure 36.



$$K_t = K_{t-90^\circ} + (K_{t-0^\circ} - K_{t-90^\circ}) \cos^2 \theta$$

Figure 36: Notch Orientation K_t Correction Equation

The notch metric K_t values derived from the ROI analyses were used for all subsequent calculations, since this method was shown to give more accurate and repeatable results compared to using the maximum K_t value in the enclosed ROI area that was calculated by the elasticity solution. With the individual notch K_t values defined for each ROI, the K_{fc} values can be estimated from equation 1 by calculating the equivalent notch root radius using equation 5 and calculating the corresponding q_c value from equation 6. Correlations between the critical notch

K_{fc} values calculated from the ROI analysis, and the values calculated from the experimental test results are listed in tables 18 through 21, and are shown graphically in figures 37 and 38.

Table 18: Batch A Critical Notch ROI Correlations (WLI Median Filter)

| Specimen | Total ROIs | Critical ROI K_t | Critical Meas. K_t | Critical ROI K_{fc} | Plate Test K_{fc} | Max. ROI K_{fc} | Critical ROI K_{fc} % |
|---------------|------------|--------------------|----------------------|-----------------------|---------------------|-------------------|-------------------------|
| 3-hr Exposure | | | | | | | |
| 15 | 5,876 | 2.895 | 2.34 | 1.424 | 1.298 | 1.544 | 99.7 |
| 21 | 329 | 1.617 | 3.17 | 1.248 | 1.376 | 1.349 | 92.6 |
| 29 | 4,764 | 2.573 | 2.72 | 1.369 | 1.384 | 1.993 | 99.0 |
| 36 | 1,002 | 1.924 | 2.45 | 1.305 | 1.296 | 1.841 | 94.7 |
| 62 | 4,714 | 2.106 | 2.59 | 1.265 | 1.350 | 1.459 | 89.4 |
| 6-hr Exposure | | | | | | | |
| 5 | 2,632 | 2.093 | 1.94 | 1.352 | 1.446 | 1.569 | 97.8 |
| 6 | 3,492 | 2.325 | 2.37 | 1.373 | 1.488 | 1.577 | 97.6 |
| 12 | 5,298 | 1.979 | 2.02 | 1.427 | 1.412 | 1.529 | 99.8 |
| 14 | 1,936 | 2.127 | 1.84 | 1.341 | 1.480 | 1.519 | 95.0 |
| 20 | 2,799 | 2.003 | 2.04 | 1.552 | 1.550 | 1.605 | 99.9 |
| 37 | 3,898 | 2.221 | 2.27 | 1.424 | 1.528 | 1.543 | 99.5 |
| 41 | 4,132 | 2.641 | 2.25 | 1.539 | 1.443 | 1.653 | 99.98 |
| 42 | 3,243 | 2.732 | 2.48 | 1.515 | 1.522 | 1.728 | 99.7 |
| 58 | 2,936 | 2.769 | 2.71 | 1.473 | 1.486 | 1.747 | 99.6 |
| 59 | 2,936 | 2.013 | 2.11 | 1.338 | 1.450 | 1.568 | 93.4 |

Table 19: Batch B 1.5-hr Exposure Critical Notch ROI Correlations (WLI Median Filter)

| Specimen | Total ROIs | Critical ROI K_t | Critical Meas. K_t | Critical ROI K_{fc} | Plate Test K_{fc} | Max. ROI K_{fc} | Critical ROI K_{fc} % |
|----------|------------|--------------------|----------------------|-----------------------|---------------------|-------------------|-------------------------|
| 544-9C | 547 | 1.791 | 2.04 | 1.298 | 1.453 | 1.368 | 94.1 |
| 545-3D | 306 | 1.410 | 2.03 | 1.220 | 1.332 | 1.472 | 60.1 |
| 547-26A | 548 | 1.373 | 1.50 | 1.270 | 1.410 | 1.633 | 87.0 |
| 545-2A | 493 | 1.170 | 2.16 | 1.142 | 1.417 | 1.391 | 6.3 |
| 547-50B | 251 | 1.264 | 2.07 | 1.184 | 1.269 | 1.414 | 30.3 |
| 614-7 | 517 | 1.400 | 2.01 | 1.236 | 1.302 | 1.344 | 70.1 |
| 614-11 | 875 | 1.384 | 1.90 | 1.329 | 1.314 | 1.384 | 97.6 |

Table 20: Batch B 3-hr Exposure Critical Notch ROI Correlations (WLI Median Filter)

| Specimen | Total ROIs | Critical ROI K_t | Critical Meas. K_t | Critical ROI K_{fc} | Plate Test K_{fc} | Max. ROI K_{fc} | Critical ROI K_{fc} % |
|----------|------------|--------------------|----------------------|-----------------------|---------------------|-------------------|-------------------------|
| 545-6A | 1,700 | 1.502 | 1.86 | 1.389 | 1.372 | 1.488 | 98.5 |
| 545-10D | 1,809 | 1.222 | 2.19 | 1.209 | 1.565 | 1.641 | 29.0 |
| 547-22C | 2,691 | 1.356 | 1.98 | 1.265 | 1.471 | 1.876 | 62.0 |
| 547-37B | 2,243 | 1.461 | 1.88 | 1.326 | 1.443 | 1.481 | 92.3 |
| 547-9M | 1,748 | 2.121 | 1.82 | 1.294 | 1.393 | 1.622 | 80.8 |
| 547-5A | 1,584 | 2.054 | 2.83 | 1.248 | 1.392 | 1.556 | 61.2 |

| | | | | | | | |
|---------|-------|-------|------|-------|-------|-------|------|
| 547-23B | 2,180 | 1.309 | 2.67 | 1.203 | 1.517 | 1.814 | 26.7 |
| 544-5C | 1,405 | 1.512 | 2.21 | 1.263 | 1.441 | 1.475 | 73.9 |
| 614-4 | 1,933 | 1.437 | 2.11 | 1.275 | 1.390 | 1.686 | 75.4 |
| 614-12 | 2,365 | 1.179 | 1.01 | 1.153 | 1.391 | 1.708 | 8.4 |
| 614-21 | 2,086 | 1.244 | 1.80 | 1.228 | 1.349 | 1.765 | 45.8 |
| 614-1 | 2,225 | 1.430 | 1.98 | 1.315 | 1.389 | 1.630 | 91.3 |
| 614-15 | 1,739 | 1.266 | 1.82 | 1.242 | 1.342 | 1.519 | 60.0 |

Table 21: Batch B 6-hr Exposure Critical Notch ROI Correlations (WLI Median Filter)

| Specimen | Total ROIs | Critical ROI K_t | Critical Meas. K_t | Critical ROI K_{fc} | Plate Test K_{fc} | Max. ROI K_{fc} | Critical ROI K_{fc} % |
|----------|------------|--------------------|----------------------|-----------------------|---------------------|-------------------|-------------------------|
| 544-8C | 2,777 | 1.592 | 2.16 | 1.517 | 1.583 | 2.030 | 96.9 |
| 544-10C | 3,674 | 1.449 | 1.88 | 1.321 | 1.550 | 2.443 | 70.9 |
| 547-6A | 3,706 | 1.317 | 1.72 | 1.299 | 1.481 | 2.020 | 63.9 |
| 547-20B | 2,839 | 1.306 | 2.24 | 1.286 | 1.477 | 2.152 | 55.1 |
| 547-36B | 3,777 | 1.309 | 3.81 | 1.296 | 1.574 | 1.981 | 61.4 |
| 544-3B | 3,459 | 3.002 | 1.99 | 2.126 | 1.744 | 4.724 | 97.2 |
| 547-16B | 2,933 | 1.339 | 1.92 | 1.322 | 1.549 | 2.504 | 70.6 |
| 547-2C | 3,484 | 1.174 | 1.91 | 1.171 | 1.462 | 2.444 | 11.1 |
| 547-31B | 3,065 | 1.154 | 2.10 | 1.151 | 1.462 | 2.292 | 6.7 |
| 614-3 | 4,182 | 1.422 | 2.23 | 1.368 | 1.417 | 2.296 | 87.6 |
| 614-8 | 4,548 | 1.368 | 1.83 | 1.336 | 1.485 | 2.087 | 77.5 |
| 614-13 | 4,655 | 1.290 | 1.77 | 1.279 | 1.545 | 2.176 | 55.5 |
| 614-5 | 4,109 | 1.481 | 1.90 | 1.413 | 1.512 | 2.516 | 91.6 |
| 614-6 | 4,291 | 1.161 | 2.79 | 1.159 | 1.621 | 2.094 | 9.2 |
| 614-19 | 4,668 | 1.330 | 1.64 | 1.304 | 1.489 | 2.253 | 72.0 |

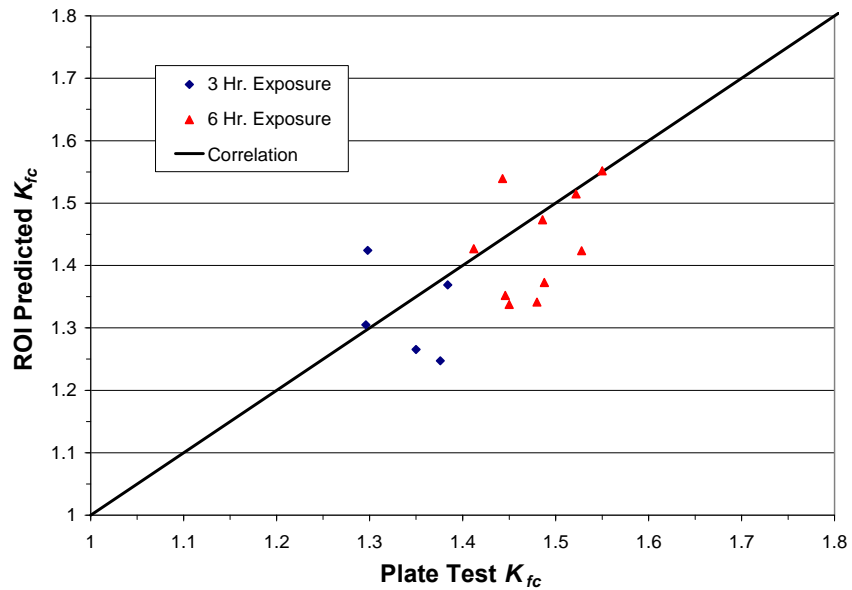


Figure 37: Batch A Critical Notch ROI Correlation (WLI Median Filter)

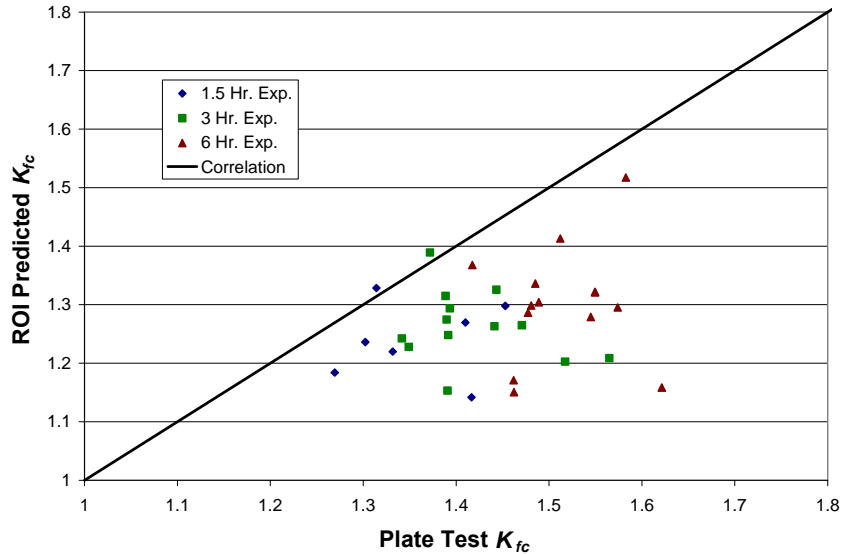


Figure 38: Batch A Critical Notch ROI Correlation (WLI Median Filter)

The K_{fc} comparisons show reasonable correlation for the Batch A samples, but the ROI predicted values are nonconservative compared to the test values on the Batch B set. This result has been traced back to the WLI median filter used to smooth out the effects of individual bad image pixels on the K_t map and the ROI algorithm. The filter also smoothed the height values for the pixels inside the ROIs, with the result that the predicted notch K_t values were reduced from what they should have been because of less measured depth from the WLI image. ROI notch depth analyses were also performed on all of the test specimens using a nonmedian filtered WLI image for comparison. These results are shown in figures 39 and 40, and identify the same ROI areas from the median filtered K_t maps that were used previously.

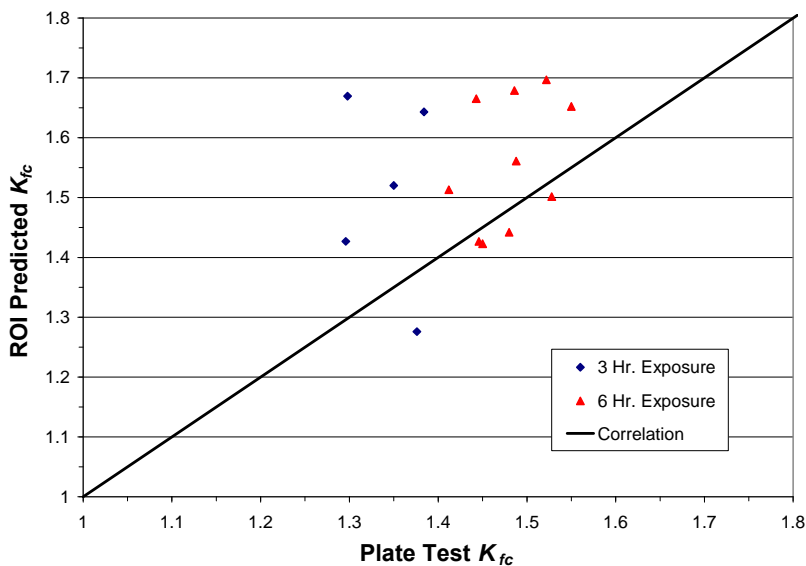


Figure 39: Batch A Critical Notch ROI Correlation (No WLI Median Filter)

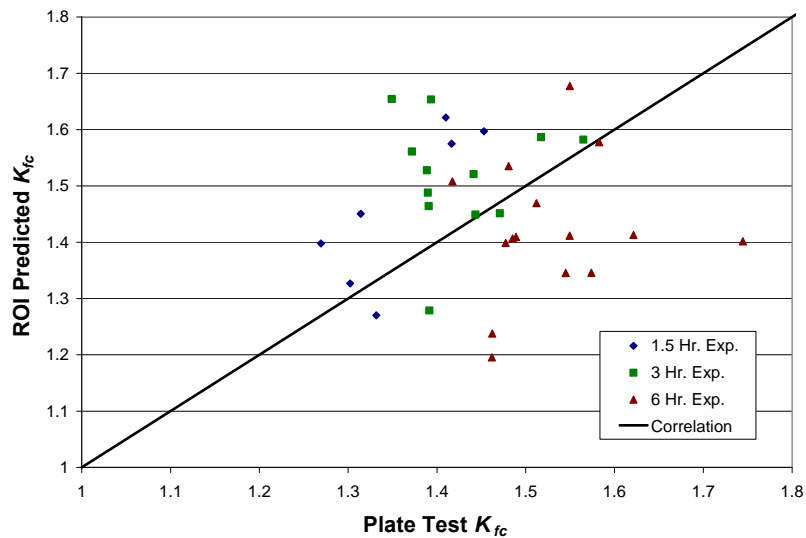


Figure 40: Batch B Critical Notch ROI Correlation (No WLI Median Filter)

Using the nonmedian filtered WLI images to extract notch depths eliminated the bias in the predicted K_{fc} values for the Batch B set, but introduced a conservative bias in the Batch A predicted values. An additional problem was that the nonmedian filtered maximum K_{fc} values for each ROI set were, in most cases, much higher than the critical K_{fc} values. This was the result of the ROI notch depth search algorithm picking out individual bad pixels in or near the ROI area, and using those to estimate notch depth. The large notch depth values resulting from these errors gave very large K_t values, which in turn gave the large K_{fc} values. These unrealistically large K_{fc} values cause grossly conservative life predictions to be made using the ROI results, because the predicted life is sensitive to the largest K_{fc} values in the ROI set. Therefore, only the WLI median filtered results were subsequently used for life predictions.

Another measure of the ability of the ROI algorithm to find the critical corrosion notch is to compare the percentile of the ROI predicted critical K_{fc} value over all of the ROIs identified. These values are listed in the last column of tables 18 through 21. For the Batch A specimens, the predicted critical K_{fc} values are above the 90th percentile for all but one of the specimens. The Batch B specimens show a much wider range of variation, with some values below the bottom 10th percentile. These results show that the Batch B ROI algorithm is identifying a large number of high K_t features that are not fatigue critical, and that many of these features have K_{fc} values that are larger than the critical ROI. Some of these features may be real, and some were caused by dirt or dust on the surface of the specimen while it was being WLI scanned. The fact that the Batch A ROI algorithm is much less sensitive to nonfatigue critical features indicates that the issue is related to the smaller critical notch sizes and lower K_t search thresholds of the Batch B set. Use of higher WLI scan resolution on lightly corroded specimens may reduce this problem in the future.

UNCORRODED CORROSION-FATIGUE PLATE PROBABILISTIC LIFE PREDICTION

Probabilistic crack initiation life predictions were made for the baseline uncorroded AF1410 Batch A and Batch B C-F specimens using the test constant-amplitude marker block load history, for a range of peak stress levels. These results are shown in figure 41 for Batch A plates and in figure 42 for Batch B plates. The predictions are nonconservative in most cases due to the presence of large grit-blast notches on Batch A plates and large surface grinding notches on Batch B plates, which initiated the critical fatigue cracks on the uncorroded specimens. The effect on life of these surface defects cannot easily be predicted from smooth coupon data, since these flaws were not present on the strain-life test coupons. However, the uncorroded life predictions do a reasonable job of approximating the scatter in the uncorroded test results.

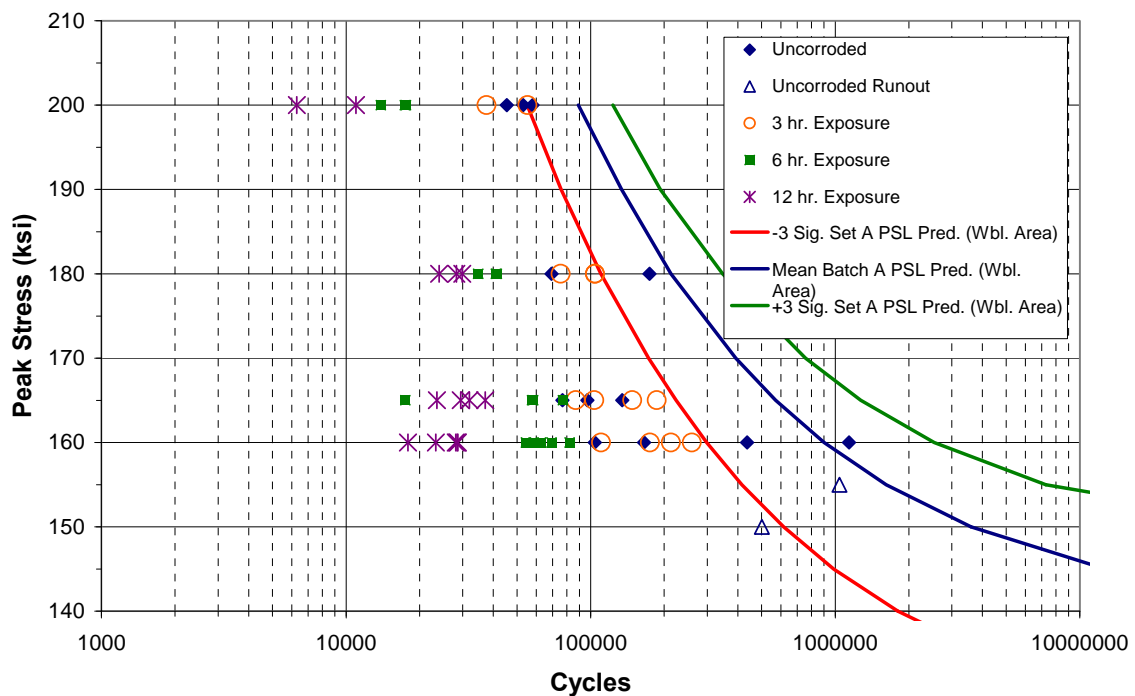


Figure 41: AF1410 Batch A C-F Specimens, Crack Initiation Life

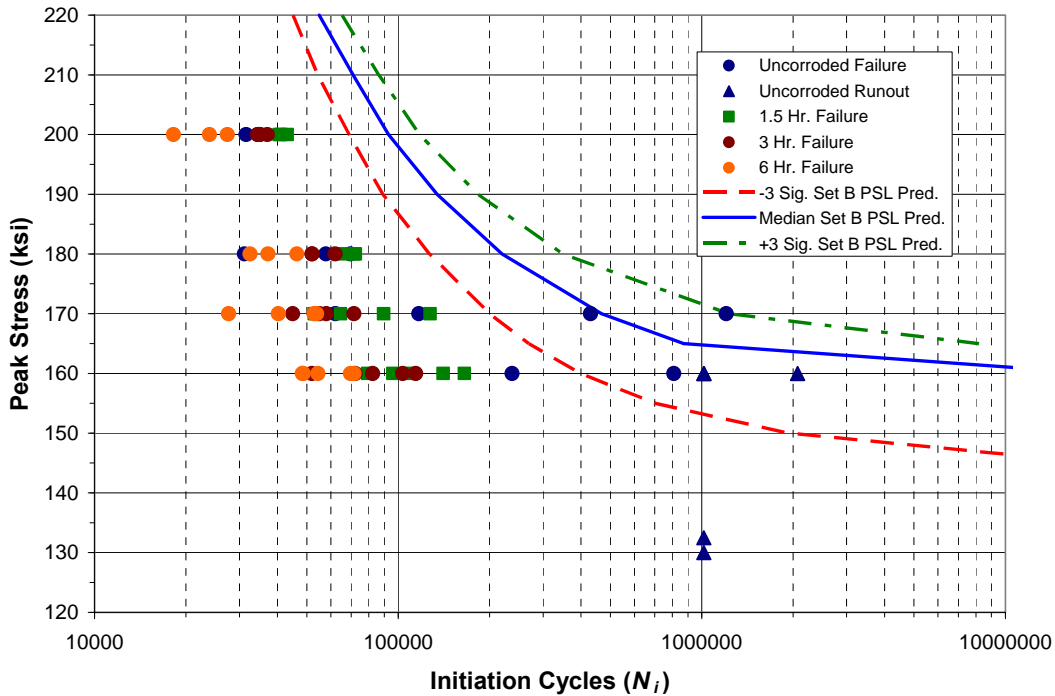


Figure 42: AF1410 Batch B C-F Specimens, Crack Initiation Life

EQUIVALENT STRESS RISER CORROSION-FATIGUE LIFE PREDICTIONS

To check the ability of the ESR method to predict the life of corrosion damaged components, life predictions were made on all of the AF1410 Batch A and Batch B C-F test specimens. Since these were the same test results that were used to calibrate the model, the predictions should give a good indication of the level of conservatism and solution scatter that is to be expected from the approach. All predictions used the WLI median filtered ROI analysis results, with 20 K_{fc} histogram bins. Median (50% probability) life predictions are listed in tables 22 through 25, and are compared to the crack initiation test lives for both test data sets.

Table 22: Batch A ESR Predicted versus Test Lives

| Specimen | Max. ROI K_{fc} | ESR Pred. Median Life (cycles) | Test CI Life (cycles) | Test/Pred. Life Ratio |
|---------------|-------------------|--------------------------------|-----------------------|-----------------------|
| 3-hr Exposure | | | | |
| 15 | 1.544 | 31,494 | 75,508 | 2.398 |
| 21 | 1.349 | 79,398 | 110,336 | 1.390 |
| 29 | 1.993 | 17,698 | 86,987 | 4.915 |
| 36 | 1.479 | 62,157 | 175,012 | 2.816 |
| 62 | 1.459 | 48,325 | 103,595 | 2.144 |
| 6-hr Exposure | | | | |
| 5 | 1.569 | 51,664 | 82,133 | 1.590 |
| 6 | 1.577 | 41,057 | 57,671 | 1.405 |

| | | | | |
|----|-------|--------|--------|-------|
| 12 | 1.529 | 45,043 | 76,999 | 1.709 |
| 14 | 1.519 | 45,245 | 58,261 | 1.288 |
| 20 | 1.605 | 44,798 | 54,375 | 1.214 |
| 37 | 1.543 | 34,502 | 34,688 | 1.005 |
| 41 | 1.653 | 28,239 | 41,316 | 1.463 |
| 42 | 1.728 | 37,213 | 58,514 | 1.572 |
| 58 | 1.747 | 34,537 | 69,243 | 2.005 |
| 59 | 1.568 | 31,155 | 41,029 | 1.317 |

Table 23: Batch B 1.5-hr Exposure ESR Predicted versus Test Lives

| Specimen | Max. ROI K_{fc} | ESR Pred. Median Life (cycles) | Test CI Life (cycles) | Test/Pred. Life Ratio |
|----------|-------------------|-----------------------------------|--------------------------|-----------------------|
| 544-9C | 1.368 | 71,732 | 79,374 | 1.107 |
| 545-3D | 1.472 | 65,395 | 140,711 | 2.152 |
| 547-26A | 1.633 | 45,041 | 96,069 | 2.133 |
| 545-2A | 1.391 | 54,500 | 64,581 | 1.185 |
| 547-50B | 1.414 | 57,706 | 127,432 | 2.208 |
| 614-7 | 1.344 | 34,400 | 41,141 | 1.196 |
| 614-11 | 1.384 | 31,100 | 40,591 | 1.305 |

Table 24: Batch B 3-hr Exposure ESR Predicted versus Test Lives

| Specimen | Max. ROI K_{fc} | ESR Pred. Median Life (cycles) | Test CI Life (cycles) | Test/Pred. Life Ratio |
|----------|-------------------|-----------------------------------|--------------------------|-----------------------|
| 545-6A | 1.488 | 54,487 | 114,168 | 2.095 |
| 545-10D | 1.641 | 45,220 | 51,988 | 1.150 |
| 547-22C | 1.876 | 28,099 | 72,125 | 2.567 |
| 547-37B | 1.481 | 54,474 | 82,424 | 1.513 |
| 547-9M | 1.622 | 45,220 | 103,392 | 2.286 |
| 547-5A | 1.556 | 38,024 | 71,468 | 1.880 |
| 547-23B | 1.814 | 23,764 | 44,960 | 1.892 |
| 544-5C | 1.475 | 45,220 | 57,903 | 1.280 |
| 614-4 | 1.686 | 24,014 | 52,069 | 2.168 |
| 614-12 | 1.708 | 23,764 | 52,009 | 2.189 |
| 614-21 | 1.765 | 20,574 | 62,035 | 3.015 |
| 614-1 | 1.630 | 17,886 | 34,403 | 1.923 |
| 614-15 | 1.519 | 24,014 | 37,046 | 1.543 |

Table 25: Batch B 6-hr Exposure ESR Predicted versus Test Lives

| Specimen | Max. ROI K_{fc} | Full MB Spectrum | | | R = 0.1 Cycles Only | | |
|----------|-------------------|-----------------------------------|--------------------------|-----------------------|-----------------------------------|--------------------------|-----------------------|
| | | ESR Pred. Median Life (cycles) | Test CI Life (cycles) | Test/Pred. Life Ratio | ESR Pred. Median Life (cycles) | Test CI Life (cycles) | Test/Pred. Life Ratio |
| 544-8C | 2.030 | 20,014 | 48,289 | 2.413 | 6,190 | 14,537 | 2.348 |
| 544-10C | 2.443 | 6,612 | 54,416 | 8.230 | 2,548 | 16,192 | 6.355 |
| 547-6A | 2.020 | 19,945 | 69,676 | 3.493 | 6,121 | 20,876 | 3.411 |
| 547-20B | 2.152 | 13,850 | 71,566 | 5.167 | 4,498 | 21,142 | 4.700 |

| | | | | | | | |
|---------|-------|--------|--------|--------|-------|--------|--------|
| 547-36B | 1.981 | 20,208 | 48,724 | 2.411 | 6,384 | 14,972 | 2.345 |
| 544-3B | 4.724 | 6,722 | 27,634 | 4.111 | 2,658 | 8,114 | 3.053 |
| 547-16B | 2.504 | 3,281 | 40,276 | 12.276 | 1,657 | 12,000 | 7.242 |
| 547-2C | 2.444 | 3,481 | 53,899 | 15.484 | 1,857 | 16,000 | 8.616 |
| 547-31B | 2.292 | 6,656 | 52,833 | 7.938 | 2,592 | 16,000 | 6.172 |
| 614-3 | 2.296 | 3,400 | 46,378 | 13.641 | 1,776 | 14,000 | 7.883 |
| 614-8 | 2.087 | 9,200 | 37,236 | 4.047 | 3,000 | 11,212 | 3.737 |
| 614-13 | 2.176 | 6,500 | 32,523 | 5.004 | 2,436 | 10,000 | 4.105 |
| 614-5 | 2.516 | 545 | 23,913 | 43.877 | 545 | 7,649 | 14.035 |
| 614-6 | 2.094 | 3,230 | 18,178 | 5.628 | 1,606 | 5,978 | 3.722 |
| 614-19 | 2.253 | 2,900 | 27,389 | 9.444 | 1,276 | 8,000 | 6.270 |

For the Batch A set, all of the test-to-predicted life ratios range from 1.0 to 2.8, except for specimen 29. Examination of the WLI and ROI data for this specimen indicated that an area of significant grit blast surface damage existed outside the corrosion patch, but was inside the WLI scan area. This surface damage did not cause any cracking in the fatigue test, but generated a large number of ROIs with K_t values greater than 3.0, resulting in a test-to-predicted life ratio for this specimen of 4.9. This type of severe grit blast damage was not observed on any of the other Batch A test specimens, so the conservatism of this life prediction is considered to be nonrepresentative. A related issue occurred in the analysis of specimen 36, where surface dirt and dust outside the corrosion patch was present during WLI scanning, causing discontinuities in the stress contours that were picked up by the ROI analysis. The largest three ROI K_{fc} values in the analysis were caused by such contamination, resulting in a test-to-predicted life ratio of 5.7. Removal of these three ROIs resulted in a recalculated test-to-predicted life ratio of 2.82, which is shown in table 22.

For the Batch B set, all of the test-to-predicted life ratios range from 1.0 to 3.0, except for the 6-hr exposures. Much larger test-to-predicted life ratios are present in this set, and are a result of the maximum ROI K_{fc} values being near or above 2.0. The cause of this was traced to the ROI notch depth extraction procedure. For ROIs with K_t values just above the ROI filtering threshold and that are located in large surface depression areas, there is little to no net change in surface height between the pixels inside and immediately outside the ROI area boundary. The notch depth extraction algorithm measures the ROI maximum depth relative to a set of reference points located outside the corrosion patch, which in effect gives the relative depth of the large surface depression area at the ROI location because there is no sharp notch edge boundary at the ROI boundary. The large notch depth measurement then causes the notch metric equation to overpredict the K_t value associated with the notch, which results in an overly conservative K_{fc} value. The 6-hr exposure specimens are the most susceptible to this effect because of the greater amounts of corrosion present compared to the 1.5- and 3-hr exposures. Many of these ROIs could be eliminated by increasing the K_t filtering threshold for the 6-hr exposure specimens. However, it was elected to keep the filtering threshold the same for all exposure levels of the Batch B set for comparison purposes. Overconservative maximum ROI K_{fc} values do not seem to have a major effect on the Batch A prediction results, likely because of the higher ROI K_t filtering threshold used. These issues with the depth extraction algorithm may also help explain

the large amount of scatter in the Batch B critical ROI K_{fc} % values shown in tables 19, 20, and 21, as compared to the Batch A set.

For median life predictions less than 20,000 cycles, the presence of a large number of $R = 0.7$ delay cycles in the marker block load history has the effect of skewing the apparent conservatism of the prediction. This can be seen in the Batch B 6-hr exposure results of table 25, where some of the test-to-predicted life ratios are above 10.0. Subtracting the $R = 0.7$ delay cycles from the load histories of the experimental and predicted results, as shown in the last three columns of table 25, gives a more representative assessment of the conservatism of the short life predictions. Removing the $R = 0.7$ cycles from the results analysis is considered acceptable in this case, because it is the $R = 0.1$ cycles that cause most of the crack initiation damage.

LIFE PREDICTION UNCERTAINTY FROM THE EQUIVALENT STRESS RISER MODEL

Because of the large number of random variable input parameters (20) in the ESR model, Monte Carlo sampling was used to generate random parameter values for life predictions. Two methods of propagating uncertainty in the ROI notch dimension measurements were used. In the first, the error is assumed to be 100% correlated, so each notch dimension for all ROIs will have the same error. This correlation is necessary to support sensitivity analysis of the input parameters, as having uncorrelated notch dimension errors for each ROI would result in an extremely large number of independent variable inputs when all ROIs are accounted for. The second propagation method is to assume that the ROI measurement errors are uncorrelated for each individual ROI. Monte Carlo uncertainty predictions were made on a single Batch A 3-hr exposure specimen, for 50 random sample sets. CDF results were reduced to a median predicted life for each random sample, over a CDF range of 1,000 to 100,000 cycles. For the fully correlated notch dimension error, the set of median predicted lives most closely approximates a normal distribution. For the uncorrelated notch dimension error, the distribution type is unknown because 13 of the 50 samples had median values below the 1,000 cycle lower bound of the CDF range. For this case, the histogram of the median predicted values is concentrated at the lower end of the CDF range. Sample means and standard deviations of the median life predictions for the two cases are listed in table 26, along with the life to crack initiation for the test specimen.

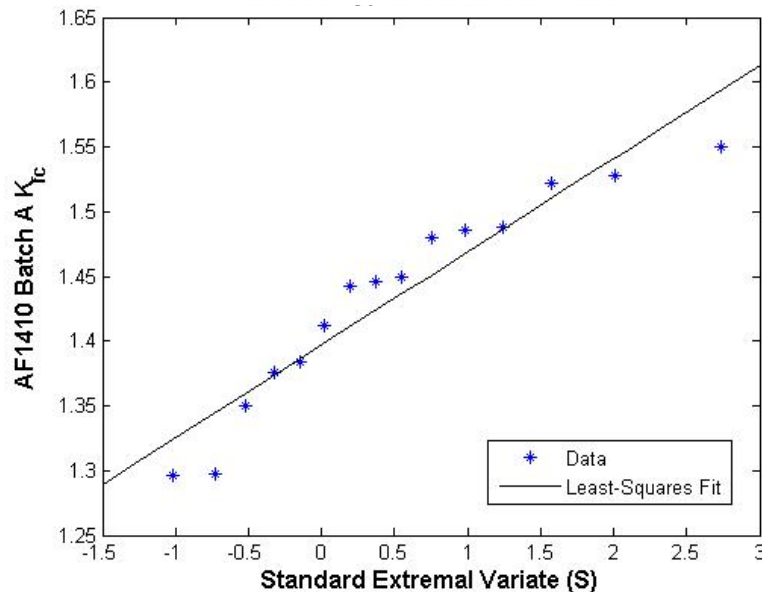
Table 26: Uncertainty in Median Predicted Life of Specimen 62 for Two Error Correlation Assumptions

| Prediction Case | Mean | Standard Deviation |
|------------------------------------|----------------|--------------------|
| Correlated Notch Dimension Error | 54,355 cycles | 10,350 cycles |
| Uncorrelated Notch Dimension Error | 17,081 cycles | 17,360 cycles |
| Specimen 62 Test | 103,595 cycles | - |

For the correlated notch dimension error case, confidence bounds can be estimated based on the normal distribution assumption for the median life prediction. For a two-sided 95% confidence interval, the bounds on the median life prediction were $\pm 2,870$ cycles. Using the lower 95% confidence bound, the median test to predicted life ratio for the fully correlated specimen 62 prediction is 2.012. No confidence bounds were generated for the uncorrelated notch dimension error case because the underlying distribution type was unknown.

EQUIVALENT STRESS RISER MODEL PREDICTION USING EXTREME VALUE STATISTICS

As a check on the validity of the extreme value assumption of K_{fc} values, the median test K_{fc} values for each batch of C-F plates were plotted on Type I Extreme Value probability plots. Only plates that cracked from corrosion notches were included in the data sets. Only 3- and 6-hr exposure sets were included in the Batch A data (figure 43). All three exposure levels were included in the Batch B data (figure 44). The plots show that the test K_{fc} values are a good fit to the extreme value assumption, especially for the Batch B test data.

Figure 43: Gumbel Type I Extreme Value Fit for Median Batch A K_{fc} Test Values

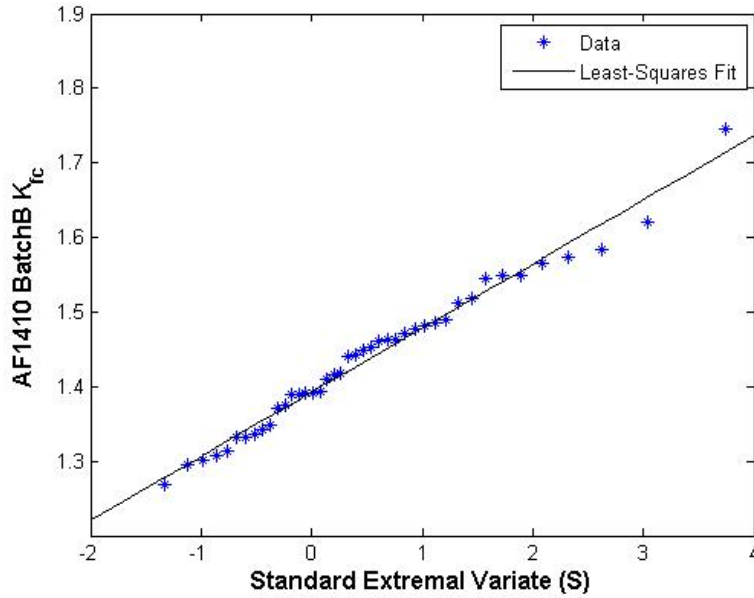


Figure 44: Gumbel Type I Extreme Value Fit for Median Batch B K_{fc} Test Values

Predictions were made for some of the AF1410 Set A C-F test specimens (42, 5, 6, 51, and 62) that were not included in the extreme value calibration set described previously. Figures 45 through 49 show the results of these predictions where the vertical line indicates the actual K_{fc} value found in the experiment.

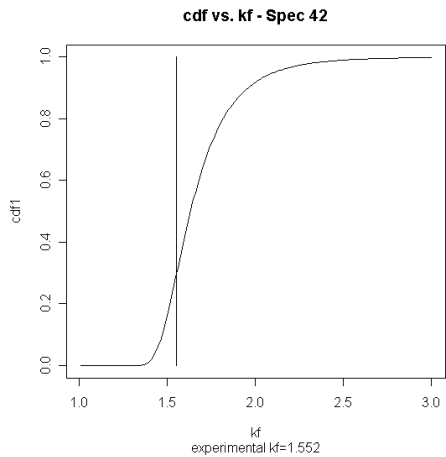


Figure 45: Extreme Value ESR Model Prediction and Experimental K_{fc} for AF1410 Batch A, Specimen 42

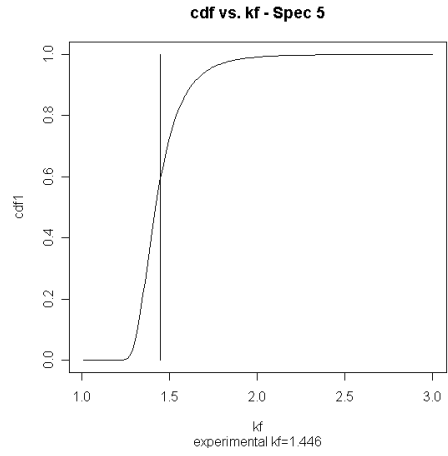


Figure 46: Extreme Value ESR Model Prediction and Experimental K_{fc} for AF1410 Batch A, Specimen 5

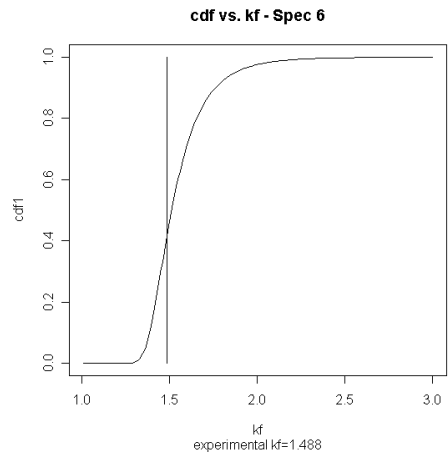


Figure 47: Extreme Value ESR Model Prediction and Experimental K_{fc} for AF1410 Batch A, Specimen 6

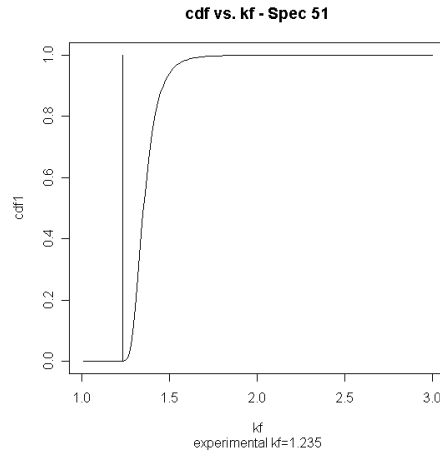


Figure 48: Extreme Value ESR Model Prediction and Experimental K_{fc} for AF1410 Batch A, Specimen 51

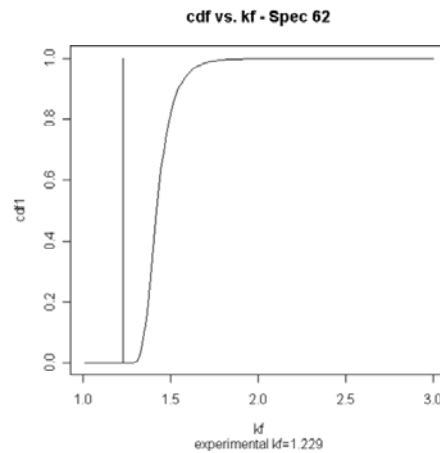


Figure 49: Extreme Value ESR Model Prediction and Experimental K_{fc} for AF1410 Batch A, Specimen 62

Calculations to compare predicted-to-test lives in terms of cycles-to-crack initiation for the extreme value calibrated model were not performed. Additional comparisons and model investigations were not performed due to program schedule constraints.

MICROMACHINED SPECIMEN LIFE PREDICTION

The micromachined specimen life predictions for the nominal Peterson model and the first Peterson Beta prediction are deterministic, and use the same ESR algorithms that were developed for the C-F modeling. The Monte Carlo simulation algorithm used for the second Peterson Beta model prediction will not work for spectrum load blocks with nonconstant damage accumulation. For the constant-amplitude marker cycle spectrum block used in the

micromachined specimen tests, the $R = 0.1$ load cycles result in an equivalent fatigue damage rate that is about five times greater than the $R = 0.7$ load cycles. Therefore, the life predictions shown here only represent the damage accumulated from $R = 0.1$ cycles, with the $R = 0.7$ cycles ignored. When comparing test results to the life predictions, all of the $R = 0.7$ cycles must be eliminated from the final cycle count to crack initiation for each test. Table 27 shows these results for $R = 0.1$ cycles and total cycles. All of the notched specimens cracked from both conic frustum features. Fractographic results for life to crack initiation are shown for both features, with the primary feature being the one that reached a 0.010 in. deep crack first.

Table 27: Crack Initiation Test Lives for Micromachined Specimens

| Specimen | Surface | Primary Conic | | Secondary Conic | |
|----------|-----------|-------------------|-----------------|-------------------|-----------------|
| | | R = 0.1 Cycles | Total Cycles | R = 0.1 Cycles | Total Cycles |
| 598-4 | Unnotched | 25,467 | 83,467 | - | - |
| 598-11 | Unnotched | 24,212 | 80,212 | - | - |
| 598-14 | Unnotched | 14,974 | 49,374 | - | - |
| 598-1 | Notched | 1,767 | 6,567 | 1,800 | 6,600 |
| 598-2 | Notched | 1,700 | 3,300 | 1,822 | 5,822 |
| 598-3 | Notched | 1,968 | 4,368 | 1,971 | 4,371 |
| 598-5 | Notched | 1,521 | 5,760 | 1,934 | 6,173 |
| 598-8 | Notched | 1,418 | 4,209 | 1,869 | 4,660 |
| 598-9 | Notched | 1,828 | 5,700 | 1,936 | 5,808 |
| 598-10 | Notched | 1,500 | 3,100 | 1,833 | 3,433 |
| 598-12 | Notched | 1,483 | 4,633 | 1,550 | 4,700 |
| 598-13 | Notched | 1,790 | 6,502 | 1,970 | 6,682 |

The overall predicted life to crack initiation for micromachined plates tested at 200 ksi peak stress is shown below for the two model versions:

Peterson nominal – $P_f \cong 50\%$ at 1,040 cycles ($R = 0.1$)

Peterson Beta – $P_f \cong 50\%$ at 2,224 cycles ($R = 0.1$)

Peterson Beta 2 – $P_f \cong 50\%$ at $1,688 \pm 85$ cycles for 95% confidence level ($R = 0.1$)

Note that the confidence bounds for the Peterson Beta 2 distribution are only for the Monte Carlo sample size of the solution, and do not include the contributions from the model parameter uncertainties. A plot of failure probability CDFs for the two predictions is shown in figure 50. The final Monte Carlo sample size for the Peterson Beta prediction was 10,000, so the CDF should be reasonably accurate for P_i values between 0.001 and 0.999.

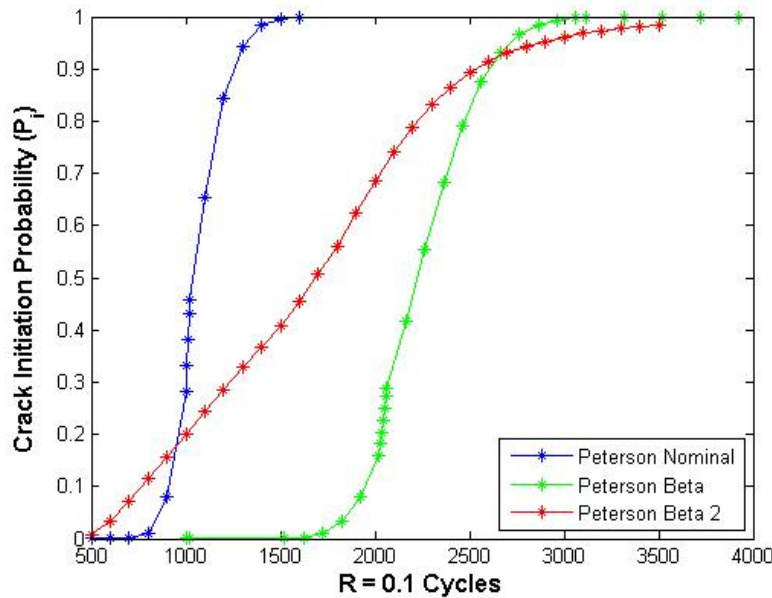


Figure 50: CDF of Micromachined Plate Crack Initiation Probabilities for Two ESR Model Versions

Probability plots of the rank-order statistic output for each prediction showed that the CDF curves most closely approximate a lognormal distribution, with the parameter values for each distribution listed in table 28. Also listed is the lognormal parameter fit to the overall plate test results, including the 95% confidence bounds on the estimates.

Table 28: Lognormal Distribution Parameters for Micromachined Specimen Predictions and Test Results (95% Confidence Bounds)

| Prediction Type | Log-Life Mean | Log-Life S.D. |
|--------------------|---------------|------------------------|
| Peterson | 6.972 | 0.125 |
| Peterson Beta | 7.711 | 0.113 |
| Peterson Beta 2 | 7.299 | 0.435 |
| Plate Test Results | 7.411 ± 0.088 | 0.0769 < 0.114 < 0.218 |

The mean test to predicted life ratio for the Peterson prediction is 1.55, and is 0.74 and 1.12 for the two Peterson Beta predictions, respectively. Tables 29, 30, and 31 show the contribution of each micromachined notch to the overall test specimen crack initiation probability for the three predictions. In the tables, the probabilities listed are for reliability instead of failure. These results enable a direct comparison of prediction versus test life for each individual notch. The overall test specimen reliability CDF values are the product of all the individual notch reliability values for each life cycle value.

Table 29: Individual Notch Reliabilities for Peterson Nominal Model Life Prediction

| R = 0.1 Cycles | Reliability for Notch K_f Values | | | | | |
|----------------|------------------------------------|-------|-------|----------|----------|----------|
| | 1.0 | 1.502 | 1.569 | 1.979 | 2.028 | 2.266 |
| 500 | 1 | 1 | 1 | 1 | 1 | 1 |
| 600 | 1 | 1 | 1 | 1 | 1 | 0.999998 |
| 700 | 1 | 1 | 1 | 1 | 1 | 0.999679 |
| 800 | 1 | 1 | 1 | 1 | 1 | 0.990499 |
| 900 | 1 | 1 | 1 | 1 | 1 | 0.920553 |
| 1,000 | 1 | 1 | 1 | 1 | 1 | 0.717637 |
| 1,008 | 1 | 1 | 1 | 1 | 1 | 0.667616 |
| 1,016 | 1 | 1 | 1 | 1 | 1 | 0.617611 |
| 1,024 | 1 | 1 | 1 | 1 | 0.999999 | 0.568538 |
| 1,024 | 1 | 1 | 1 | 1 | 0.999997 | 0.542749 |
| 1,100 | 1 | 1 | 1 | 0.999999 | 0.999974 | 0.346603 |
| 1,200 | 1 | 1 | 1 | 0.999991 | 0.999732 | 0.156538 |
| 1,300 | 1 | 1 | 1 | 0.999908 | 0.998307 | 0.057289 |
| 1,400 | 1 | 1 | 1 | 0.999409 | 0.992751 | 0.01751 |
| 1,500 | 1 | 1 | 1 | 0.997352 | 0.977197 | 0.004606 |
| 1,600 | 1 | 1 | 1 | 0.991093 | 0.94389 | 0.001072 |

Table 30: Individual Notch Reliabilities for Peterson Beta Model Life Prediction

| R = 0.1 Cycles | Reliability for Notch K_f Values | | | | | |
|----------------|------------------------------------|-------|-------|-------|--------|--------|
| | 1.0 | 1.439 | 1.445 | 1.699 | 1.888 | 1.977 |
| 1,000 | 1 | 1 | 1 | 1 | 1 | 1 |
| 1,024 | 1 | 1 | 1 | 1 | 1 | 1 |
| 1,524 | 1 | 1 | 1 | 1 | 1 | 0.9995 |
| 1,624 | 1 | 1 | 1 | 1 | 1 | 0.9973 |
| 1,724 | 1 | 1 | 1 | 1 | 1 | 0.989 |
| 1,824 | 1 | 1 | 1 | 1 | 1 | 0.9664 |
| 1,924 | 1 | 1 | 1 | 1 | 0.9998 | 0.9194 |
| 2,024 | 1 | 1 | 1 | 1 | 0.9991 | 0.8412 |
| 2,032 | 1 | 1 | 1 | 1 | 0.9987 | 0.8206 |
| 2,040 | 1 | 1 | 1 | 1 | 0.9982 | 0.7992 |
| 2,048 | 1 | 1 | 1 | 1 | 0.9974 | 0.7773 |
| 2,056 | 1 | 1 | 1 | 1 | 0.9965 | 0.755 |
| 2,064 | 1 | 1 | 1 | 1 | 0.9952 | 0.7324 |
| 2,064 | 1 | 1 | 1 | 1 | 0.9943 | 0.7188 |
| 2,164 | 1 | 1 | 1 | 1 | 0.9851 | 0.5996 |
| 2,264 | 1 | 1 | 1 | 1 | 0.9669 | 0.477 |
| 2,364 | 1 | 1 | 1 | 1 | 0.9356 | 0.3623 |
| 2,464 | 1 | 1 | 1 | 1 | 0.8881 | 0.2634 |
| 2,564 | 1 | 1 | 1 | 1 | 0.8233 | 0.1839 |
| 2,664 | 1 | 1 | 1 | 1 | 0.743 | 0.1237 |
| 2,764 | 1 | 1 | 1 | 1 | 0.6515 | 0.0805 |

| | | | | | | |
|-------|---|---|---|--------|--------|--------|
| 2,864 | 1 | 1 | 1 | 1 | 0.5547 | 0.0508 |
| 2,964 | 1 | 1 | 1 | 1 | 0.4586 | 0.0311 |
| 3,064 | 1 | 1 | 1 | 1 | 0.3685 | 0.0186 |
| 3,120 | 1 | 1 | 1 | 0.9997 | 0.2966 | 0.0136 |
| 3,320 | 1 | 1 | 1 | 0.9985 | 0.1776 | 0.0043 |
| 3,520 | 1 | 1 | 1 | 0.9944 | 0.0998 | 0.0012 |
| 3,720 | 1 | 1 | 1 | 0.9837 | 0.0456 | 0.0004 |
| 3,920 | 1 | 1 | 1 | 0.9606 | 0.0196 | 0.0001 |
| 4,120 | 1 | 1 | 1 | 0.9189 | 0.0081 | 0 |

Table 31: Individual Notch Reliabilities for Peterson Beta 2 Model Life Prediction

| R = 0.1 Cycles | Reliability for Notch Average K_f Values | | | | | |
|----------------|--|--------|--------|-------|--------|--------|
| | 1.888 | 1.888 | 1.977 | 1.445 | 1.7 | 1.439 |
| 500 | 1 | 1 | 0.992 | 1 | 1 | 1 |
| 600 | 1 | 1 | 0.9656 | 1 | 1 | 1 |
| 700 | 1 | 1 | 0.9284 | 1 | 0.9996 | 1 |
| 800 | 1 | 1 | 0.8884 | 1 | 0.9972 | 1 |
| 900 | 1 | 1 | 0.8494 | 1 | 0.9928 | 1 |
| 1,000 | 1 | 1 | 0.8104 | 1 | 0.9863 | 1 |
| 1,100 | 1 | 1 | 0.7757 | 1 | 0.9761 | 1 |
| 1,200 | 0.9999 | 1 | 0.7422 | 1 | 0.9653 | 1 |
| 1,300 | 0.9995 | 0.9997 | 0.7079 | 1 | 0.9507 | 1 |
| 1,400 | 0.9983 | 0.9981 | 0.6772 | 1 | 0.936 | 1 |
| 1,500 | 0.9941 | 0.9937 | 0.6481 | 1 | 0.9237 | 1 |
| 1,600 | 0.9823 | 0.9837 | 0.6206 | 1 | 0.9104 | 1 |
| 1,700 | 0.9627 | 0.962 | 0.5956 | 1 | 0.8951 | 1 |
| 1,800 | 0.9354 | 0.931 | 0.5728 | 1 | 0.88 | 1 |
| 1,900 | 0.8895 | 0.8916 | 0.5475 | 1 | 0.865 | 1 |
| 2,000 | 0.8383 | 0.8406 | 0.5262 | 1 | 0.8504 | 1 |
| 2,100 | 0.7887 | 0.7832 | 0.5038 | 1 | 0.8334 | 1 |
| 2,200 | 0.7304 | 0.7282 | 0.4849 | 1 | 0.8173 | 1 |
| 2,300 | 0.6767 | 0.6713 | 0.4644 | 1 | 0.8019 | 1 |
| 2,400 | 0.6222 | 0.6161 | 0.4468 | 1 | 0.7872 | 1 |
| 2,500 | 0.574 | 0.5665 | 0.43 | 1 | 0.7724 | 1 |
| 2,600 | 0.5297 | 0.5218 | 0.4126 | 1 | 0.7598 | 1 |
| 2,700 | 0.4885 | 0.4837 | 0.3959 | 1 | 0.7453 | 1 |
| 2,800 | 0.4537 | 0.4514 | 0.3817 | 1 | 0.7307 | 1 |
| 2,900 | 0.4211 | 0.4201 | 0.3686 | 1 | 0.718 | 1 |
| 3,000 | 0.3936 | 0.3913 | 0.3551 | 1 | 0.7037 | 1 |
| 3,100 | 0.3653 | 0.3648 | 0.3424 | 1 | 0.6914 | 0.9999 |
| 3,200 | 0.3415 | 0.342 | 0.3322 | 1 | 0.6786 | 0.9999 |
| 3,300 | 0.3199 | 0.3206 | 0.3217 | 1 | 0.6638 | 0.9998 |
| 3,400 | 0.3008 | 0.3027 | 0.3094 | 1 | 0.6516 | 0.9998 |
| 3,500 | 0.283 | 0.2854 | 0.3 | 1 | 0.6412 | 0.9991 |

To enable the estimation of parameter uncertainty in the model fit, bootstrap resampling methods were attempted to generate random samples of parameter values for the Peterson Beta model. However, because of the large amount of scatter in the underlying data, the majority of the samples would not converge to a valid maximum likelihood solution. It is therefore not possible to generate life prediction confidence bounds for the existing data set that will adequately incorporate the underlying uncertainty in the model parameters.

EQUIVALENT STRESS RISER LIFE PREDICTION ON CADMIUM-PLATED CORROSION-FATIGUE SPECIMENS

A blind prediction of the crack initiation lives of the corroded, cad-plated C-F specimens was made, without prior knowledge of the fatigue test results. Most of the ROIs on each specimen were located in the masked area outside the corrosion patch, as a result of the surface roughness from grit blasting and plating of the specimens. However, all of the ROIs with the largest K_{fc} values were located in the corroded area where the plating was sanded off. The area between the sanded region and the masking edge was exceptionally smooth compared to the masked areas, indicating that the corrosion smoothed down the cad-plated surface without causing a large amount of corrosion damage. Indications of corrosion damage were only present in the sanded part of the unmasked area. Dirt that was present in most of the WLI scans caused some high K_{fc} value ROIs that were manually removed from the data sets prior to life predictions. Statistics for the ROI analyses are listed in table 32, along with the life predictions as compared to the test results. No attempt was made to develop confidence bounds for the cad-plated life predictions due to program time constraints.

Table 32: ESR Life Prediction Results for Cad-Plated AF1410 C-F Plates

| Specimen | Total ROIs | Critical Meas. K_t | Plate Test K_{fc} | Max. ROI K_{fc} | ESR Pred. Median Life (cycles) | Test CI Life (cycles) | Test/Pred. Life Ratio |
|----------|------------|----------------------|---------------------|-------------------|--------------------------------|-----------------------|-----------------------|
| 545-1C | 2,529 | 2.207 | 1.224 | 1.364 | 55,040 | 151,029 | 2.74 |
| 614-10 | 1,276 | 2.134 | 1.260 | 1.417 | 54,570 | 121,634 | 2.29 |
| 614-14 | 1,519 | 1.874 | 1.223 | 1.432 | 51,780 | 151,403 | 2.92 |
| 614-23 | 878 | 2.321 | 1.226 | 1.434 | 49,430 | 148,596 | 3.01 |

EQUIVALENT STRESS RISER LIFE PREDICTION ON AN F/A-18C/D ARRESTING SHANK SECTION

ESR modeling of stress gradient effects was demonstrated by performing a life prediction on a service corroded F/A-18C/D arresting shank. The arresting shanks experience corrosion in the lateral damper sleeve region, on the inside diameter of the shank. The shanks are subject to pure bending (hook bounce) and combined axial and bending (cable pickup) load cases, with the first principle stress direction in the damper region fixed along the longitudinal axis of the shank (proportional loading). Replicas of the corrosion inside the damper sleeve region were made prior to shank testing. Replicas representing a 110 deg section of the lower portion of the damper sleeve region of shank PT0735 were scanned by WLI to create a surface topology image. Replica and WLI scanning procedures, along with shank test setup

and results are described in reference 27. ESRD generated axial stress contour plots of the damper region inside diameter for both hook bounce and cable pickup load cases. Results for the cable pickup load case are shown in figure 51.

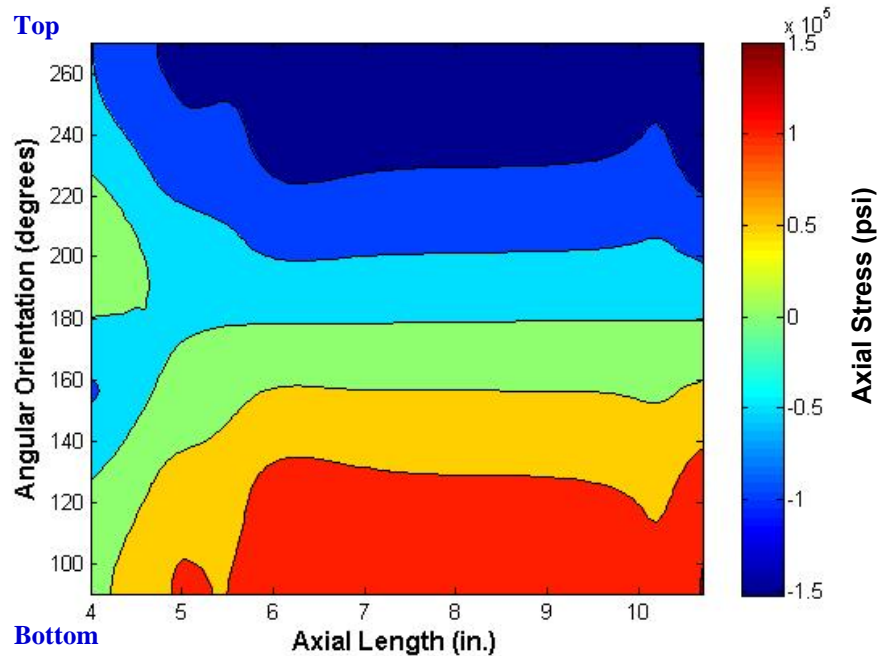


Figure 51: F/A-18C/D Arresting Shank Damper Sleeve Inside Bore Axial Stress Distribution, Cable Pickup Load Case

These contour plots were used to create K_g maps for each load case, based on a reference location 8.0 in. aft of the shank lateral pivot axis, at the bottom of the inside diameter. Using the test load spectrum and the stress contour maps, a stress spectrum was created for the reference location, and used to generate a spectrum strain-life curve for a range of spectrum stress ratios. This curve is shown in figure 52 for three different probability levels, and is based on a reference K_{fc} value of 2.0.

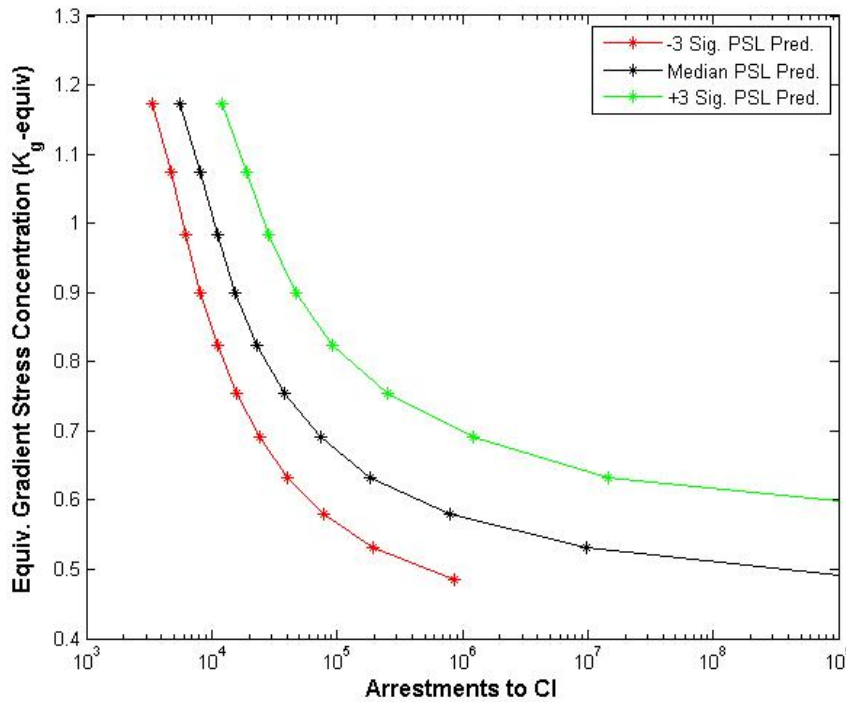


Figure 52: Spectrum Strain-Life Curve for Reference Location, as a Function of Equivalent Gradient Stress Concentration

The $K_{g-equiv}$ values for each local notch were interpolated off the median curve of figure 52 at the predicted local notch life calculated for the reference K_{fc} value. As a check on the accuracy of the $K_{g-equiv}$ local notch life approximation, local notch PSL predictions using the local stress history were compared to PSL predictions made using the $K_{g-equiv}$ values at the reference location. The results are shown in table 33 for a range of $K_{g-equiv}$ values.

Table 33: Comparison of Life Values Predicted at Local Notch with $K_{g-equiv}$ Method Predictions, 2.0 Reference K_{fc} value

| $K_{g-equiv}$ | Local Notch PSL Prediction | | | Reference Location PSL Prediction | | | % Error | |
|---------------|----------------------------|---------|-------------|-----------------------------------|---------|-------------|-------------|-------------|
| | -3 σ | Median | +3 σ | -3 σ | Median | +3 σ | -3 σ | +3 σ |
| 1.085 | 4,594 | 7,847 | 18,180 | 4,594 | 7,847 | 18,170 | 0 | -0.06 |
| 0.979 | 6,375 | 11,360 | 29,380 | 6,371 | 11,360 | 29,430 | -0.06 | 0.003 |
| 0.748 | 16,430 | 40,810 | 290,300 | 16,410 | 40,810 | 293,200 | -0.12 | 1.00 |
| 0.657 | 32,610 | 124,900 | 5.101E6 | 32,270 | 124,900 | 5.164E6 | -1.04 | 1.24 |
| 0.546 | 144,900 | 4.300E6 | Inf. | 144,700 | 4.300E6 | Inf. | -0.14 | 0 |

The comparison shows that the scatter in life distributions is not significantly affected by the $K_{g-equiv}$ approximation, so the amount of error introduced in the life prediction CDF of the entire component should be minimal.

The FFT elasticity solution for the shank WLI image is created as if the corroded surface was subjected to a uniform stress field, with the curvature of the shank bore eliminated by the high-pass WLI Gaussian filter. Notch K_t values are therefore only a function of the notch dimensions. Initial ROI analysis of the shank WLI image generated 5,979 ROIs. Since all shanks are abrasive blasted prior to cadmium plating during manufacture, uniform stress K_{fc} values were calculated using the Batch A C-F calibrated Peterson equation. Peak K_{fc} value for the initial analysis was 9.58, with 13 ROIs having a value greater than 3.0. Examination of some of the high K_{fc} ROIs indicated the presence of a large amount of dust and dirt in the WLI scans of the corrosion replica, as shown in figure 53.

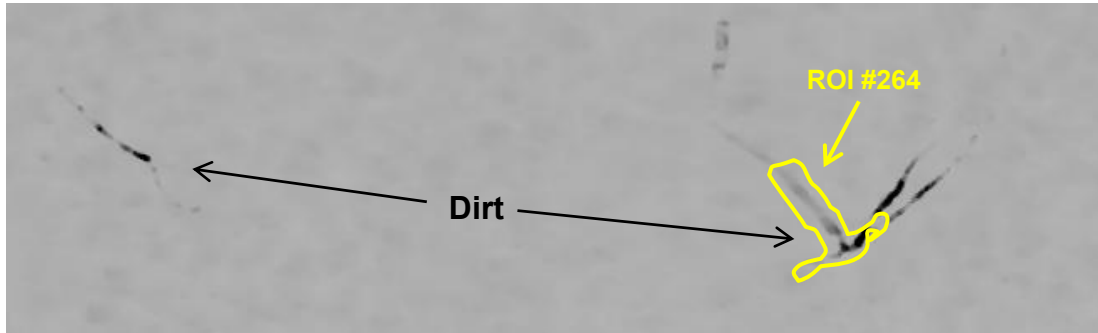


Figure 53: Contamination on Shank PT0735 Replica WLI Scan, Strip 17

Previous methods used to filter out contamination on the C-F plate WLI images were to throw out all pixels approximately $2\ \mu\text{m}$ above the mean reference plane for the uncorroded portions of the surface. However, since the contamination in the shank scans is on the surface of the corrosion replica, the contamination height measurements are in the same direction as the corrosion notches, so all pixels above a threshold value cannot be arbitrarily thrown out. The filtering approach taken for this case was to throw out all ROIs with a width to height ratio greater than 6.0. This resulted in the number of ROIs being reduced to 5927 for the complete image, with a maximum K_{fc} value of 3.956. Performing the shank stress gradient modification to this ROI set gave a maximum K_{fc-eff} value of 3.894. The CDF of crack initiation probability for this ROI set is shown in figure 54, with a median predicted crack initiation life of 359 arrestments. This prediction appeared to be highly conservative, considering that the shank in question was tested to 7,413 arrestments without cracking in the damper sleeve region. Additional analysis of the filtered ROI set found other high K_t ROIs with the appearance of originating from surface contamination, but that were not filtered out by the aspect ratio filter. Six of these ROIs were manually removed from the ROI set to give a total of 5,921 for the complete image, with the same maximum K_{fc} value of 3.956 as in the previous set. Performing the shank stress gradient modification to this ROI set gave a new maximum K_{fc-eff} value of 2.107. The CDF of crack initiation probability for this ROI set is shown in figure 55, with a median predicted crack initiation life of 7,990 arrestments.

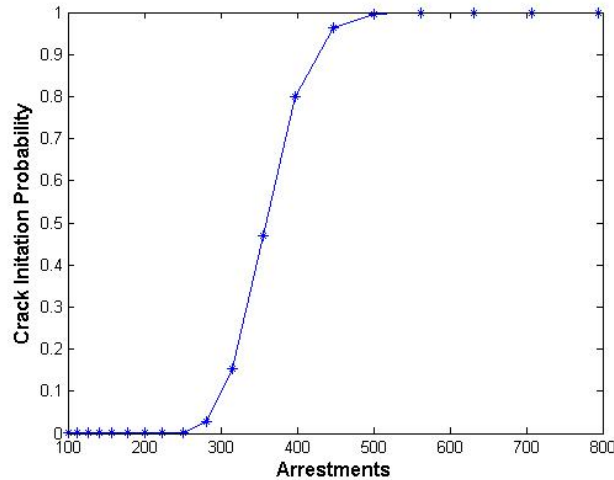


Figure 54: Partial Shank Life Prediction with High K_t Values from Contamination

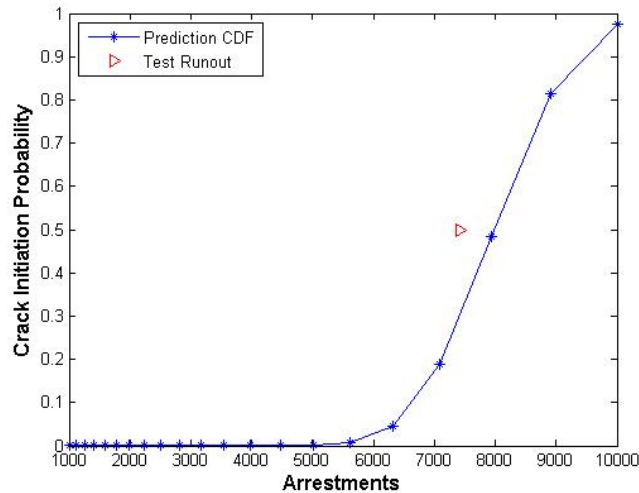


Figure 55: Partial Shank Life Prediction with High K_t Values from Contamination Removed

After fatigue testing, new surface replicas was made from the upper and lower 180 deg sections of the damper region of shank PT0735. WLI scans were made using these replicas, with care taken to minimize the amount of dust and dirt accumulation on the replica surfaces during scanning. A new partial shank life prediction was made using the complete lower 180 deg section WLI scans, with the CDF of crack initiation probability shown in figure 56. The median predicted crack initiation life was 15,240 arrestments. Initial ROI analysis generated 10,654 ROIs, and accounting for stress gradient effects and WLI image strip overlap reduced this number to 2,002. The maximum K_{fc-eff} value for this prediction was 1.761. The largest five K_{fc-eff} values for the set were segregated into individual bins in the K_{fc-eff} histogram, prior to the life prediction calculation. This was done to minimize the histogram discretization error influence on the overall life prediction error. Examination of the WLI

images and resulting ROI details indicated little to no contamination on the replica surfaces. As a result, no additional filtering was applied to these ROI sets, as was done for the previous prediction.

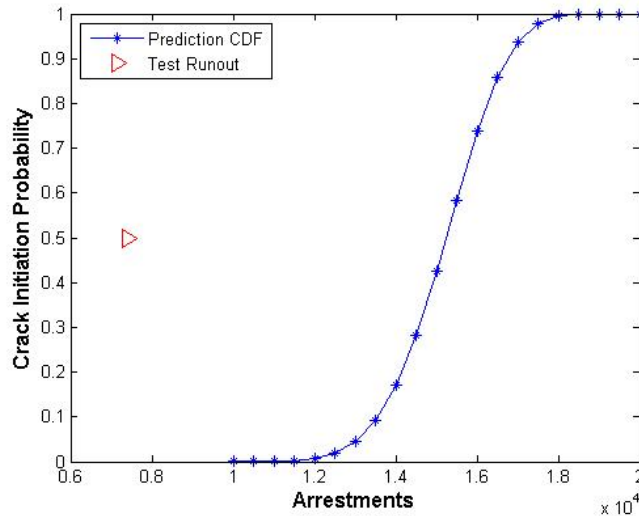


Figure 56: Shank Life Prediction for Damper Lower Half, new 180 deg Replica

CORROSION SURFACE-ROUGHNESS BASED MODELING

Predictions using the grid-based roughness metric method outlined previously were performed on three Batch B specimens with different corrosion exposure times. Plate R_q values for the corrosion patch were extracted prior to fatigue testing using ultrasonic time-of-flight responses. The 99th percentile regression curves were used to convert the UT derived grid R_q values to equivalent WLI values, and to convert the WLI R_q values to equivalent K_{fc} values. Each plate image contained approximately 1,000 grid squares, and 813 to 926 after filtering out grids with R_q values below the noise threshold. The K_{fc} grid values for each plate were combined in a 20-bin histogram, which provided the input to predict the CDF of crack initiation life for the test specimens. Results for the grid-based median life predictions are compared to the ESR predictions and test lives in table 34.

Table 34: Median Life Predictions for Grid-Based Metric Method for Three AF-1410 Batch B Specimens

| Test Specimen | Grid R_q Pred. | ESR Pred. | Test C.I. Life | Grid Test/Pred. Life Ratio | ESR Test/Pred. Life Ratio |
|---------------------------|---------------------|--------------|-------------------|-------------------------------|------------------------------|
| 547-26B (1.5-hr exposure) | 35,006 | 45,041 | 96,069 | 2.744 | 2.133 |
| 547-37B (3-hr exposure) | 31,007 | 54,474 | 82,424 | 2.658 | 1.513 |
| 547-6A (6-hr exposure) | 17,604 | 19,945 | 69,676 | 3.958 | 3.493 |

VERIFICATION AND VALIDATION RESULTS FOR CORROSION-FATIGUE MODELS

Significant progress was made in accomplishing the V&V tasks outlined in the previous sections; however, program cost and schedule constraints limited the number of tasks that could be completed. The final status of each V&V task is listed below:

Code verification tasks:

1. PSL Curve to PSL Code (completed)
2. FFT K_t Transformation to FFT K_t Algorithm (mostly complete)
3. ROI Search Criteria to ROI Search Algorithm (mostly complete)
4. Notch Metric to ESR Life Prediction Algorithm (partially complete)
5. Notch Sensitivity Curve to ESR Life Prediction Algorithm (partially complete)
6. ESR Life Prediction Logic to ESR Life Prediction Algorithm (partially complete)
7. Roughness Metric Formulas to Roughness Metric Algorithm (not started)
8. Roughness Metric Correlation to Roughness Metric Algorithm (not started)
9. Equivalent Geometric Stress Concentration Logic to ESR Shank Life Prediction Algorithm (not started)
10. Equivalent Geometric Stress Concentration Logic to Metric Shank Life Prediction Algorithm (not started)
11. Shank FEM assumptions to Shank FE Model (completed)

Calculation verification tasks:

1. PSL Code to ESR Probabilistic Life Predictions (completed)
2. FFT K_t Algorithm to ESR Probabilistic Life Predictions (completed)
3. ROI Search Algorithm to ESR Probabilistic Life Predictions (mostly complete)
4. ESR Life Prediction Algorithm to ESR Probabilistic Life Predictions (partially complete)
5. Roughness Metric Algorithm to Metric-Based Probabilistic Life Predictions (not started)
6. Metric Life Prediction Algorithm to Metric-Based Probabilistic Life Predictions (not started)
7. ESR Shank Life Prediction Algorithm to ESR Probabilistic Life Predictions (not started)
8. Metric Shank Life Prediction Algorithm to Metric-Based Probabilistic Life Predictions (not started)
9. Shank FE model to ESR and Metric-Based Probabilistic Life Predictions (partially complete)

Validation Tasks:

1. Confidence bounds on ESR Probabilistic Life Predictions
 - a. Identification of sources of uncertainty (mostly complete)
 - b. Input uncertainty distributions (partially complete)
 - c. Sensitivity analysis (not started)
 - d. Confidence bounds on life predictions (preliminary results)
2. Comparison of ESR Probabilistic Life Predictions with AF1410 Batch A and Batch B C-F test results. (partially complete)

3. Confidence bounds on Metric-Based Probabilistic Life Predictions
 - a. Identification of sources of uncertainty (not started)
 - b. Input uncertainty distributions (not started)
 - c. Sensitivity analysis (not started)
 - d. Confidence bounds on life predictions (not started)
4. Comparison of Metric-Based Probabilistic Life Predictions with AF1410 Batch A and Batch B C-F test results. (not started)
5. Confidence bounds on ESR and Metric-Based Probabilistic Life Predictions for Cad-Plated C-F Specimens (not started)
6. Comparison of ESR and Metric-Based Probabilistic Life Predictions with Cad-Plated C-F test results. (partially complete)
7. Confidence bounds on ESR Probabilistic Life Predictions of Large Notch Plates (micromachine specimens).
 - a. Identification of sources of uncertainty (partially complete)
 - b. Input uncertainty distributions (partially complete)
 - c. Sensitivity analysis (not started)
 - d. Confidence bounds on life predictions (not started)
8. Comparison of ESR Probabilistic Life Predictions with Large Notch plate test results. (partially complete)
9. Shank FE model to Shank Strain Survey Results (completed)
10. Confidence bounds on ESR and Metric-Based Probabilistic Shank Life Predictions
 - a. Identification of sources of uncertainty (not started)
 - b. Input uncertainty distributions (not started)
 - c. Sensitivity analysis (not started)
 - d. Confidence bounds on life predictions (not started)
11. Comparison of ESR and Metric-Based Probabilistic Shank Life Predictions with Corroded Shank test results (preliminary results)

The detailed results of many of the V&V tasks can be found in various sections of this report. Other details not included in this report can be found in reference 28.

DISCUSSION

EQUIVALENT STRESS RISER MODEL APPLICATION

Application of the ESR model to predict the fatigue life of corroded components follows the general approach outlined in this paper. The procedures involved in creating the ESR model and applying it to life prediction on an unfailed component can be condensed to nine major steps, which are defined as if the model is being applied to a new material type:

1. Test uncorroded and corroded plates to generate database of material C-F response.
2. Measure characteristic dimensions of critical notches on all test plates.
3. Calculate fatigue notch factor (K_{fc}) for each test plate using the appropriate probabilistic strain-life model with Neuber notch strain relation.
4. Calculate critical notch K_t , equivalent notch root radius and fatigue notch ratio (q_c) for each test plate.
5. Fit notch ratio model to C-F test results.
6. Perform ROI analysis of surface topology data for corroded component, and extract characteristic notch dimensions.
7. Calculate notch K_t and equivalent notch root radius for each ROI.
8. Calculate fatigue notch ratio (q_c) and fatigue notch factor (K_{fc}) for each ROI using notch ratio model.
9. Calculate survival probability for damaged component using all ROIs found.

Steps 1 through 5 define the model creation and calibration process for a new material. Steps 6 through 9 define the process of applying the model to the life prediction of an unfailed corrosion-damaged component.

LIFE PREDICTION UNCERTAINTY FROM THE EQUIVALENT STRESS RISER MODEL

Preliminary life prediction uncertainty results were generated only for a single specimen, but they indicate several important behavioral characteristics of the ESR model. The first is that the solution is highly dependent on the level of correlation assumed between the individual ROI measurement errors. A high degree of correlation gives a solution with a relatively low level of uncertainty, whereas uncorrelated measurement errors give a larger degree of uncertainty relative to the mean prediction, and much greater conservatism in the prediction. The actual amount of error correlation for the nominal ESR prediction can be estimated by comparing the nominal ESR prediction for specimen 62, which uses the expected values for all of the input parameters, to the Monte Carlo estimated means of the median life predictions for the two correlation extremes. The nominal ESR median life prediction for specimen 62 is 48,325 cycles, which is much closer to the fully correlated sample mean value of 54,355 than to the uncorrelated sample mean value of 17,081 cycles. This is a rough indication that the ESR approach has ROI measurement errors that are closely coupled, but not fully correlated. More extensive investigations of uncertainty sources and model behavior will be necessary to fully capture the

influence of input parameter variability on solution accuracy, and to generate accurate confidence intervals for predicted lives. The preliminary analysis presented here serves as a basis for further research in this area.

EQUIVALENT STRESS RISER MODEL CALIBRATION USING EXTREME VALUE STATISTICS

The extreme value approach to calibrating the notched C-F model shows some promise in reducing the amount of conservatism in life prediction as compared to the ESR calibration approach that is currently implemented. However, further development work is necessary to more fully demonstrate an improvement over the existing ESR model.

EQUIVALENT STRESS RISER LIFE PREDICTION ON MICROMACHINED SPECIMENS

Examination of the CDF values for each individual notch prediction in tables 29, 30, and 31 show that both models incorrectly predicted that Ellipsoid 1 would crack first, when in fact the conic frustum features had the earliest cracking in all of the specimens tested. This discrepancy can be explained by the fact that the shape of the conic frustum deviates significantly from the idealized semi-elliptical notch shape used to derive the notch metric equations. As a result, the notch metric equation used to estimate K_t significantly underpredicted the actual value for the conic frustum, as can be seen in table 6. Posttest fractographic examination of these features showed that all of the critical cracks originated from the bottom of the feature, with a few features also having cracks that simultaneously initiated on the sides of the cone. Cracking was also found in most of the Ellipsoid 1 features; however, program time and budget constraints precluded fractographic measurements of the crack sizes, so the crack initiation lives of these features is unknown. Comparison of Ellipsoid 1 crack initiation lives to the predicted life CDF would yield a better validation of the notched fatigue method, since these features are much more representative of the notch geometry that the ESR approach was developed for.

Peterson's notch sensitivity value for quenched and tempered steels gave a more conservative life prediction compared to the Beta distribution fit of the ASM Handbook data. This is to be expected, since the nominal Peterson equation represented a conservative fit to the available notched fatigue data. If the conic frustum feature were correctly modeled by the notch metric equation, and even more conservative prediction would have resulted. The Peterson Beta model gave a mean predicted life that was nonconservative compared to the mean test life. This can be explained by the overprediction of life for the conic frustum features due to the K_t error from the notch metric equation. If the correct K_t value was used for the conic features, a more accurate mean predicted life would likely result. The Monte Carlo Peterson Beta model gave a mean predicted life that was conservative compared to the test life, and slightly outside the lower 95% confidence bound. The conservatism was a result of the increased scatter in the individual notch feature CDFs, which cumulatively reduce the mean life of the overall plate compared to the first Peterson Beta model prediction. The large

amount of scatter evident in the Monte Carlo Peterson Beta CDF is a result of the large prediction bounds on the Beta model calibration of the ASM Handbook data. The prediction bound scatter was propagated through to the life CDF for this version of the model, but not for the original Peterson version and the first Peterson Beta prediction. Much of the scatter in the Monte Carlo Peterson Beta prediction could be reduced by only using a complete set of AF1410 notched fatigue test data for the Beta model calibration. However, this type of data was not available, so data for several other types of materials were used, resulting in the high degree of scatter. What all of the life predictions do show is that by ignoring the errors of fit for both Peterson notch sensitivity model calibrations, the ESR approach to implementing notched fatigue analyses does an excellent job of capturing the variance in fatigue test life for geometrically notched specimens. Both the original Peterson and the first Peterson Beta predictions have standard deviation values that are close to the nominal test value, and fall well within the $\pm 95\%$ confidence bounds.

EQUIVALENT STRESS RISER LIFE PREDICTION ON CADMIUM-PLATED CORROSION-FATIGUE SPECIMENS

The blind life predictions performed on the cad-plated C-F plates represent a true validation of the ESR modeling approach, and demonstrate that the ESR approach is not dependent on how the corrosion damage was incurred on the surface. Cad-plated specimens were subjected to an SO₂ salt-fog chamber for corrosion growth, as opposed to the electro-potential accelerated growth method used on the unplated Batch A and Batch B plates. The cad-plated corrosion has an overall topology that is different from the unplated specimens, and more closely resembles the service-induced corrosion on the F/A-18 arresting shanks. The life predictions show a level of conservatism similar to the predictions on the Batch A and Batch B plates.

EQUIVALENT STRESS RISER LIFE PREDICTION ON AN F/A-18C/D ARRESTING SHANK SECTION

The $K_{g-equiv}$ approach to incorporating stress gradient effects in an ESR life prediction has been shown to provide reasonable life prediction results for an F/A-18C/D arresting shank corroded section. Difficulties with dirt and dust in the WLI scan point to the importance of maintaining a clean specimen surface during scanning. This is especially important when scanning replicas of corroded surfaces, as it is much more difficult to filter out unwanted contamination from the resulting WLI scans. After the shank was tested, the damper region was sectioned in half longitudinally to expose the corroded surface. New replicas were made of each section, and complete WLI scans were performed by UDRI. The lower 180 deg section of the damper region was then used to make a new life prediction, with the result that the predicted crack initiation life for the corroded region nearly doubled compared to the initial prediction. The WLI scans from the new replicas showed no visible evidence of contamination, indicating that taking steps to minimize contamination during the scanning process can substantially improve the predictive capability of the ESR model. K_t maps were generated for the upper 180 deg section of the damper region using the new replica scans, but

the ROI analysis and a shank life prediction incorporating corrosion from the upper damper region were not completed due to program schedule constraints.

CORROSION SURFACE-ROUGHNESS BASED MODELING

The limited number of roughness metric life predictions performed show the method to be more conservative than the corresponding ESR predictions for the same test specimens. Much of this additional conservatism is due to the use of 90th percentile correlation curves. If mean regression correlation curves are used, the roughness metric life predictions are much closer to the ESR predictions. However, the considerable amount of scatter in the correlations makes it necessary to use upper percentile curves if a high degree of confidence in the prediction is to be achieved. Analysis of the grid-based metric modeling approach indicates that the UT derived roughness values capture the large-scale corrosion features such as crevice corrosion, but does not have the resolution to capture the small notch features that cause fatigue cracking. In applying the roughness-based life prediction methods, an implicit assumption is that the small notches are spatially correlated with areas of large-scale corrosion features. This correlation was reduced for some of the lower corrosion exposure level specimens, resulting in the critical grid roughness values being of a lower percentile than for the higher exposure level specimens. The large-scale/small-scale feature correlation becomes important when applying the method to components with surface coatings, because the coatings protect the material from general corrosive attack. Fleet corroded components with protective coatings may not accumulate the type of large-scale corrosion damage necessary to trigger a UT-derived roughness metric fatigue life reduction, even though a significant amount of small-scale corrosion damage is present. For this reason, the behavior of roughness metric life prediction methods on coated materials should be ascertained before using the method to make disposition decisions on fleet corroded components.

VERIFICATION AND VALIDATION FOR CORROSION-FATIGUE MODELS

A robust V&V process was defined for this program, but budget and schedule constraints limited the amount of V&V work that could be completed. Still, the work that was completed indicates that the ESR model can meet the preliminary engineering validation criteria of a factor of 1 to 4 conservatism in model median life prediction error at the 95% confidence level, for light-to-moderate levels of surface corrosion damage. Whether the specified validation criteria represent acceptable limits for applying the method to fleet corroded components remains to be seen. Demonstration of the ESR method on several cases of fleet corroded components will likely be necessary to determine if the life predictions provide sufficient fatigue margin for the method to be useful. It may be necessary to tailor the validation criteria for specific component applications, and differing applications should be approached on a case-by-case basis.

CONCLUSIONS

Initial investigation of the ESR model demonstrates that an empirical approach to corrosion surface damage that builds on traditional notched fatigue analysis methods can be utilized to generate probabilistic life predictions that have substantial engineering value in assessing the residual fatigue life of corroded AF1410 steel components. Further work to refine the ROI search algorithm methods, and to investigate the sensitivity to varying levels of corrosion and WLI scan resolution is warranted. However, the approach captures the significant corrosion features that cause fatigue cracking in most cases, especially for more severely corroded surfaces. Predictions generated for micromachined notched plates have shown that traditional notched fatigue analysis techniques, implemented in a probabilistic framework, adequately captured the variance in fatigue test lives even when the median prediction is conservative. The blind life predictions performed on the cadmium-plated C-F plates represent a true validation of the ESR modeling approach, and demonstrate that the ESR approach is not dependent on how the corrosion damage was incurred on the surface. The incorporation of stress gradient effects in an ESR life prediction has been shown to provide reasonable preliminary results for an F/A-18C/D arresting shank corroded section. WLI scans of the complete corroded surface of a shank are available for future analysis. A method of life prediction using grid-based surface roughness statistics was developed to enable the use of low-resolution UT inspection techniques on corroded components. While the life predictions using this method were more conservative than the corresponding ESR predictions, it is not certain how the method will perform on components with corroded surfaces that contain little to no large-scale corrosion features, but many small-scale corrosion features of the type that cause fatigue cracks. A robust V&V process was defined for this program, but was not completed due to program budget and schedule constraints. The V&V work that was completed indicates that the ESR model can meet the preliminary engineering validation criteria of a factor of 1 to 4 conservatism in model median life prediction error at the 95% confidence level, for light-to-moderate levels of surface corrosion damage.

THIS PAGE INTENTIONALLY LEFT BLANK

REFERENCES

1. Fontana, M.G., "Corrosion Engineering," Third Ed., McGraw-Hill, New York, 1986, p. 63.
2. Mills, T., Sharp, P.K., and Loader, C., "The Incorporation of Pitting Corrosion Damage into F-111 Fatigue Life Modeling," DSTO-RR-0237, DSTO Aeronautical and Maritime Research Laboratory, 506 Lorimer St., Fishermans Bend, Vic. 3207, Australia, of Jun 2002.
3. Komai, K., "Life Estimation of Stress Corrosion Cracking and Corrosion Fatigue in Structural Materials," Kanazawa Kogyo Diagaku Zairyo Sisutemu (Materials Systems), Vol. 19, No. 19, Japan, 2000, pp. 7-14.
4. Harlow, D.G. and Wei, R.P., "Probability Approach for Prediction of Corrosion and Corrosion Fatigue Life," *AIAA Journal*, Vol. 32, No. 10, Oct 1994, pp. 2073-2079.
5. Wang, Q.Y., Pidaparti, R.M., and Palakal, M.J., "Comparative Study of Corrosion-Fatigue in Aircraft Materials," *AIAA Journal*, Vol. 39, No. 2, Feb 2001, pp. 325-330.
6. Shi, P. and Mahadevan, S., "Damage Tolerance Approach for Probabilistic Pitting Corrosion Fatigue Life Prediction," *Engineering Fracture Mechanics*, Vol. 68, 2001, pp. 1493-1507.
7. Hoppe, W., Scott, O., Braisted, B., Abfalter, G., Pierce, J., Burke, E., Kuhlman, S., Frock, B., and Ko, R., "Navy High-Strength Steel Corrosion-Fatigue Modeling Program," UDR-TR-2007-00039, University of Dayton Research Institute, Dayton, OH, of Oct 2006.
8. NAVAIRWARCENACDIV Patuxent River Engineering Data Report No. NAWCADPAX/EDR-2008/10, Results of Fatigue Tests of Bare AF1410 Steel Unnotched Flat Plates with Surface Corrosion Damage, of 8 May 2008.
9. Dowling, N.E., "Mechanical Behavior of Materials," Second Ed., Prentice Hall, 1999.
10. Bannantine, J.A., Comer, J.J., and Handrock, J.L., "Fundamentals of Metal Fatigue Analysis," Prentice Hall, 1990.
11. Peterson, R.E., "Analytical Approach to Stress Concentration Effects in Aircraft Materials," TR 59-507, *U.S. Air Force – WADC Symposium on the Fatigue of Metals*, Dayton, OH, 1959.
12. Neuber, H., "Theory of Notch Stresses: Principle for Exact Stress Calculations," J.W. Edwards, Ann Arbor, MI, 1946.
13. Young, W.C., "Roark's Formulas for Stress and Strain," Sixth Ed., McGraw Hill, 1989.

14. Pilkey, W.D., "Peterson's Stress Concentration Factors," Second Ed., John Wiley and Sons, Inc., 1997.
15. ASTM E606, "Standard Practice for Strain-Controlled Fatigue Testing," ASTM International, West Conshohocken, PA, 2004.
16. ASTM E466, "Standard Practice for Conducting Force Controlled Constant Amplitude Axial Fatigue Tests of Metallic Materials," ASTM International, West Conshohocken, PA, 1996.
17. Pascual, F.G. and Meeker, W.Q., "Estimating Fatigue Curves with the Random Fatigue-Limit Model," *Technometrics*, Vol. 41, No. 4, of Nov 1999, pp. 277-290.
18. Socie, D.F. and Marquis, G.B., "Multiaxial Fatigue," SAE International, 2000, p. 351.
19. Myers, R.H., "Classical and Modern Regression with Applications," Second Ed., PWS-Kent, 1990.
20. Rasband, W., ImageJ, U.S. National Institutes of Health, Bethesda, MD, USA, <http://rsb.info.nih.gov/ij/>, 1997-2008.
21. Weibull, W., "A Statistical Representation of Fatigue Failure in Solids", Transactions of the Royal Institute of Technology, Stockholm, Sweden, 1949.
22. Hoppe, W. "Improved Navy Maintenance through Corrosion-Fatigue Assessment Program," UDR-TR-2008-00064, University of Dayton Research Institute, Dayton, OH, of Mar 2008.
23. Peterson, R.E., "Analytical Approach to Stress Concentration Effect in Fatigue of Aircraft Materials," U.S. Air Force-WADC Symposium on Fatigue of Metals, TR 59-507, Dayton, OH, 1959.
24. "Aerospace Structural Metals Handbook", Metals and Ceramics Information Center, Battelle Columbus Division, Columbus, OH, 1987.
25. Shooman, M.L., "Probabilistic Reliability: An Engineering Approach," McGraw Hill, New York, 1968.
26. ASME V&V 10-2006, "Guide for Verification and Validation in Computational Solid Mechanics," American Society of Mechanical Engineers, New York, of 29 Dec 2006.
27. NAVAIRWARCENACDIV Patuxent River Technical Report No. NAWCADPAX/TR-2008/9, Analysis and Testing of Fleet Corroded F/A-18C/D Arrestment Shanks, of 20 Jun 2008.

28. Hoppe, W., Braisted, W., Pierce, J., and Abfalter, G., "Corrosion-Fatigue Assessment Program – Final Report," UDR-TR-2008-00069, University of Dayton Research Institute, Dayton, OH, of Mar 2008.

THIS PAGE INTENTIONALLY LEFT BLANK

APPENDIX A
 VERIFICATION AND VALIDATION FRAMEWORK FLOWCHARTS

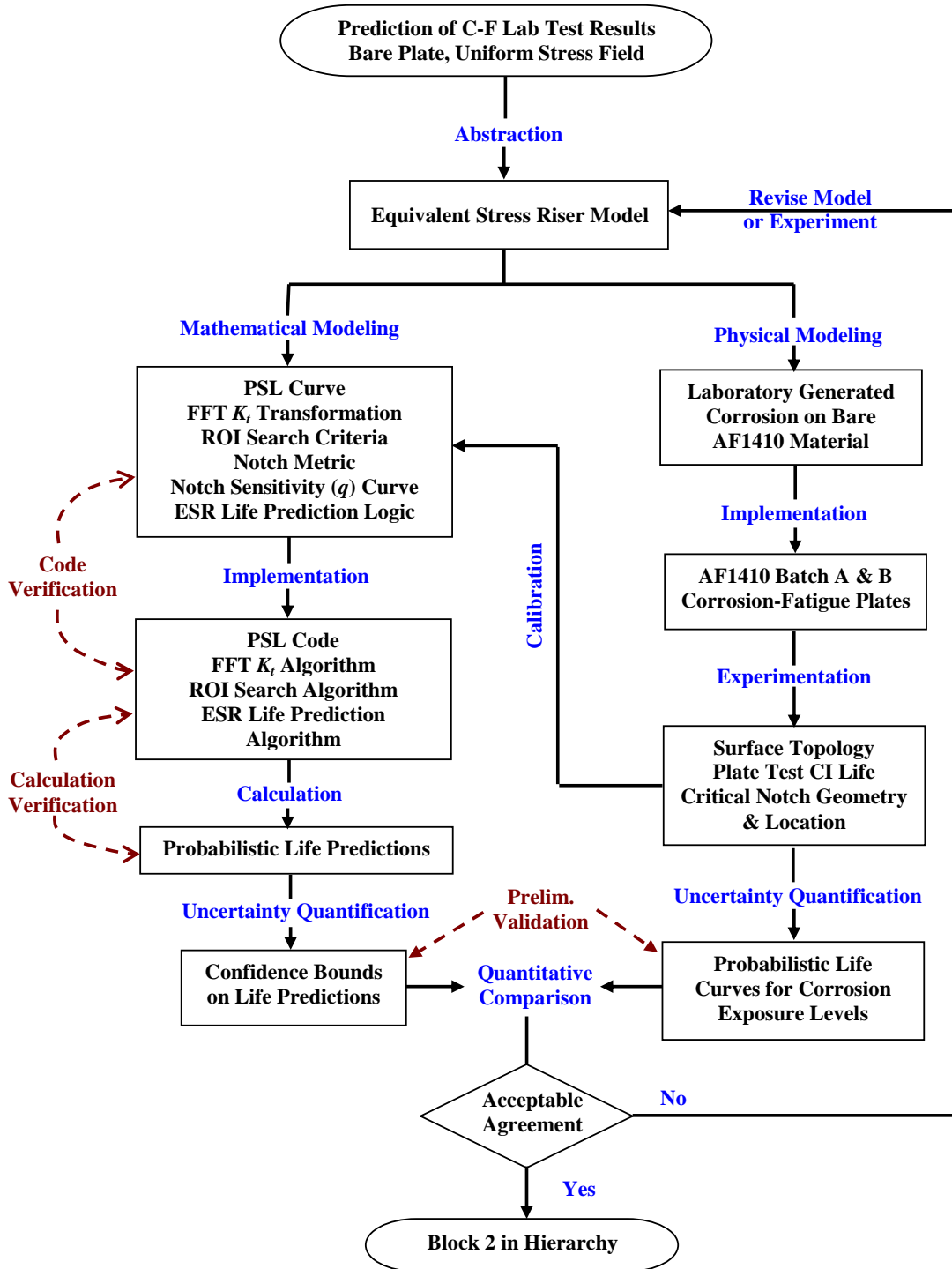


Figure A-1: V&V Framework for Block 1A of C-F Life Characterization Hierarchy

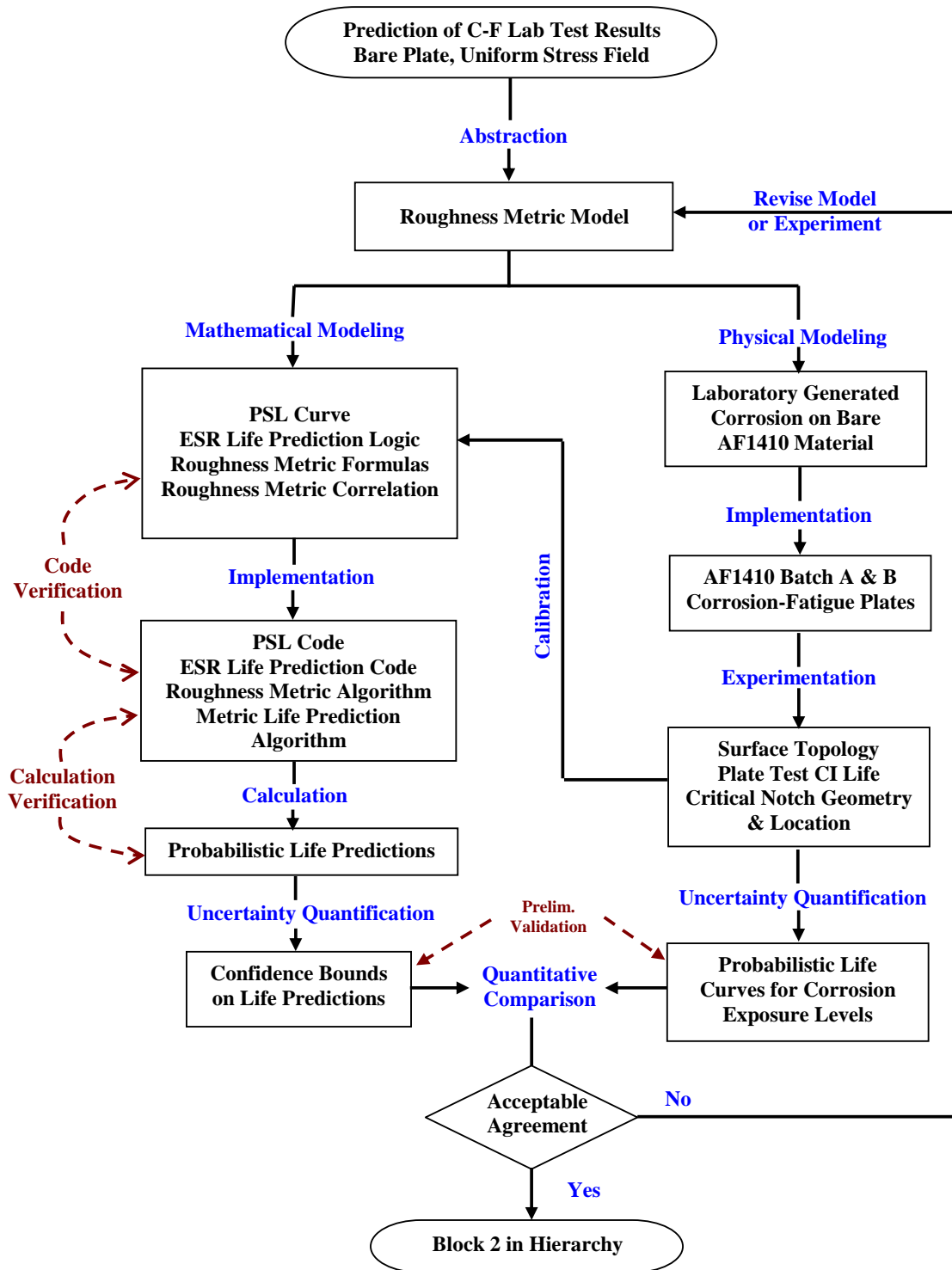


Figure A-2: V&V Framework for Block 1B of C-F Life Characterization Hierarchy

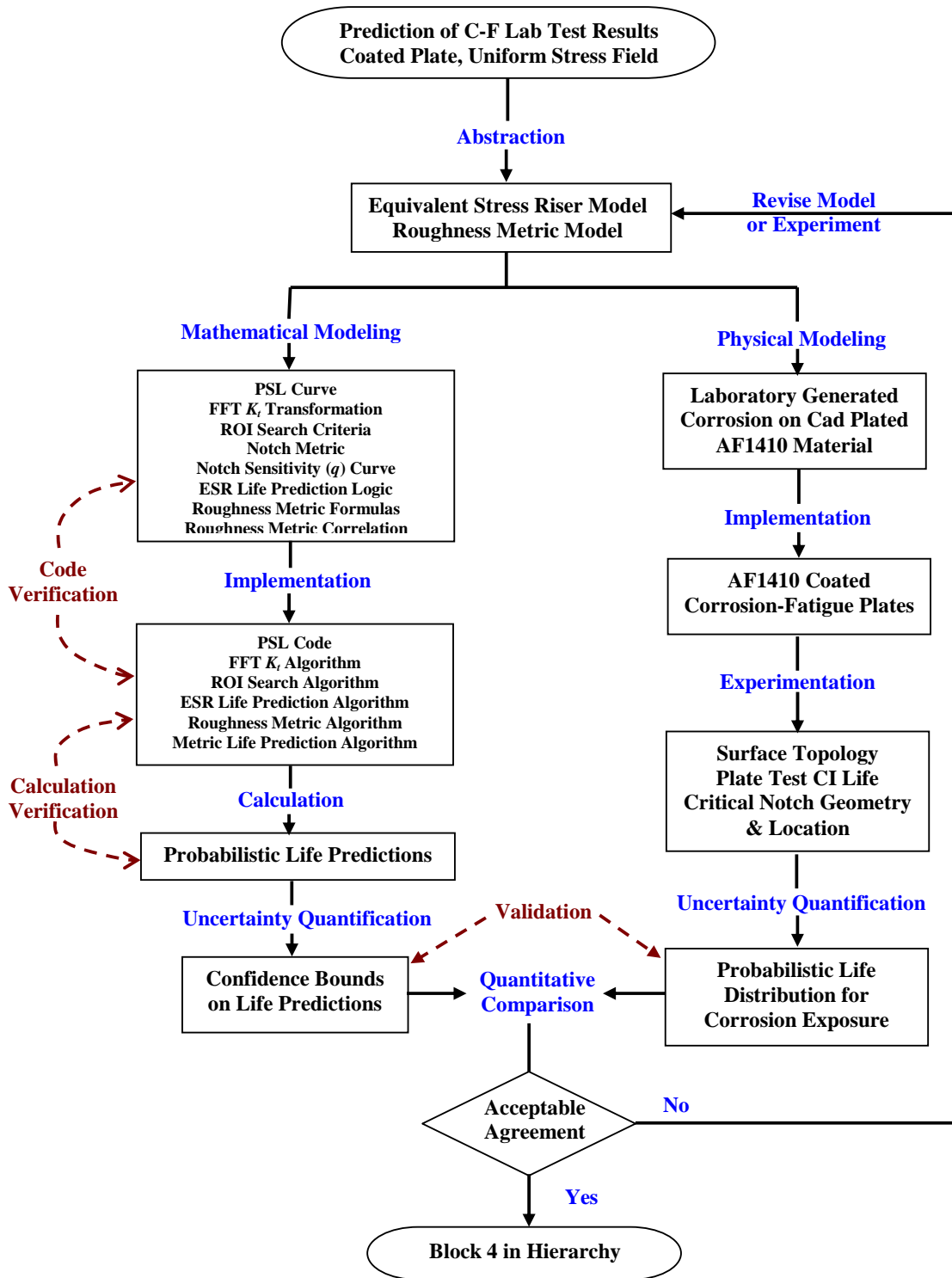


Figure A-3: V&V Framework for Block 2 of C-F Life Characterization Hierarchy

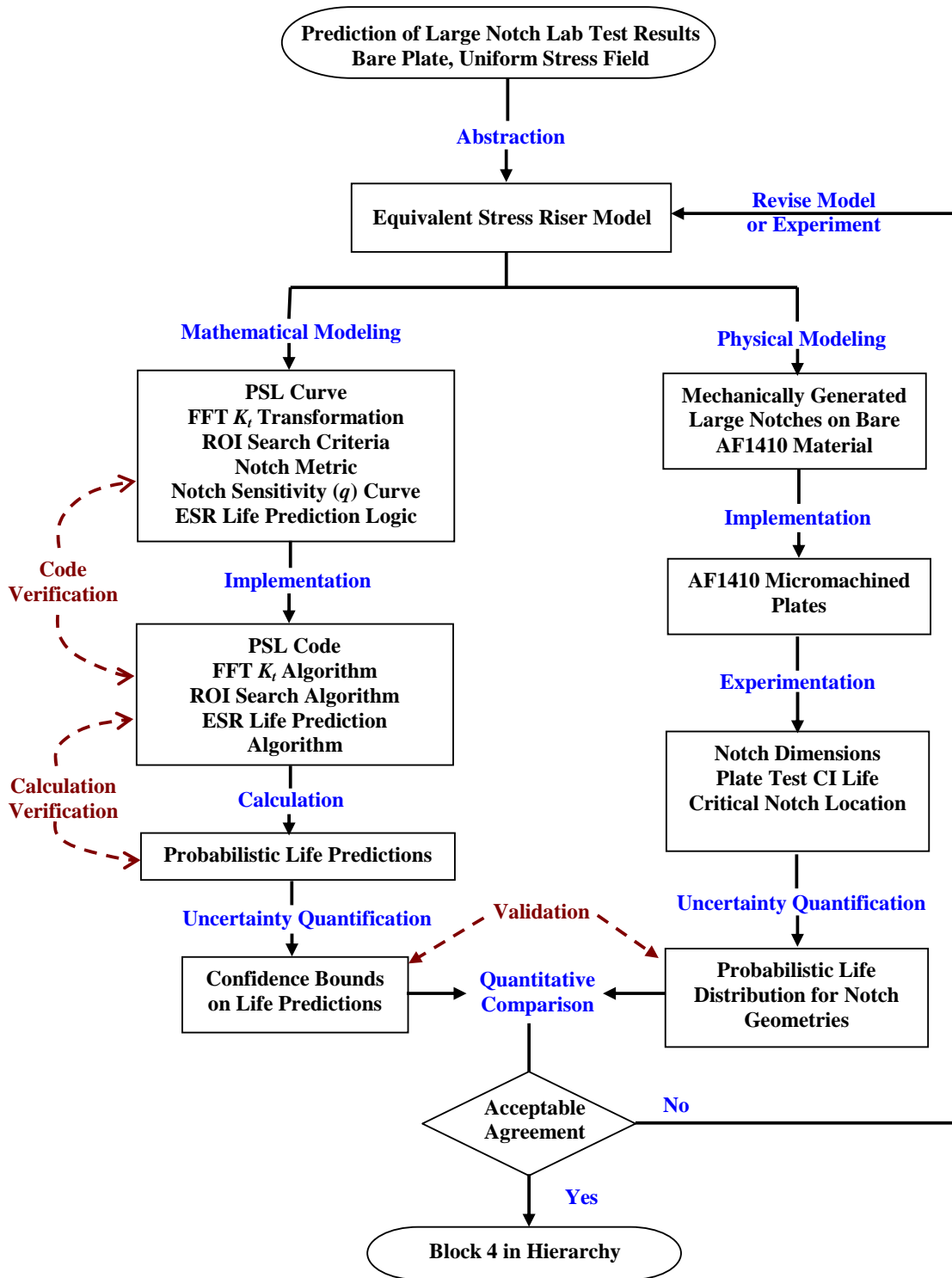


Figure A-4: V&V Framework for Block 3 of C-F Life Characterization Hierarchy

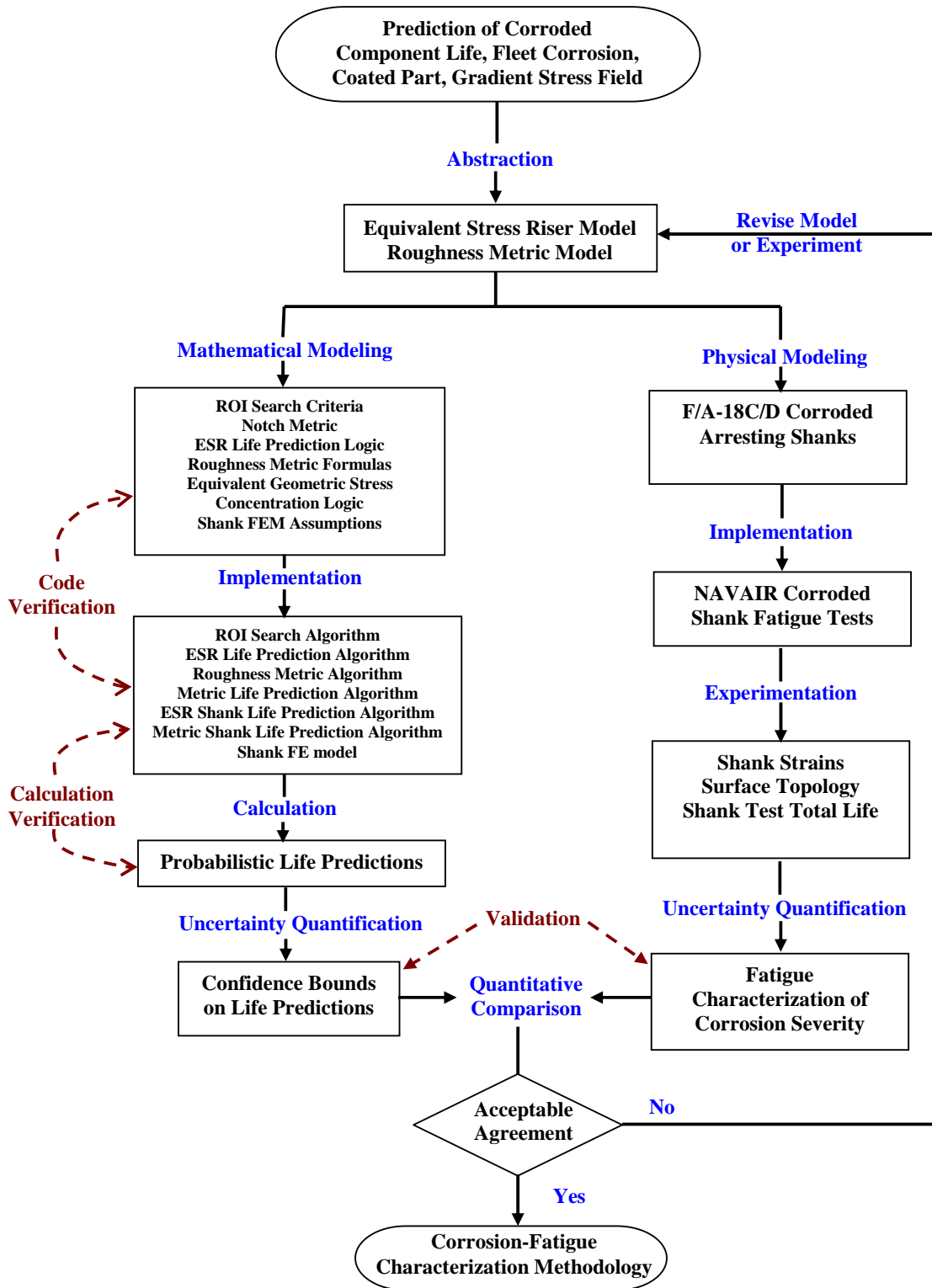


Figure A-5: V&V Framework for Block 4 of C-F Life Characterization Hierarchy

THIS PAGE INTENTIONALLY LEFT BLANK

DISTRIBUTION:

NAVAIRSYSCOM (AIR-4.3E/Polakovics), Bldg. 2187, Room 3390C (1)
48110 Shaw Road. Unit 5, Patuxent River, MD 20670-1906

NAVAIRSYSCOM (AIR-4.3/Frazier), Bldg. 2187, Room 3390C (1)
48110 Shaw Road. Unit 5, Patuxent River, MD 20670-1906

NAVAIRSYSCOM (AIR-4.3./Agarwala), Bldg. 2187, Room 3390C (1)
48110 Shaw Road. Unit 5, Patuxent River, MD 20670-1906

NAVAIRSYSCOM (AIR-4.3.3/Nam Phan), Bldg. 2187, Room 2340A (1)
48110 Shaw Road. Unit 5, Patuxent River, MD 20670-1906

NAVAIRWARCENACDIV (4.3.3.1/Richard Ryan), Bldg. 2187, Room 2340A (1)
48110 Shaw Road. Unit 5, Patuxent River, MD 20670-1906

NAVAIRWARCENACDIV (4.3.3.2/Clyde Simmerman), Bldg. 2187, Room 2340A (1)
48110 Shaw Road. Unit 5, Patuxent River, MD 20670-1906

NAVAIRWARCENACDIV (4.3.3.5/David Barrett), Bldg. 2187, Room 2340A (3)
48110 Shaw Road. Unit 5, Patuxent River, MD 20670-1906

NAVAIRWARCENACDIV (4.3.4.1/Darrel Tenney), Bldg. 2188 (1)
48066 Shaw Road. Unit 5, Patuxent River, MD 20670-1906

NAVAIRWARCENACDIV (4.3.4.6/Fred Lancaster), Bldg. 2188 (1)
48066 Shaw Road. Unit 5, Patuxent River, MD 20670-1906

NAVAIRSYSCOM (AIR-5.1), Bldg. 304, Room 100 (1)
22541 Millstone Road, Patuxent River, MD 20670-1606

NAVAIRWARCENACDIV (4.12.6.2), Bldg. 407, Room 116 (1)
22269 Cedar Point Road, Patuxent River, MD 20670-1120

Airframe Technology, U.S. Army Aviation and Missile Command (Attn: Jon Shuck) (1)
Fort Eustis, VA, 23604-5577

Director, Aerospace Science Research Division (Attn: Dr. Kathy Stevens) (1)
Office of Naval Research, 875 Randolph Street, Arlington, VA 22203-1995

Office of Naval Research, Scientific Officer (John Kinzer) (1)
875 Randolph Street, Arlington, VA 22203-1995

Office of Naval Research, Scientific Officer (Dr. Davis Shifler) (1)
875 Randolph Street, Arlington, VA 22203-1995

Office of Naval Research, Scientific Officer (Dr. Cliff Bedford) (1)
875 Randolph Street, Arlington, VA 22203-1995

Director, Naval Material Sea Platform Division (Dr. Julie Ann Christodoulou) (1)
Office of Naval Research, 875 Randolph Street, Arlington, VA 22203-1995

Naval Research Laboratory (Dr. John Michopolus), Bldg. 28, Room 117 (1)
Washington, DC 20020

AFMC (Charles Babish), 2530 Loop Road West, B560 ASC/EN (1)
Wright-Patterson AFB, OH 45433

AFMC (Joe Gallagher), 3340 Ferry Road (1)
Bellbrook, OH 45305

DTIC (1)
Suite 0944, 8725 John J. Kingman Road, Ft. Belvoir, VA 22060-6218

UNCLASSIFIED

UNCLASSIFIED